DISSERTATION

CROSS-VALIDATION OF SPACEBORNE RADAR AND GROUND POLARIMETRIC RADAR OBSERVATIONS

Submitted by

Steven M. Bolen

Department of Electrical and Computer Engineering

In partial fulfillment of the requirements

For the Degree of Doctor of Philosophy

Colorado State University

Fort Collins, Colorado

FALL 2002

UMI Number: 3075342

UMI®

UMI Microform 3075342

ProQuest Information and Learning Company
300 North Zeeb Road
P.O. Box 1346
Ann Arbor, MI 48106-1346

COLRADO STATE UNIVERSITY

May 31, 2002

WE HEREBY RECOMMEND THAT THE DISSERTATION PREPARED UNDER OUR SUPERVISION BY STEVEN M. BOLEN ENTITLED "CROSS-VALIDATION OF SPACEBORNE RADAR AND GROUND POLARIMETRIC RADAR OBSERVATIONS," BE ACCEPTED AS FULFILLING, IN PART, REQUIREMENTS FOR THE DEGREE OF DOCTOR OF PHILOSOPHY.

Committee on Graduate Work

V.N. Bringi

Advisor

Department Head

ABSTRACT OF DISSERTATION

CROSS-VALIDATION OF SPACEBORNE RADAR AND GROUND POLARIMETRIC RADAR OBSERVATIONS

There is great potential for spaceborne weather radar to make significant observations of the precipitating medium on global scales. Unlike other instruments, such as light detecting and ranging (lidar) systems that operate in the optical region, and thermatic mapping systems that use short wavelengths in the infrared, etc., radar has the ability to penetrate the cloud and rain layer to make observations of the vertical profile of the rain field. Though the scientific reasons for making weather observations using spaceborne radar are varied, the benefits of using space-based weather radar have been largely unrealized. The technological advances in spaceborne weather radar systems that were required to reduce the size, weight and cost of deployment, and to meet the efficiency, reliability and sensitivity needs of the scientific community were not available until the 1990's.

In 1997, the Tropical Rainfall Measuring Mission (TRMM) satellite was launched. TRMM was the first dedicated mission to study rainfall in the tropics from space. The satellite operates in a nearly circular orbit at 350 km nominal altitude and 35 degree inclination. It carries several meteorological observing instruments, including the

13.8 GHz Precipitation Radar (PR). This instrument is designed to yield information about the vertical storm structure so as to gain insight into the intensity and distribution of rainfall. Attenuation effects on PR measurements, however, can be significant, which can be as high as 10-15 dB. This can seriously impair the accuracy of rain rate retrieval algorithms derived from PR signal returns, which makes it necessary to compensate for attenuation effects. Independent evaluation and verification of attenuation correction, and subsequent rain rate estimation, derived from spaceborne algorithms is an important task in order to accurately determine the rain rate from space.

Direct inter-comparison of meteorological measurements between space radars with polarimetric ground radar observations can be used to evaluate and validate spaceborne processing algorithms. Though conceptually straightforward, this can be a challenging task. Differences in viewing aspects between space and earth point observations, propagation frequencies, resolution volume size and time synchronization mismatch between measurements can contribute to direct point-by-point inter-comparison errors. The problem is further complicated by spatial geometric distortions induced into the space-based observations caused by the movements and attitude perturbations of the spacecraft itself. A method is developed to align space and ground radar observations so that a point-by-point inter-comparison of measurements can be made. The method uses variable resolution volume matching to match observations between the two systems and a polynomial alignment technique to minimize the effects of potential geometric distortion in space radar observations relative to ground measurements. Examples of the alignment method are presented using TRMM PR reflectivity measurements and ground radar measurements from the National Center for Atmospheric Research (NCAR) S-band polarimetric (SPOL) radar.

After appropriate resolution volume matching and alignment, *in situ* data collected from the TRMM TExas and FLorida UNderflights (TEFLUN-B) experiment, and the Large-scale Biosphere Atmosphere (LBA) field campaign was used to calibrate PR measurements, and to evaluate the PR attenuation correction algorithm relative to ground-based measurements. Ground-based polarimetric observations are used to quantitatively estimate the attenuation on PR signal returns along individual PR beams, and a technique is formulated to determine the *true* PR return via theoretical modeling of specific attenuation (k) at PR wavelength with ground-based S-band radar observations. The reflectivity factor (Z_h) at horizontal polarization state and specific differential phase (K_{dp}) are determined along the PR beam from GR measurements, and a theoretical relationship is used to determine the expected specific attenuation (k) along the space-earth path at K_u-band frequency from these measurements. A theoretical k-K_{dp} relationship is determined for moderate rain rate (when $K_{dp} \geq 0.5$ deg/km); and, a power-law relationship, $k = a\, Z_h^b$, is used for light rain and for other types of hydrometers encountered along the path. The two-way path-integrated attenuation (PIA) is calculated along the PR propagation path by integrating the specific attenuation along the path. The *true* PR reflectivity is then determined from PIA estimates and the measured PR reflectivity.

Ground-based polarimetric observations are also used to quantitatively estimate the parameters of a three-parameter gamma raindrop size distribution (RSD) model along individual PR beams in the presence of rain. The mean shape of the raindrops is used along with polarimetric measurements to retrieve the model parameters N_w, D_0 and μ. The current algorithm used by the PR for attenuation correction is evaluated using GR polarimetric estimates of the functional behavior of the RSD along PR beams. The statistical behavior of the gamma model parameters, and PR attenuation correction algorithm, are presented in histogram form along the vertical profile through the rain layer, which is used to evaluate the PR attenuation correction algorithm. Additionally, PR rain rate estimates near the earth surface are compared to polarimetric ground-based radar observations. This analysis leads to direct evaluation of the PR-derived RSD model parameter values. The analysis, and summary, of this work is presented in the dissertation.

Steven M. Bolen

Department of Electrical and Computer Engineering

Colorado State University

Fort Collins, Colorado State University 80523

FALL 2002

ACKNOWLEDGEMENTS

It is with great humility that I thank the Good Lord for giving me the strength and patience to complete this task that I have undertaken, and for providing me the graces of the kind people who have helped me along the way. To my committee, Dr.'s Derek Lile, Paul Mielke and V. N. Bringi, it has been my great pleasure to study under your tutelage, guided by your wisdom. Dr. Bringi, as my brother before me, I have found you to be a most brilliant and patient person without whose help I could not have succeeded. To Dr.'s Robert Meneghini of NASA Goddard Space Flight Center, Toshio Iguchi of the Communications Research Laboratory (CRL) in Japan and Eugineo Gorgucci of the Istituto di Fisica dell' Atmosfera (CNR) in Rome, Italy, it has been my distinct honor to have benefited from your knowledge and experiences, and whose many discussions have aided my work greatly. Dr. Gorgucci, your keen insights and amicable personality have made it a pleasure to work with you. To my management at the National Aeronautics and Space Administration (NASA) at the Lyndon B. Johnson Space Center in Houston, Texas, my eternal gratitude for your generous support and for allowing me to study at such a fine institution as Colorado State University. In particular, my deepest appreciation to my supervisor, Dr. Andrew Benjamin, for his constant and never ending faith in me. To my family, my parents, Don and Maria, and my best friend, my brother, Scott, it has been your strength, love and encouragement that have sustained me throughout all of this. And, lastly (but, not in the least), to my advisor, Dr. Chandrasekar (whom, with the greatest of respect and admiration, we all call Chandra), who has not only been my guide through all of this, but also a friend, colleague, supervisor and mentor. As an educator in the classroom I have found him to be without equal, as a researcher in search of the truth I have found him to be brilliant. It will now be my lifelong task to bring honor to his work and to have him be proud of my own.

This work was supported by the NASA/JSC Human Resources Development Office under the JSC Fellowship Program, and the NASA/GSFC TRMM Program.

DEDICATION

To my parents, Donald and Maria Bolen, who grew up as simple Iowa farmers, both becoming educators, who have dedicated their lives to the pursuit of truth and enlightenment, and who have instilled in my brother and me the ideals of freedom, hard work, honor and patience: God Bless them with the Love and Strength with which they have shown me.

"All men by nature desire knowledge." Aristotle, Metaphysics I

TABLE OF CONTENTS

LIST OF FIGURES

LIST OF TABLES

Chapter 1

1 INTRODUCTION

1.1 Historical Perspective and General Description of the Problem

Observing the precipitating medium on a global scale is of significant importance to monitoring the impact of human activity on the environment as well as to understanding the hydrological processes that regulate the climate. The use of radar to remotely observe the precipitating medium has been studied for nearly 60 years when Ryde (1941, 1946), principally concerned with precipitation as unwanted clutter, first showed the relationships between reflectivity, attenuation and rain rate at microwave frequencies. Other researchers such as: Wexler and Swingle (1947), Marshall, et. al., (1947), Atlas (1947, 1948) and Marshall and Palmer (1948), extended the work of Ryde to meteorological applications. Work continued through the 1950s and 1960s on development of a single relationship between radar return echo and rain rate (Marshall, et. al., 1947; Austin and Williams, 1951; Cataneo and Stout, 1968; Cataneo, 1969), but was largely unsuccessful (Blanchard, 1953; and, Batan, 1973). By the 1970s dual-polarization techniques were being used to study propagation effects (e.g., differential attenuation and differential phase shift), as well as particle size and orientation (McCormick and Hendry, 1975). Later, Seliga and Bring (1976, 1978) used these analyses along with information about the equilibrium raindrop shape (Pruppacher and Beard, 1970) to formulate relationships between the rain rate and polarimetric observations of the precipitation. Though difficulties exist in determining the exact relationship between the return signal echo and the rain rate field, the unique ability of weather radar to describe the three-dimensional spatial variability of the storm structure, over large areas quickly and efficiently, will continue to be of interest to the meteorological community. In particular, spaceborne weather radar will be a critical component for providing global coverage, and measurement of the vertical profile, of the precipitating medium.

The potential use of space-based radar for meteorological interests was first explored as early as the mid-1950s (e.g., Wexler, 1954, 1957; and, Widger and Touart, 1957). However, due to the technical limitations of spacecraft components, and the difficulty in meeting the required science objectives (Dennis, 1963a and 1963b), it remained largely neglected in the United States until the mid-1970s when meteorological applications were re-evaluated as technology advanced (e.g., Skolnik, 1974; Eckerman and Wolf, 1975; and, Okamoto, et. al., 1979). During this time, one of the catalysts for the renewed interest stemmed from the science planning for the Space Shuttle Orbiter (SSO) program (Eckerman, 1975). Over the next two decades following this period, various system architectures were studied and proposed including (but not limited to): nadir looking systems (Goldhirsh and Walsh, 1982), conical scanning systems (Moore and Xie, 1988) and cross-track scanning systems (Tropical System Energy Budget [BEST], 1988). Several profiling methods were also proposed during this time, such as: single frequency systems (Marzoug, et. al., 1989), dual frequency systems (Goldhirsh, 1988; Im and Li, 1989; and, Im and Kellog, 1990) and dual beam systems (Testude, et. al., 1992). While the use of space-based platforms for making meteorological observations on global, synoptic and climatological scale is of scientific value, the cost of these systems, however, can be substantial.

Short wavelength radars can be used to reduce costs by deploying smaller antennas while maintaining the required resolution necessary for adequate meteorological sampling (Meneghini and Kozu, 1990). Attenuation of high-frequency signals, though, can be quite severe (as high as 10–15 dB) at K_u-band frequency [Bolen and Chandrasekar, 2000], which can significantly impair the accuracy of rainfall rate estimation algorithms. For systems operating with a single attenuating frequency, Hitschfeld and Bordan (1954) were among the first to propose a method of attenuation estimation by forward integration of the backscattered radar signal. This method, however, can become unstable when the path length is long unless the raindrop size distribution (RSD) along the path and radar constant are known to a high degree, which is seldom the case. Previously, airborne experiments were conducted at frequencies envisioned for space radars to test the validity of space-based processing algorithms. The surface reference technique (SRT) is one method that was proposed to compensate for instabilities in the forward integration method. This method was developed and tested using airborne weather radar to determine its suitability to space-based applications (see, Durden and Haddad, 1998; Fujita 1983; Iguchi and Meneghini, 1994; Kozu and Nakamura, 1991; Marecal et. al., 1997; Marzoug and Amayenc, 1994; Meneghini et. al., 1983; and, Meneghini et. al., 1992). Data collected from airborne experiments was also used in several other studies such as: Fujita et. al. (1985), Meneghini et. al. (1989), Meneghini and Nakamura (1990), Marzoug and Amayenc (1991, 1992 and 1993), and Amayenc and Marzoug (1992) to evaluate various attenuation estimation and rain rate retrieval schemes. More recently, satellite-based beacon data has been used along with ground radar observations to characterize the attenuation on high-frequency earth-space radio links. Beaver and Bringi (1997) used beacon data from the Advanced Communications Technology Satellite (ACTS) and radar data from the Colorado State University (CSU) CHILL radar facility to characterize the relationships between K_a-band attenuation and ground radar observations. This work built upon previous studies that used ground radar and satellite beacon data to determine the attenuation characteristics of precipitation on high-frequency radio wave propagation, such as the COMSTAR (Cox, 1978) and OLYMPUS–OPEX (Olympus Propagation EXperimenters) (see Davies, 1994) campaigns.

Direct comparison of space and ground-based radar observations, on a point-by-point basis, can be made to physically validate spaceborne algorithms. The Precipitation Radar (PR) aboard the Tropical Rainfall Measuring Mission (TRMM) satellite operates at 13.8 GHZ frequency and is currently using a single frequency scheme based on the Hitschfeld-Bordan and SRT methods (Iguchi et. al., 2000) to estimate the attenuation effects on the return signal. Simultaneous measurements of multi-parameter ground radar data and TRMM PR data have been collected during the TRMM TExas and FLorida UNderflights (TEFLUN-B) and Large-scale Biosphere Atmosphere (LBA) field campaigns in order to precisely determine the affects of precipitation on K_u-band frequency, and to evaluate satellite-based estimation and parameter retrieval algorithms. The process of cross validating spaceborne radar observations with ground observations is not an easy task, however. Differences in viewing aspects, operating frequencies, resolution volume size, orientation, and time synchronization mismatch can contribute to inter-comparison errors (Bolen and Chandrasekar, 2002). The problem is further complicated by geometric distortion induced upon space-based observations caused by the movements and attitude perturbations of the satellite itself (Schowengerdt, 1997). Though previous techniques and methods have been used to evaluate space-based estimation algorithms, it is nonetheless, important to perform independent validation using direct measurements from spaceborne systems, such as the TRMM PR, in order to quantify the systematic behavior of space weather radar correction methods and parameter retrieval algorithms under operational conditions.

1.2 Objectives of the Research

The objectives of the research consist of the inter-comparison between high frequency, attenuating spaceborne radar measurements with ground-based polarimetric radar observations for the interpretation and calibration of space radar algorithms. This includes: the development of a method to ensure the proper processing of satellite and *in-situ* multi-parameter ground radar data in a common framework so that inter-comparison can be made on a point-by-point basis; the validation and calibration of space-based path-integrated-attenuation (PIA) correction algorithms - as well as reflectivity measurements, with ground radar observations; and, the estimation of the raindrop sized distribution (RSD) along the satellite beam for calibrating current space-based processing data products. More specifically, the tasks can be summarized as follows:

A. ***Common framework for processing***: Direct inter-comparisons between space and ground-based radars, on a point-by-point basis, can be a daunting task. Differences in viewing aspects between space and earth point observations, propagation frequencies, resolution volume size and time synchronization mismatch between space and ground-based measurements can contribute, in a significant way, to direct point-by-point inter-comparison errors. The problem is further complicated due to geometric distortions in PR data (e.g., shift, scale, shear, rotation, etc.) caused by the movements and attitude perturbations of the TRMM satellite itself. A method will be developed to optimally align PR and ground radar data with quality suitable for point-point inter-comparisons.

B. ***Comparison of path-integrated-attenuation (PIA)***: The TRMM PR operates at 13.8 GHz and is susceptible to a significant amount of attenuation during high storm events. This can impose severe limitation on its ability to precisely measure precipitation rainfall rates. The current PR algorithm uses a hybrid of two single-frequency techniques – the Hitschfeld-Bordan and surface reference technique (SRT), to correct for attenuation during both strong and weak precipitation events. Multi-polarimetric ground radar techniques for PIA correction (such as k-Z_h and k-K_{DP} relationships) are used to validate the current PIA correction method as well as to cross-validate PR reflectivity measurements.

C. ***RSD parameter characterization along the satellite radar beam***: Estimation of the RSD is critical to determining the precipitation medium, which can be used to characterize the attenuation effects. Comparisons of TRMM PR reflectivity measurements and PR attenuation corrected measurements with multi-polarimetric radar observations are conducted. The RSD parameters are estimated from SPOL ground radar using relationships given by the drop axial ratio, β, and the polarimetric observations Z_h, K_{dp} and Z_{dr}.

Radar measurements from the Tropical Rainfall Measuring Mission (TRMM) Precipitation Radar (PR), the National Center for Atmospheric Research (NCAR) S-Band polarimetric radar (SPOL) and the Doppler Weather Surveillance Radar (DWSR), the DWSR-93S (Kwajalein KPOL radar), are used. Data is collected from the TExas and FLorida UNderflights Experiment (TEFLUN-B) near Melbourne, FL; the Large Biosphere-Atmosphere Experiment in Amazonia (LBA) near Ji-Parana, Brazil; and, from the Kwajalein Island site located in the west Pacific.

1.3 Overview of the Dissertation

The dissertation is organized as follows:

Chapter 2 – Theoretical Background and Instrumentation

The theoretical foundation, and definition, for the polarimetric observables that will be used throughout the dissertation is summarized. Attention to specific theoretical formulation of hypotheses based on these parameters (e.g., raindrop size distribution), or other concepts, will be discussed, as appropriate, in the succeeding chapters, as described below. The operational characteristics of the TRMM PR, NCAR SPOL and Kwajalein KPOL radars are summarized.

Chapter 3 – Ground and Space-Based Radar Alignment Methodology

A methodology for aligning observations from a moving space radar (SR) platform with observations from a stationary, terrestrial-based, ground radar (GR) for the purpose of quantitative cross-validation and interpretation is presented. The method is based on matching low-intensity reflectivity profiles of storm cell contours from both radars across a horizontal plane. A key feature of the method is that it assumes that low-intensity contours are not subject to significant attenuation, which is an important consideration for high-frequency space-based radars. From this assumption it follows that SR and GR contours are, therefore, similar in size and shape, which can then be used for alignment purposes. Theoretical modeling is use to characterize the effects of attitude induced motions on satellite observations. Simultaneous space and ground-based measurements are used to validate theoretical modeling and the alignment methodology procedures.

Chapter 4 - Quantitative Estimation of TRMM PR Attenuation

Ground radar data is used to calibrate PR reflectivity and to independently estimate PR attenuation in the presence of a precipitating medium. Simulation is performed to determine ideal (non-attenuating) scattering relationships between S-band and K_u-band frequencies over a wide range of raindrop size distributions (RSD). Simulation results are used, along with GR data, to determine theoretical PR reflectivity for a given mean storm reflectivity. Comparison of quantitative results between the two instruments is presented.

Chapter 5 – Cross-Validation of TRMM PR Attenuation Correction with Ground Radar Polarimetric Observations

Theoretical relationships are determined between ground-based polarimetric observations, Z_h and K_{dp}, and expected values of *k*, for various hydrometeor types, along the SR beam path. Hydrometeor classification is performed based on a fuzzy-logic technique developed by Liu and Chandrasekar (2000), that uses GR polarimetric observations. The technique, applied to CHILL observations in Colorado, was modified for SPOL measurements taken during the TEFLUN-B and TRMM-LBA campaigns. The specific attenuation is integrated along the SR beam path to determine the total two-way PIA at each point along the beam. Measured SR reflectivity along with the derived PIA can be used to determine the *true* SR vertical reflectivity profile. This is demonstrated with *in-situ* data from TRMM field campaigns.

Chapter 6 – Evaluation of TRMM PR Attenuation Correction in Conjunction with Raindrop Size Distribution (RSD)

Comparison is made of the PR attenuation correction algorithm with estimates of the raindrop size distribution (RSD) along the PR beam path. Histograms of the three-parameter gamma distribution model are made along the vertical profile and compared with similar histograms of the difference between ground-based reflectivity measurements and PR attenuation corrected reflectivity measurements. Additionally, comparison of the rain rate estimate between the PR algorithm and ground radar measurements is made. Analysis of the initial PR RSD model values is performed and evaluated against ground radar observations.

Chapter 7 – Summary and Suggestions for Future Work

The results of the research are summarized and the major contributions of the dissertation are reviewed. Suggestions for future work are proposed.

Chapter 2

THEORETICAL BACKGROUND AND INSTRUMENTATION

2.1 Polarimetric Radar Observables

The forward scattering amplitudes of the electromagnetic wave incident on hydrometeors in the precipitating medium can be used to describe radar observations. Following the development of Bringi and Chandrasekar (2001), the incident plane wave, with linear polarization, in the far-field can be described by

$$\vec{E}^{i} = \hat{e}_{i}\, E_{0} \exp\left(-jk_{0}\hat{i} \bullet \vec{r}_{i}\right) \tag{2.1}$$

where E_o is the amplitude of the electric field (with the arrow above referring to vector form of the quantity), $\hat{e}_i$ is the unit vector that characterizes the linear polarization state which lies in the transverse plane, $\vec{r}_i$ is the position vector from the originating point to a point on the plane of constant phase, which is orthogonal to the direction of incidence (with $\hat{i}$ being the unit vector indicating this direction), and $k_o = 2\pi/\lambda$ being the wave number free space (where λ is the wavelength). The far-field scattered wave is then

$$\vec{E}^{s} = \frac{\vec{f}\left(\hat{s},\hat{i}\right)}{r}\exp\left(-jk_{0}r\right) \tag{2.2}$$

where $\bar{f}$ is the far-field scattering amplitude produced by the dipole moment of a dielectric particle, r is the magnitude of the position vector $(\bar{r})$ and $\bar{s}$ is the unit vector indicating the direction of the scattered plane wave. The scattered wave can be resolved into components as

$$\bar{E}^s = E_h^s \hat{h}_s + E_v^s \hat{v}_s \tag{2.3}$$

where h and v represent the horizontal and vertical polarization states, respectively. Using the forward scattering alignment (FSA) convention, equation (2.3) becomes

$$\begin{bmatrix} E_h^s \\ E_v^s \end{bmatrix} = \frac{e^{-jk_o r}}{r} \begin{bmatrix} S_{hh} & S_{hv} \\ S_{vh} & S_{vv} \end{bmatrix}_{FSA} \begin{bmatrix} E_h^i \\ E_v^i \end{bmatrix} \tag{2.4}$$

Defining the scattering matrix to be

$$S_{FSA} \equiv \begin{bmatrix} Shh & Shv \\ Svh & Svv \end{bmatrix}_{FSA} \tag{2.5}$$

where, in this convention, the first index of the scattering element refers to polarization from the backscattered field, and the second index refers to the polarization from the incident electric field, equation (2.5) can be written in more compact form as

$$\mathbf{E}^s = S_{FSA}\, \mathbf{E}^i \left(\frac{e^{-jk_o r}}{r} \right) \tag{2.6}$$

where boldface indicates a matrix quantity. In general, the elements (S_{ij}) of the matrix $\mathbf{S}_{FSA}$ will be complex.

For the most general case, the second-order moments of the scattering matrix, $\mathbf{S}_{FSA}$, can be grouped into a four-by-four covariance matrix, **W**. From the reciprocity theorem it can be shown that $S_{hv} = S_{vh}$, so that the covariance matrix reduces to a three-by-three dimension (Borgeaud et. al., 1987). Taking into account the distribution of the hydrometeor's properties (e.g., shape, canting angle, equivalent volume diameter, etc.), the covariance matrix, **W**, can be written as

$$\mathbf{W} = \begin{bmatrix} \left\langle |S_{hh}|^2 \right\rangle & \left\langle S_{hv} S_{hh}^* \right\rangle & \left\langle S_{vv} S_{hh}^* \right\rangle \\ \left\langle S_{hh} S_{hv}^* \right\rangle & \left\langle |S_{hv}|^2 \right\rangle & \left\langle S_{vv} S_{hv}^* \right\rangle \\ \left\langle S_{hh} S_{hh}^* \right\rangle & \left\langle S_{hv} S_{vv}^* \right\rangle & \left\langle |S_{vv}|^2 \right\rangle \end{bmatrix} \tag{2.7}$$

where $\langle \; \rangle$ denotes exception, and * denotes complex conjugate. Some qualitative characterization of the physical properties of the ensemble of hydrometeors present in the radar resolution volume can be deduced from elements of the covariance matrix (Doviak and Zrnic, 1993). A few of these are:

A. The reflectivity factor at horizontal polarization, can be expressed as

$$Z_h = \left(\frac{4\lambda^4}{\pi 4 |K_w|^2} \right) \left\langle |S_{hh}|^2 \right\rangle \qquad \text{mm}^6\ \text{m}^{-3} \tag{2.8}$$

where λ is the wavelength of the radar, $K_w = \frac{\varepsilon_r - 1}{\varepsilon_r + 2}$ is the dielectric factor of water and ε_r is the dielectric constant. In some sense, Z_h provides information about the size of the hydrometeor in the horizontal direction. An alternate expression for Z_h, is

$$Z_h = \frac{\lambda^4}{\pi^5 |K_w|^2} \int \sigma_h(D) N(D) dD \qquad (2.9)$$

where σ_h represents the hydrometeor radar cross section at horizontal polarization state.

B. The differential reflectivity can be expressed as

$$Z_{dr} = 10 \log\left(\frac{\langle |S_{hh}|^2 \rangle}{\langle |S_{vv}|^2 \rangle}\right) \quad \text{dB} \qquad (2.10)$$

which can be used to the deduce shape and orientation of the hydrometeors.

C. The linear depolarization ratio, which is the ratio of the received cross-polar power to the transmitted co-polar power, is defined as

$$LDR_{hv} = 10 \log\left(\frac{\langle |S_{hv}|^2 \rangle}{\langle |S_{vv}|^2 \rangle}\right), \text{ or} \quad \text{dB} \qquad (2.11)$$

$$\mathrm{LDR}_{vh} = 10\ \log\left(\frac{\left\langle |S_{vh}|^2 \right\rangle}{\left\langle |S_{hh}|^2 \right\rangle}\right) \qquad (2.12)$$

Depolarization of can occur due to such factors as the hydrometeor shape, oblateness, radar view angle and canting angle with respect to the axis of polarization (Herzegh and Jameson, 1982).

D. The correlation coefficient at zero lag is defined as

$$\rho_{hv}(0) = \frac{\left\langle S_{vv} S_{hh}^{*} \right\rangle}{\left\langle |S_{vv}|^2 \right\rangle^{0.5} \left\langle |S_{hh}|^2 \right\rangle^{0.5}} \qquad (2.13)$$

Which can be used to determine the orientation and shape of irregularly shaped hydrometeors.

For n number of spheroidal scatterers, with identical diameters of size D and axis ratio r (i.e., the ratio of minor axis to major axis), the specific differential phase can be written as

$$K_{dp} = \frac{2\pi n}{k_o} \mathrm{Re}\left[\hat{h} \bullet \vec{f}(r, D) - \hat{v} \bullet \vec{f}(r, D)\right] \qquad \text{deg. km}^{-1} \qquad (2.14)$$

where, Re indicates the real component of a complex quantity. For a medium composed of particles with size distribution N(D) (where, N(D) is the number of particles per unit volume with sizes in the interval D to D+ΔD) it follows that

$$K_{dp} = \frac{2\pi}{k_o} \mathrm{Re} \int N(D) \left\{ \hat{h} \bullet \vec{f}(r, D) - \hat{v} \bullet \vec{f}(r, D) \right\} dD \tag{2.15}$$

Fitting a power law of the form aD^b to $\hat{h} \bullet \vec{f}(r, D) - \hat{v} \bullet \vec{f}(r, D)$ the following empirical formula for specific differential phase is derived for S-band

$$K_{dp} = \frac{2\pi a}{k_o} \mathrm{Re} \int N(D) D^{4.24}\, dD. \tag{2.16}$$

Using similar formulation, the specific attenuation can be expressed as

$$k = 4.343\left(10^3\right) \int_D \sigma_{ext}(D) N(D) dD \qquad \text{dB km}^{-1} \tag{2.17}$$

where, σ_{ext} is the extinction cross section. Note that N(D) dD is in units m^{-3}. For scattering at frequencies between 3 and 15 GHz, and for drops in the range 0.1 < D < 8 mm, a power law, as a function of the drop diameter, D, can be fit to the extinction cross section so that equation (2.12) becomes

$$k \approx 4.343\left(10^3\right) \int_D D^{4.2}(D) N(D) dD. \tag{2.18}$$

2.2 Radar Systems and Locations

2.2.1 TRMM Precipitation Radar (PR)

The Tropical Rainfall Measuring Mission (TRMM) is a joint mission between the United States National Aeronautics and Space Administration (NASA) and the Japanese National Space Development Agency (NASDA). The TRMM satellite was launched into a 350 km circular orbit (nominal) at inclination of 35 degrees in November 1997. The Precipitation Radar (PR), onboard the satellite, is the first weather radar to be deployed in space, and is one of several instruments being used to measure the rainfall in the tropical and subtropical regions of the world. An illustration of the TRMM satellite showing the location of the PR is illustrated in Figure 2.1. The principle objectives of the radar

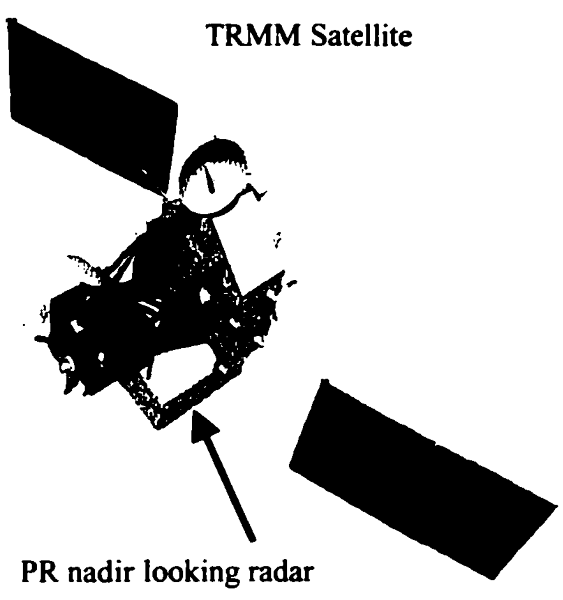

Figure 2.1: Illustration of TRMM satellite showing location of PR on the satellite.

are to: (1) provide a three-dimensional description of the rain profile, (2) obtain a quantitative estimation of rainfall over land and ocean and (3) improve the overall accuracy of precipitation retrieval algorithms by combined use of the active and passive systems on the TRMM satellite.

The PR is a nadir-pointing, single frequency K_u-band system that operates in the 13,796 to 13,802 MHz frequency range. The antenna is a 128-element WG planar array with aperture size of 2.0 x 2.0 meters. It transmits at a peak power of 500 W with a 1.6 microsecond pulse. The pulse repetition frequency (PRF) is 2776 Hz. The transmitter-receiver (T-R) consists of 128 solid state power amplifiers (SSPA) with each T-R element connected to a 2-meter slotted waveguide antenna. The system scans in the cross-track direction over $\pm$ 17 degrees from nadir creating a 215 km swath path near the earth surface. Each scan is completed in about 0.6 seconds. Meteorological observations are made from the earth's surface to 15 km in altitude with 250 meter vertical resolution and 4.3 km horizontal resolution (at the surface) at nadir. A more detailed description of the PR is given by Kummerow, et. al. (1998). A summary of the main features of the PR is given in Table 2.1.

Table 2.1: Summary of the Operating Characteristics of the TRMM PR

Antenna Specifications	
Type Size Directivity Beamwidth	128 element WG planar array 2.0 x 2.0 meters 44.5 dB (including waveguide loss) 0.71 x 0.71 degrees
Transmitter Specifications	
Type Frequency Peak Power Pulse Width Pulse Repetition Frequency (PRF) Observable Range	solid state power amplifier and low noise amplifier (128 channels) 13.796 to 13.802 GHz $\geq$ 500 W (at antenna input) 1.6 μs x 2 channels (transmitted pulse) 2776 Hz surface to 15 kilometers
Receiver Specifications	
Noise Figure Noise Power Typical Bandwidth Transfer Function Dynamic Range	 $\geq$ 70 dB dB
Parameters Available	
• Reflectivity at horizontal polarization (Z_h)	
Miscellaneous Specifications	
Swath Width Scan Angle Horizontal Resolution (nadir) Vertical Resolution (nadir)	215 kilometers $\pm$ 17 degrees 4.3 kilometers (at earth surface) 250 meters

2.2.2 SPOL Radar

The SPOL radar is a dual polarization S-band ground radar, which operates in the 2700 to 2900 MHz frequency range. A picture of the radar system, along with its support facilities, is shown in Figure 2.2 at the TRMM-LBA location. Used for meteorological research, the radar completed operational testing and became available for use in 1996.

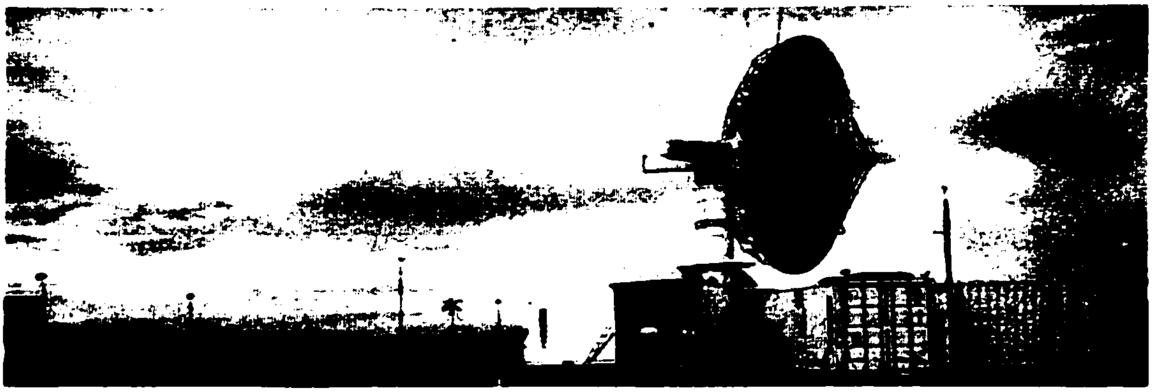

Figure 2.2: Picture of the SPOL showing the reflector antenna and support facility. The picture was at its location near Ji-Parana, Brazil during the TRMM-LBA field campaign.

The transmitter is an ASR-9 unit built by Westinghouse, and uses an air-cooled klystron that radiates one megawatt of power with a one microsecond pulse. The PRF can be adjusted from 325 to 1200 pulses per second with a tapered and filtered pulse to minimize radio frequency (RF) interference. The 8.5 meter parabolic reflector type antenna is a high-compliance aluminum structure that provides –30 dB first sidelobe and –35 dB integrated cross-polar isolation. Switching between horizontal and vertical polarization states is done by an NCAR built mechanical switch that provides 49 dB transmit isolation. A separate receiver is used for each channel, which provides 40 dB isolation at the receiver. The radar uses an NCAR designed VME-based Integrated Radar Processing Acquisition (VIRAQ) system for pulse-pair and dual polarization processing. The electronics consist of a dual range 90 dB digital intermediate frequency (IF) system with multiple C44 digital signal processing (DSP) chips that are controlled by a 486 central processing unit (CPU) running DOS (disc operating system). More information on the specifications and operating characteristics of the SPOL radar can be found at the NCAR website: http://www.atd.ucar.edu/rsf/spol/spol.html. A summary of its characteristics is given in Table 2.2.

Additionally, the system can be packed into six 20-foot sea containers for shipping to remote locations to support data collection in field campaigns worldwide: Measurements used in the dissertation were taken during the TEFLUN-B and TRMM-LBA campaigns near Melbourne, Florida and Ji-Parana, Brazil, respectively. The TEFLUN-B site was located about 26 km southwest (200° azimuth) of the Melbourne International Airport (at 27.8893333° north latitude, 80.7456° west longitude). The location of the radar relative to the city of Melbourne, FL is indicated by the circle, and is shown in Figure 2.3. The LBA site was located in the province of Rondonia in western Brazil close to the Bolivian border. The location is about 43.6 km southwest (200° azimuth) from the airport at Ji-Parana (at 11.2212633° south latitude, 61.998195° west longitude). The relative location of the radar site within Brazil is shown Figure 2.4 and is indicated by the circle.

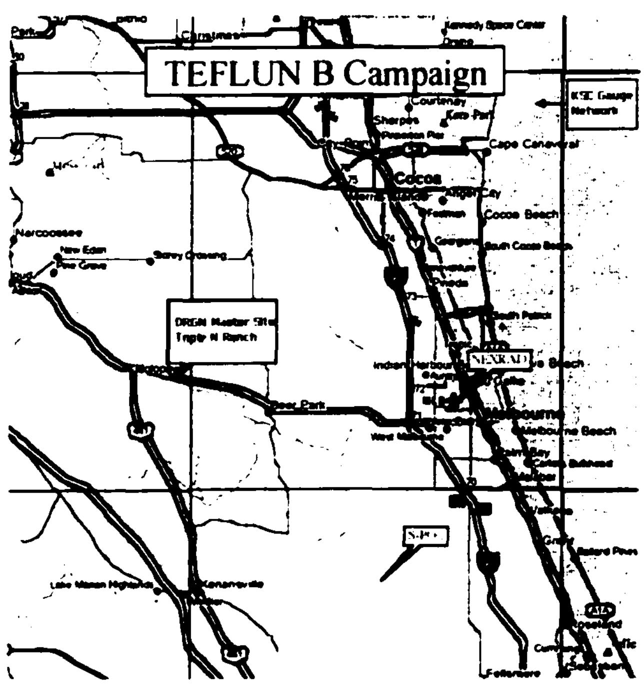

Figure 2.3: Location of SPOL during the TEFLUN-B campaign southwest of Melbourne International Airport. Circled is the location of the radar site.

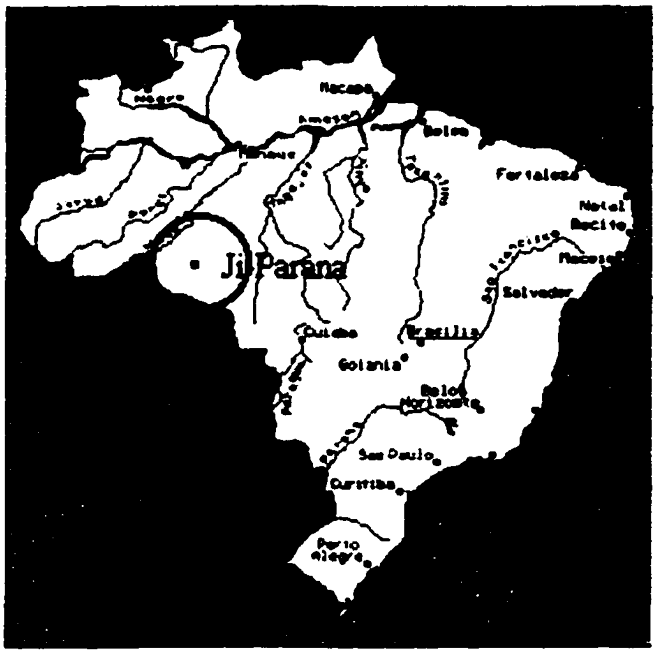

Figure 2.4: Location of SPOL during the TRMM-LBA campaign near Ji-Parana, Brazil. Circled is the location of the radar site.

Table 2.2: Summary of the Operating Characteristics of the SPOL Radar

Antenna Specifications	
Type	fully steerable, parabolic reflector
Size	8.5 meters in diameter
Gain	44.5 dB (including waveguide loss)
Beamwidth	0.91 degrees
Sidelobe Level	$\leq$ -30 dB
Cross-Polarization	$\leq$ -35 dB
Transmit Polarization States	linear polarization; horizontal or vertical
Transmitter Specifications	
Type	air cooled klystron, ASR-9
Wavelength	10.3 to 11.0 centimeters
Peak Power	> 1000 kW
Pulse Width	0.3 μs up to 1.4 μs - tapered
Pulse Repetition Frequency (PRF)	0 to 1300 Hz
Receiver Specifications	
Noise Figure	2.9 dB
Noise Power	-115.5 dBm
Typical Bandwidth	738 kHZ
Dynamic Range	90 dB
Parameters Available	
• Reflectivity at horizontal polarization (Z_h) • Differential reflectivity (Z_{dr}) • Co-Polar correlation coefficient ($\rho_{hv}(0)$) • Linear depolarization ratio (LDR) • Differential propagation phase shift (Φ_{dp})	
Processor and Software	
• VME-based Integrated Radar Acquisition (VIRAQ) system	
Miscellaneous Specifications	
Maximum Scan Rate	18 degrees/second each axis (30 degrees/second with pulley change)

2.2.3 Kwajalein WSR-93S (KPOL) Radar

The Kwajalein dual-polarimetric radar, pictured in Figure 2.5 (covered by radome), is a ground system located at Kwajalein island (8.7188889° north latitude, 167.713194° west longitude), in the Republic of the Marshall Islands, which is about 2,250 km east of the island of Guam and 3,380 km southwest of the Hawaiian islands, as shown in Figure 2.6. The radar is situated near the island's airstrip, as indicated in Figure 2.7. The system is a modified Doppler Weather Surveillance Radar (DWSR) 93S model, which operates with a wavelength of 10.71 cm. It transmits at a peak power of 500 kW (250 kW horizontal polarization state, and 250 kW vertical polarization state) with a 0.72 microsecond pulse. The PRF is variable between 369 to 960 Hz. Situated 24.8 m above mean sea level (msl), the 8.23 meter parabolic antenna is contained within an 11.5 meter radome. More information on the specific operational characteristics can be found in the KWAJEX experimental plan, edited by Yuter (1999). A summary of its characteristics is given in Table 2.3.

Figure 2.5: Picture of Kwajalein KPOL radar (covered by radome).

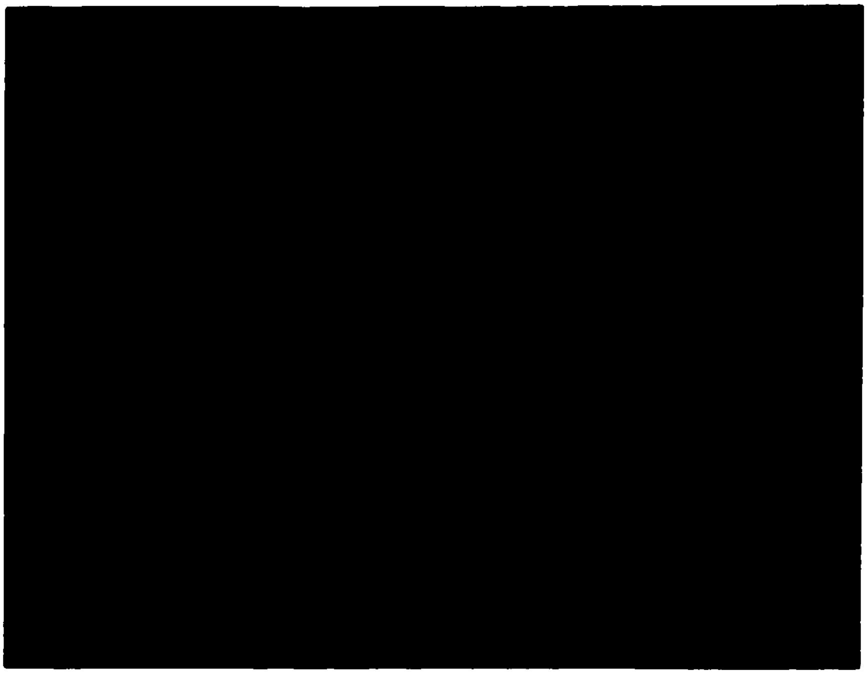

Figure 2.6: Location of Kwajalein Island in the Pacific Ocean.

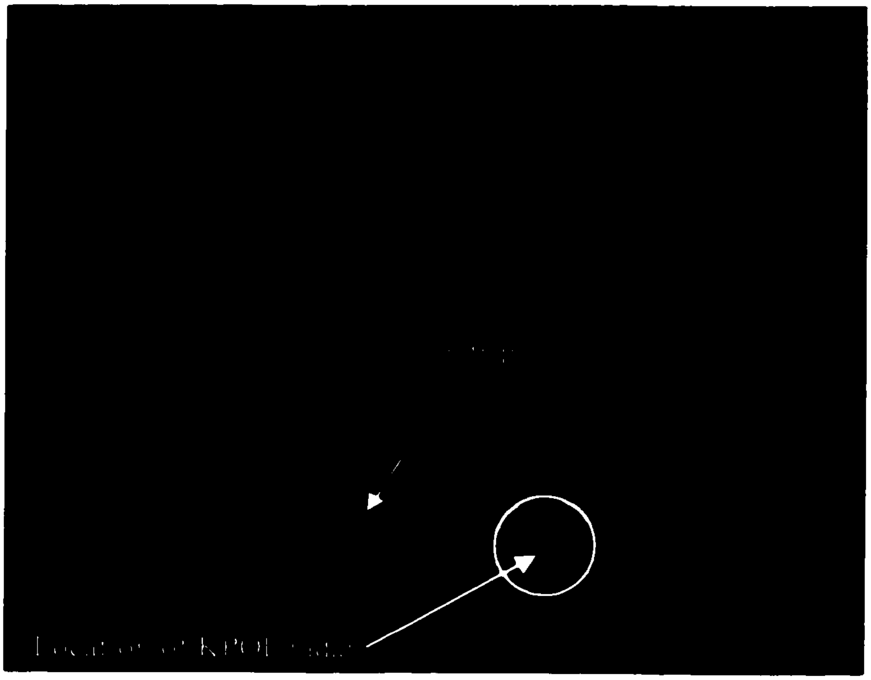

Figure 2.7: Location of KPOL radar on Kwajalein Island next to airstrip.

Table 2.3: Summary of the Operating Characteristics of the KPOL Radar

Radar	
Type	modified DWSR-93S
Antenna Specifications	
Type	parabolic
Size	8.23 meters (radome 11.5 meters)
Gain	45.1 dB
Beamwidth	1.12 degrees
Transmit Polarization States	linear polarization; horizontal or vertical
Transmitter Specifications	
Type	
Wavelength	10.71 centimeters
Peak Power	500 kW (250 kW horizontal/250 kW vertical)
Pulse Width	0.72 μs
Pulse Repetition Frequency (PRF)	396-960 Hz (up to four simultaneously)
Receiver Specifications	
Minimum Detectable Signal	-108 dBm
Parameters Available	
• Reflectivity at horizontal polarization (Z_h) • Differential reflectivity (Z_{dr}) • Differential propagation phase shift (Φ_{dp}) • Differential propagation phase shift (K_{dp}) • Mean doppler velocity (V_r) • Spectral width (SW)	
Processor and Software	
• Sigmet RVP7 and RCP02 • Iris software V7.05	
Miscellaneous Specifications	
Antenna Height Above Sea Level	24.8 meters
Maximum Scan Rate	20 degrees/second
Elevation Range	-0.4 to 90.5 degrees

Chapter 3

GROUND AND SPACE-BASED RADAR ALIGNMENT METHODOLOY

3.1 Overview of the Alignment Technique

A method has been developed that aligns space radar (SR) data with ground radar (GR) observations for the purpose of cross-validation of the two systems. Accurate and precise alignment of observations requires meticulous attention to detail that is important in minimizing measurement uncertainties between the two systems so that quantitative analysis of bias, attenuation and characterization of the microphysical properties of the atmospheric medium can be made along space radar beams via ground-based measurements. Reconciliation of the difference in resolution volumes between the two systems, due to size and orientation, and the need to align ground and space radar points have been previously investigated: Bolen and Chandrasekar (1999 and 2000a) used a correlation-shift procedure and a moment-based technique, respectively, for final alignment of points. The work of Bolen and Chandrasekar was motivated by the need to evaluate attenuation correction in space radar echo returns. An independent procedure, motivated by the need to match reflectivity, was presented by Anagnastou, et. al. (2001) who provided a comprehensive study comparing space radar with ground radar reflectivity measurements. The method presented in the thesis uses a variable volume matching scheme with a polynomial technique for alignment of SR and GR points. A theoretical modeling of potential alignment errors is first performed to determine the expected magnitude of the errors, and to analyze their impact on the inter-comparison.

The alignment methodology is then demonstrated using data collected from the TRMM PR and SPOL radars on August 13, 1998. The procedure is also applied to simultaneous data sets taken between TRMM PR and the Kwajalein KPOL radars on July 10, 2000 as further illustrations of the alignment method.

Inter-comparisons between ground radar and spaceborne radar on a point-by-point basis can be a difficult and challenging task. Errors result from the mismatch between GR and SR resolution volume, spatial image alignment and operating frequencies. Differences in viewing aspects and resolution contribute to the inter-comparison error, which results from the measurement of return signals from different volumes of the precipitation medium, as illustrated in Figure 3.1. Inter-comparison is further complicated by geometric distortion introduced into the satellite data (e.g., shift, scale,

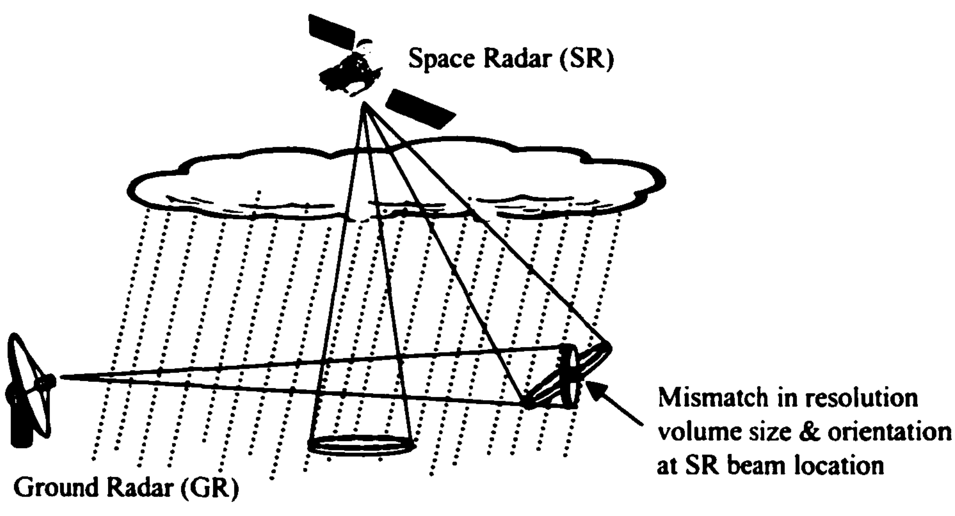

Figure 3.1: Illustration of the viewing geometry for ground and space-based radar systems. Note the difference in size and orientation of the resolution volumes between the two systems, which results in measurement mismatch error.

shear, rotation, etc.), which is caused by the movements and attitude perturbations of the satellite itself (Schowengerdt, 1997). Attitude motions such as roll, pitch and yaw, as depicted in Figure 3.2(a), introduce variabilities into the retrieved satellite radar image that are not systematic in nature creating relative spatial alignment error between SR and GR images. Changes in the satellite altitude and velocity, due to orbit eccentricity, can also produce geometric distortion. The types of distortion caused by these perturbations are illustrated in Figure 3.2(b). Differences in operating frequencies can also make it difficult to find alignment points (i.e., common reference points between the two radar images). Furthermore, attenuation, and non-Rayleigh scattering, of high-frequency space-based measurements (Bolen and Chandrasekar, 2000) can make the task of finding common points between return signals problematic in high-intensity storm regions. A method has been devised to minimize inter-comparison error. The methodology is described in more detail in the following sections, and is validated using *in-situ* data collected during the TRMM field campaigns.

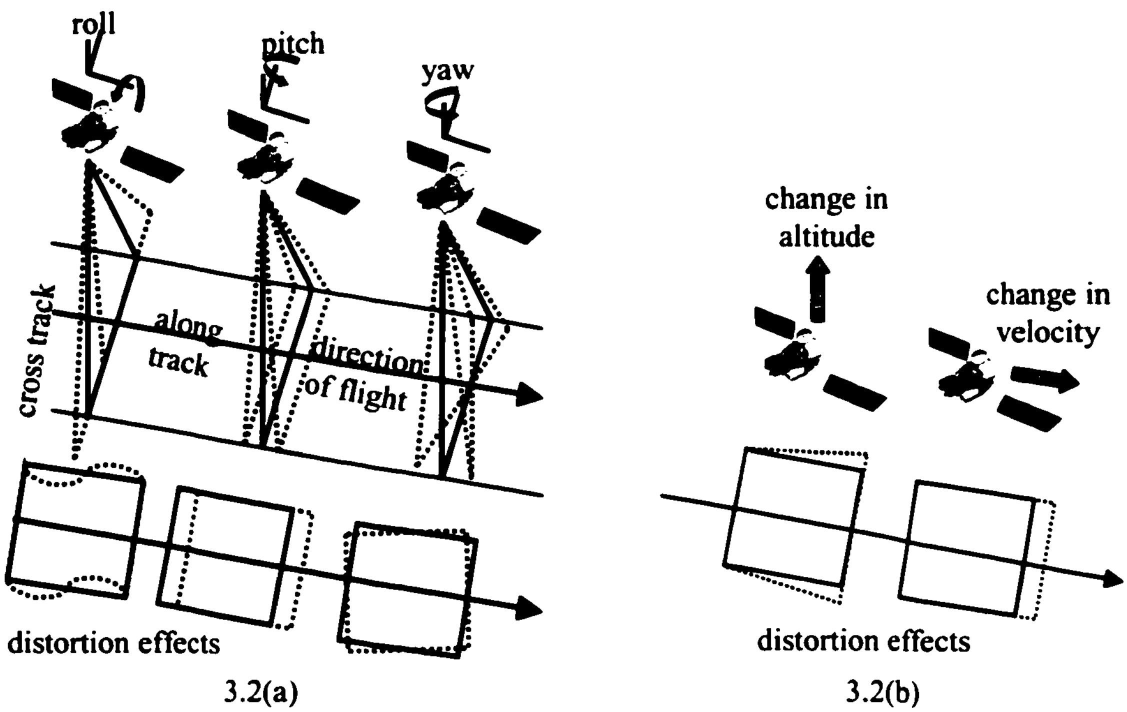

Figure 3.2: Illustration of the types of platform motion that can cause geometric distortion in the space-based radar image. (a) Distortion caused by the satellite attitude perturbations: roll, pitch and yaw. (b) Distortion caused by the satellite motions along its flight track. Changes in attitude and velocity are due to the characteristics of a non-circular orbit trajectory.

3.2 Alignment Methodology

To minimize errors, ground and space-based data are collected during simultaneous intervals not exceeding 2-3 minutes in time difference. Small windows approximately 50 x 50 km in size (in a horizontal plane) are defined around a precipitation cell of interest so as to minimize non-linear spatial geometric distortion effects. Both ground and space-based data are re-mapped to a satellite-centered Cartesian coordinate system using a non-spherical earth model (WGS-84 model). For a cross-track, line scanning system, such as that employed by the TRMM PR, the coordinate system origin is located at the intersection of the satellite ground track and scan line that passes through the center of the storm area. The re-sample angle is taken such that the spaceborne radar line of scan becomes orientated perpendicular to the x-axis of the re-sampled coordinate grid. Both space and ground-based data are sampled to grids spaced 0.5 km horizontally and 0.25 km in altitude. A 4/3-earth radius model is used during sampling of the ground radar data to compensate for radar beam refraction. The coordinate re-sampling scheme is illustrated in Figure 3.3 showing ground radar data collected during the TEFLUN-B campaign on August 13, 1998.

Common reference points (or, point-pairs) are then found between the ground and space radar data sets. The procedure begins by finding the (x,y) coordinates of each SR beam location, derived from satellite ephemeris and PR pointing data, in a horizontal plane at a nominal altitude. A three-dimensional set of reflectivity points is averaged in linear scale (units $mm^6\ m^{-3}$) at each of the beam locations in both the horizontal and vertical directions in order to match the resolution volumes. The horizontal and vertical limits are taken as the maximum extent of either the SR or ground radar resolution at the SR beam location, which is calculated according to the geometry described in (Meneghini and Kozu, 1990). The average value of reflectivity computed in the volume is taken as the satellite measured reflectivity, $Z_m(SR)$, at that (x,y) location. Next, the points that comprise the volume are translated in x, y and z (i.e., along both horizontal directions and in the vertical direction) in the ground radar reflectivity data set, starting

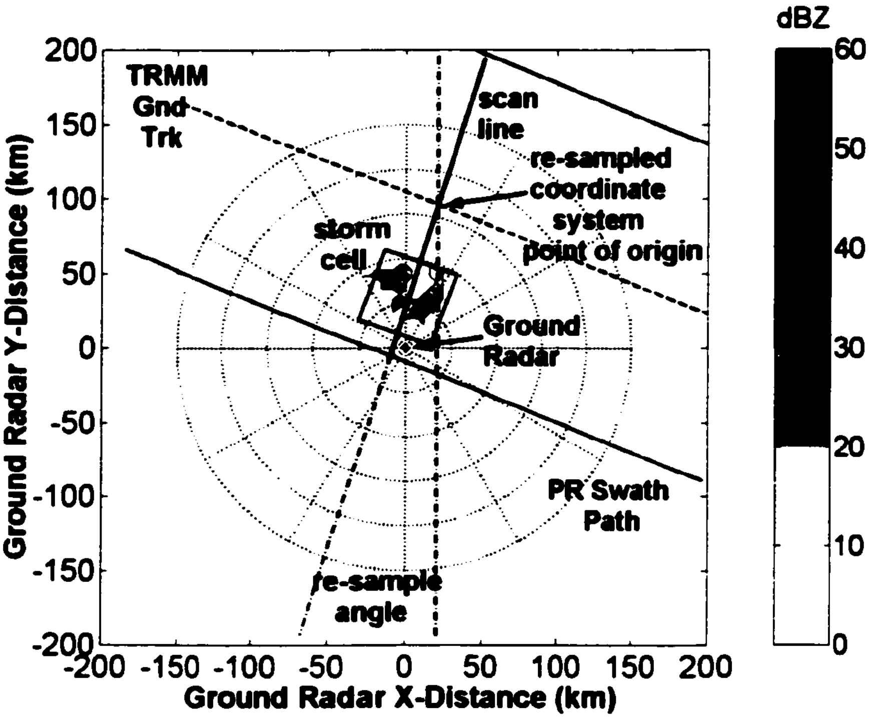

Figure 3.3: Radar data re-mapping to space radar centered Cartesian coordinate system. Shown is the mapping coordinate system point of origin and re-sample angle. The example shows GR reflectivity data at 2 km CAPPI re-sampled to 4 km horizontal resolution on August 13, 1998 near Melbourne, FL. The overlay is the TRMM PR with the ground track shown as a dotted line, PR swath path as a solid line, and PR scan as solid line bisecting the meteorological region of interest.

from the SR beam location, (x,y). The value computed is taken as the ground radar measured reflectivity, $Z_m(GR)$, at location (x,y). The three-dimensional volume and illustration of the shift are shown in Figure 3.4.

A ground-space radar point-pair is established when a shift in (x,y,z) is found that minimizes a cost function based on the volume-averaged space and ground radar reflectivities, Z_m(SR) and Z_m(GR), and the Euclidean distance of the volume shift. Since it is assumed that the effect of attenuation is not significant on either radar at low reflectivity contour levels at the edges of the storm cell, only volumes that result in GR

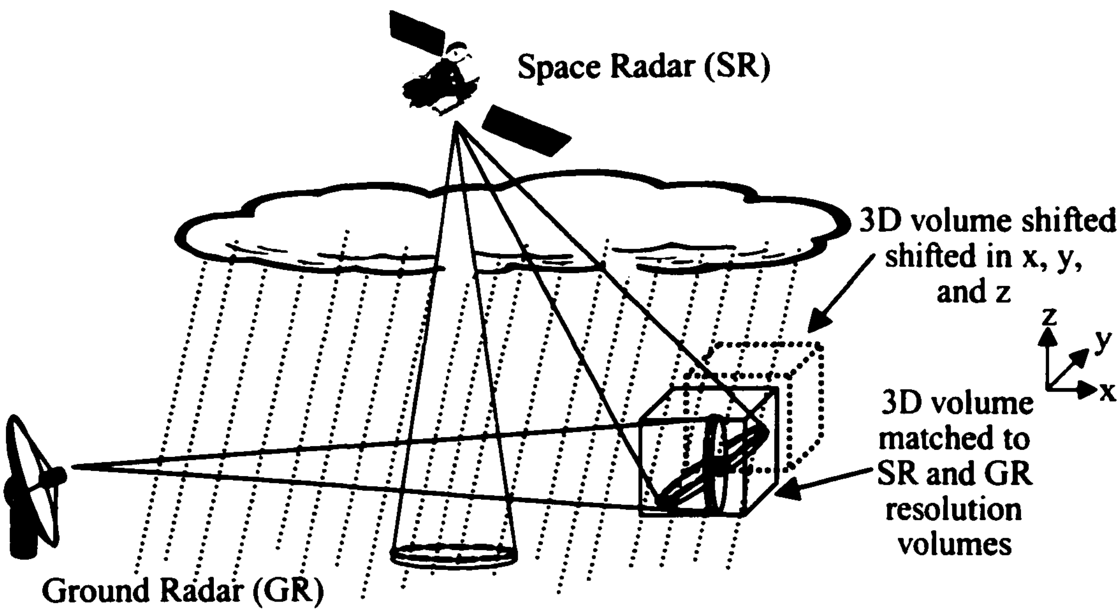

Figure 3.4: Illustration of 3D volume matching and shifting based on GR and SR resolution volumes. The location of the SR beam is found at a nominal altitude, shown here at the 2km altitude. The solid line cube represents SR reflectivity that is arithmetically averaged within the matched resolution volume, and the dotted cube represents the same set of points (i.e., the same volume) shifted in GR reflectivity space.

reflectivities less than 30 dBZ are considered as possible candidates for establishing a point-pair relationship. The cost function (CF), is normalized based on the expected error in reflectivity measurements and PR beam location measurements, and is given by

$$CF = \frac{\sqrt{\Delta x^2 + \Delta y^2 + \Delta z^2}}{\sigma_d} + \left| \frac{Z_m(PR) - Z_m(GR) + bias}{\sigma_m} \right| \qquad (3.1)$$

where Δx, Δy and Δz are the incremental volume shift distances, $\sigma_d = \sqrt{\sigma_x^2 + \sigma_y^2 + \sigma_z^2}$ is the expected error associated with the satellite geolocation and beam pointing errors (derived from nominal satellite operational position vector and attitude errors in the horizontal and vertical directions denoted by σ_x, σ_y and σ_z) and σ_m is the reflectivity measurement uncertainty of the two systems. Computation time is reduced by considering only shifts within the distance of $2\sigma_d$. Finally, in order to minimize any potential calibration bias between space and ground radar measurements, a *bias* term is introduced into the second term on the right hand side of equation (3.1). The bias is determined by taking the difference of the arithmetic mean between the space and ground radar reflectivities over a three-dimensional volume with dimensions of σ_x, σ_y and σ_z centered about the SR beam location.

Once the set of point-pairs is found, a polynomial fit is used to determine the appropriate mapping of the space radar image to the ground radar image. Following the development of Schowengerdt (1997), a polynomial of order N can be used to relate the coordinates of the contour of the distorted spaceborne image ($x_c(SR)$,$y_c(SR)$) to the corresponding ground radar contour coordinates ($x_c(GR)$,$y_c(GR)$) via

$$x_c(GR) = \sum_{i=0}^{N} \sum_{j=0}^{N-i} \alpha_{ij}\, x_c(SR)^i\, y_c(SR)^j \tag{3.2}$$

$$y_c(GR) = \sum_{i=0}^{N} \sum_{j=0}^{N-i} \beta_{ij}\, x_c(SR)^i\, y_c(SR)^j\,. \tag{3.3}$$

The coefficients, α and β, are determined and applied to the entire SR data set, thereby mapping the space radar image to the ground radar image. The level of detail that can be approximated in the fit depends on the order of the polynomial. Usually, a quadratic polynomial in x and y (i.e., 6 coefficients) is sufficient for most satellite remote sensing applications (Schowengerdt, 1997). This type of transformation method can be used to reduce the effects of shift, scale, shear, rotation, etc. between the two images. For the set of SR data coordinate locations (x(SR),y(SR)) and GR data locations (x(GR),y(GR)), equation (3.2) can be written in the general vector-matrix form, for 6 coefficients and *m* point-pairs, as

$$\begin{bmatrix} x(GR)_1 \\ x(GR)_2 \\ \vdots \\ x(GR)_m \end{bmatrix} = \begin{bmatrix} 1 & x(SR)_1 & y(SR)_1 & x(SR)_1 y(SR)_1 & x(SR)_1^2 & y(SR)_1^2 \\ 1 & x(SR)_2 & y(SR)_2 & x(SR)_2 y(SR)_2 & x(SR)_2^2 & y(SR)_2^2 \\ \vdots & \vdots & \vdots & \vdots & \vdots & \vdots \\ 1 & x(SR)_m & y(SR)_m & x(SR)_m y(SR)_m & x(SR)_m^2 & y(SR)_m^2 \end{bmatrix} \begin{bmatrix} \alpha_{00} \\ \alpha_{10} \\ \alpha_{01} \\ \alpha_{11} \\ \alpha_{20} \\ \alpha_{02} \end{bmatrix} \qquad (3.4)$$

or, in more compact form as

$$\mathbf{X}(GR) = \mathbf{WA} \qquad (3.5)$$

where bold-faced represents vector, or matrix, form with **X**(GR) being the vector of GR x-coordinates, W being the matrix with structure shown in the first product on the right-hand-side of equation (3.5) and **A** being the vector of α-coefficients that map SR observation locations to GR x-coordinate locations. The mapping of SR coordinates to GR y-coordinates in equation (3.3) can be written in vector-matrix form similar to equation (3.5), and also in the more compact form

$$Y(GR) = \mathbf{WB}. \quad (3.6)$$

with **Y**(GR) being the vector of GR y-coordinates, **W** as described before for equation (3.5) and B being the vector of β-coefficients that map SR observation locations to GR y-coordinate locations. Special physical interpretation can be placed on each of the coefficients contained in **A** and **B** as components to the total 'warp,' or geometric distortion, in the space radar image. A summary of the properties for both x- and y-coordinate coefficients is listed in Table 3.1

Table 3.1: Physical meaning of coefficients to the total "warp" in the space radar image. (Schowengerdt, 1997)

Coefficient	Warp Component
α_{00}	shift in x
β_{00}	shift in y
α_{10}	scale in x
β_{01}	scale in y
α_{01}	shear in x
β_{10}	shear in y
α_{11}	y-dependent scale in x
β_{11}	x-dependent scale in y
α_{20}	nonlinear scale in x
β_{02}	nonlinear scale in y

If the number of point-pairs is equal to the number of polynomial coefficients, (e.g., m = 6 for a second order polynomial), the ideal error in the polynomial fit would be zero. However, since some point-pairs may be in error (e.g., due to incorrect volume matching), it is desirable to find more pairs, such that the number of point-pairs is more than the number of coefficients in order to minimize the impact of incorrect matching. In this case, (3.5) and (3.6) can be written as

$$\mathbf{X}(GR) = \mathbf{WA} + \varepsilon_x \tag{3.7}$$

$$\mathbf{Y}(GR) = \mathbf{WB} + \varepsilon_y \tag{3.8}$$

where ε_x and ε_y represent the possible location errors between point-pairs associated with GR x and y-coordinates, respectively. Solutions to (3.7) and (3.8) can be found by minimizing the least squared error vectors as

$$\min\left[\varepsilon_x^T \varepsilon_x\right] = \left(\mathbf{X}(GR) - \mathbf{W}\hat{\mathbf{A}}\right)^T \left(\mathbf{X}(GR) - \mathbf{W}\hat{\mathbf{A}}\right) \tag{3.9}$$

$$\min\left[\varepsilon_y^T \varepsilon_y\right] = \left(\mathbf{Y}(GR) - \mathbf{W}\hat{\mathbf{B}}\right)^T \left(\mathbf{Y}(GR) - \mathbf{W}\hat{\mathbf{B}}\right) \tag{3.10}$$

where T represents transpose and $\hat{\mathbf{A}}$, and $\hat{\mathbf{B}}$ are the generalized-inverse solutions given by

$$\hat{\mathbf{A}} = \left(\mathbf{W}^T \mathbf{W}\right)^{-1} \mathbf{W}^T \mathbf{X}(GR) \tag{3.11}$$

$$\hat{\mathbf{B}} = \left(\mathbf{W}^T \mathbf{W}\right)^{-1} \mathbf{W}^T \mathbf{Y}(GR) \tag{3.12}$$

where $\hat{\mathbf{A}}$ and $\hat{\mathbf{B}}$ represents the solution using generalized-inverse. If some measure of confidence between point-pairs can be determined, then a weighted least-squares solution can be employed which minimizes the least squared error vectors (Brogan, 1982)

$$\min\left[\varepsilon_x^T \varepsilon_x\right] = \left(\mathbf{X}(GR) - \mathbf{W}\hat{\mathbf{A}}\right)^T \mathbf{Q}\left(\mathbf{X}(GR) - \mathbf{W}\hat{\mathbf{A}}\right) \tag{3.13}$$

$$\min\left[\varepsilon_y^T \varepsilon_y\right] = \left(\mathbf{Y}(GR) - \mathbf{W}\hat{\mathbf{B}}\right)^T \mathbf{Q}\left(\mathbf{Y}(GR) - \mathbf{W}\hat{\mathbf{B}}\right) \tag{3.14}$$

with the solutions $\hat{\mathbf{A}}$ and $\hat{\mathbf{B}}$ given by

$$\hat{\mathbf{A}} = \left(\mathbf{W}^T \mathbf{Q} \mathbf{W}\right)^{-1} \mathbf{W}^T \mathbf{Q} \mathbf{X}(GR) \tag{3.15}$$

$$\hat{\mathbf{B}} = \left(\mathbf{W}^T \mathbf{Q} \mathbf{W}\right)^{-1} \mathbf{W}^T \mathbf{Q} \mathbf{Y}(GR). \tag{3.16}$$

Here, $\mathbf{Q}$ is a non-singular diagonal matrix such that its elements, q_{ij}, are related to the expected confidence in the j^{th} point-pair matching (for $i = j$, and equal to zero for $i \neq j$). That is to say, given the cost function values computed from equation (3.1) a relative measure of confidence can be determined corresponding to the validity in the establishment of a particular ground-space radar contour point-pair matching. It is assumed that point-pairs that have a relatively low minimum cost function value are more closely matched than point-pairs with higher CF values. Each element, q_{ij}, in **Q**, is determined from the cost function in the following way

$$q_{ij} = \begin{cases} \max[CF] - CF_j + \min[CF] & i = j \\ 0 & i \neq j \end{cases} \tag{3.17}$$

where CF_j is the cost function of the j^{th} pair. For the set of point-pairs, the maximum and minimum cost functions are found and the elements, q_{ij}, of the **Q** matrix are determined according to equation (3.17). This ensures that pairs with smaller cost functions are weighted more than pairs with larger cost functions in the weighted least-squares solution. This also ensures that no diagonal element of **Q** is equal to zero.

In practice, it may be possible that one or more point-pairs could have cost function values that are the same, or nearly the same. Because of this, several point-pair sets could be reasonably established between the ground and space radar storm cell contours. For this reason, the difference in GR and SR volume matched reflectivity values is taken in the 20-30 dBZ range. The set of point-pairs that minimizes the standard deviation of the difference is taken as the valid point-pair set. This approach minimizes the possibility of selecting the incorrect set of point-pairs, and also has the effect of selecting a point-pair set that minimizes the scatter between GR and PR reflectivity observations. Finally, alignment in the vertical direction between space and ground radar measurements can also be made from Δz: the shift in the vertical that minimizes the cost function.

3.3 Misalignment Effects on Data Matching

3.3.1 Theoretical Uncertainty in SR Beam Location

Matching SR and GR resolution volumes to take into account variations in resolution size and orientation between the two systems is a straightforward notion. However, the necessity to account for geometric warping in SR data retrieval may seem less obvious. Satellite attitude perturbations, such as roll, pitch and yaw, can produce displacement shifts or rotation in the SR return image. Uncertainties associated with these types of movements can potentially be significant leading to localized distortion in SR observations relative to GR measurements; most notably near the edges of the SR swath path. In principle, for a nadir-looking, scanning system, like the TRMM PR, the magnitude of the variations can be determined from the satellite ephemeris: satellite altitude; off-nadir scan and roll angle perturbation in the cross-track direction; and, pitch angle perturbation in the along-track direction. As shown in Figure 3.5, for a given off-nadir scan angle, θ, with the satellite at nominal altitude, h, the displacement δy in the cross-track direction, due roll perturbation angle $\delta\theta$, can be determined as follows:

From the Law of Sines, the angle β_c, can be determined from $\frac{\sin\beta_c}{(r_e + h)} = \frac{\sin\theta}{r_e}$, where r_e is the earth radius, which is

$$\beta_c = \sin^{-1}\left[\frac{(r_e + h)}{r_e}\sin\theta\right]. \tag{3.18}$$

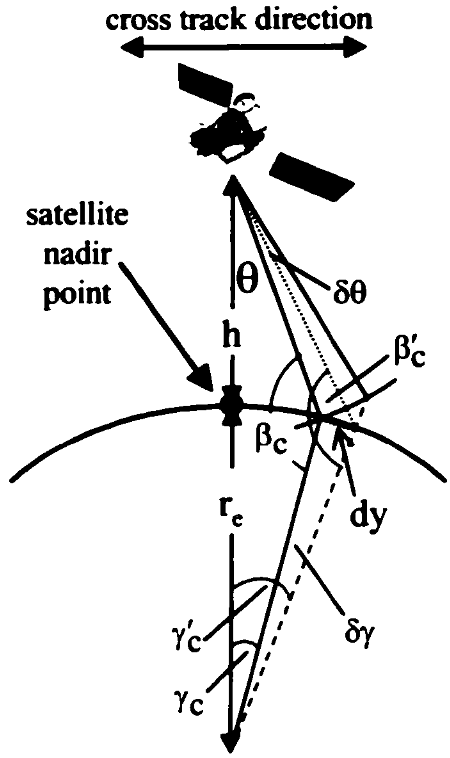

Figure 3.5: Geometry for determining the magnitude of cross-track position perturbation due to attitude roll motion.

The central angle γ_c, which subtends the arc from the satellite nadir point to the expected beam location at scan angle θ, is $\gamma_c = 180 - \beta_c - \theta$. Likewise, the central angle with roll perturbation δθ can be determined from similar geometric analysis, which yields

$$\beta'_c = \sin^{-1}\left[\frac{(r_e + h)}{r_e}\sin(\theta + \delta\theta)\right] \tag{3.19}$$

from which it follows that $\gamma'_c = 180 - \beta'_c - \theta - \delta\theta$ (where the *accent* denotes perturbation-induced quantities). The cross-track shift can then be found via

$$\frac{\left(\frac{dy}{2}\right)}{r_e} = \sin\left(\frac{\delta\gamma_c}{2}\right) \tag{3.20}$$

where, $\delta\gamma_c = \gamma'_c - \gamma_c$. Simplification yields the following result for the cross-track shift due to roll perturbation

$$dy = 2r_e \sin\left(\frac{\delta\gamma_c}{2}\right). \tag{3.21}$$

Using the expressions for γ_c and γ'_c in the expression for $\delta\gamma_c$, and substituting into equation (3.21) the following equation can be derived for the cross-track displacement due to roll perturbation

$$dy = 2r_e \sin\left(\frac{\beta_c - \beta'_c - \delta\theta}{2}\right). \tag{3.22}$$

Derivation of the along-track shift, dx, due to pitch angle perturbation $\delta\phi$, is determined in similar fashion with the exception that there is no scan angle in the along-track direction. The along-track shift is

$$dx = 2\, r_e \sin\left(\frac{\beta_a - \beta'_a - \delta\phi}{2}\right) \tag{3.23}$$

where β_a has an analogous meaning as β_c, but in the along-track direction, and is given by

$$\beta_a = \sin^{-1}\left[\frac{(r_e + h)}{r_e}\right] \tag{3.24}$$

and, likewise, the angle after perturbation is

$$\beta'_a = \sin^{-1}\left[\frac{(r_e + h)}{r_e}\sin(\delta\phi)\right]. \tag{3.25}$$

The potential cross-track displacement error for off-nadir scan angles between 0-17 degrees with roll angle uncertainty 0.2 degrees is plotted in Figure 3.6 for a satellite platform at a nominal altitude of 350 km. Note that the magnitude of the displacement

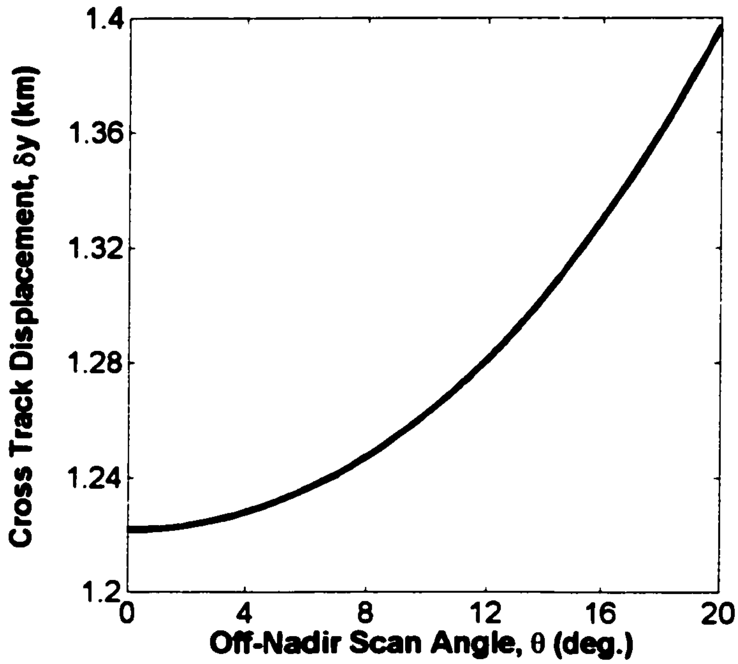

Figure 3.6: Plot of potential cross-track displacement caused by attitude roll motion assuming 0.2 degrees of attitude uncertainty. Note that the off-nadir angle of 0 degrees also corresponds to the potential displacement in the along-track position due to pitch motion.

shift at scan angle 0 degrees is also the magnitude of the along-track shift if pitch angle uncertainty is also assumed to be 0.2 degrees. As scan angle increases, the displacement due to attitude perturbation is also seen to increase. For the PR, with nominal 4.3 km resolution near the earth surface, displacement shift, due to roll perturbation, can be as large as about 1.34 km in cross-track and about 1.23 km in the along-track direction due to pitch perturbation (as indicated at the 0 degree off-nadir scan).

Geometric distortions, due to yaw perturbation effects with uncertainty angle $\delta\rho$, are of the form

$$x' = y \sin(\delta\rho) \tag{3.26}$$

$$y' = y \cos(\delta\rho) \tag{3.27}$$

where x and y are the SR along-track and cross-track beam locations, respectively (with the *accent* indicating the coordinates due yaw uncertainty). For yaw uncertainty of 0.2 degrees, cross-track displacement is minimal. However, the along-track shift can be as large as 0.35 km near the SR swath edge at about 100 km. Taking into account yaw and pitch perturbation, the total along-track shift could, therefore, be as large as 1.6 km with rotation accounting for nearly 20% of the displacement. Finally, satellites operating in non-circular orbits can undergo uncertainty variations in altitude and along-track velocity. These types of variations are the result of the non-sphericity of the earth and orbit eccentricity. Depending on the magnitude of the uncertainties, these can contribute to geometric warping, but are small for the PR.

3.3.2 Geometric Distortion Effects in SR Data

High-resolution reflectivity measurements taken from the Colorado State University (CSU) CHILL radar during the STEPS campaign on June 23, 2000 were used to simulate TRMM PR observations in order to determine the magnitude of the effects of geometric distortion on SR data. A cross-sectional profile of the CHILL data at 2 km CAPPI (constant altitude planned position indicator) is shown in Figure 3.7(a) sampled at 0.5 km resolution. The CHILL reflectivity measurements (Z_h) were degraded in resolution to simulate the effects of matching PR resolution volume to the ground radar resolution, as described in preceding sections. The resulting image is shown in Figure 3.7(b). A 1 dB zero mean Gaussian noise was added to the matched resolution data to simulate the measurement uncertainty in PR reflectivity data as described in the TRMM Science User Interface Control Specification (1999). The reflectivity field was then warped according to the polynomial coefficients: **A** = [0.8254000 cos(0.0034970) sin(0.0034970) -0.000070 0.000001 0.000650]^T, **B** = [-0.284600 -sin(0.0034970) cos(0.0034970) -0.000010 0.000000 0.000000]^T , and **C** = 0.0 (where **C** is the altitude uncertainty) to simulate geometric distortion in PR observations. Here, the distortion is primarily due to shift and rotation (about 0.2 degrees) with very small amounts of other distortion. The distorted, or warped Z_h field, is shown in Figure 3.7(c). The total area $\geq$ 20 dBZ after warping is about 2.5% larger than the area before warping. That is, in this example, the warping increased the total area of the storm cell by about 2.5% using the 20 dBZ contour as a measure. The reflectivity was averaged in $\log_{10}$ scale (henceforth referred to as log scale with subscript omitted) across horizontal planes for both the true and warped reflectivity fields at 0.5 km vertical increments ranging from 0 to 15 km. The averages were plotted with respect to altitude as shown in Figure 3.8: where the true reflectivity is depicted with a solid line and the warped reflectivity with a dotted line. The difference between true and warped reflectivity is seen to be as much as 1.4 dB.

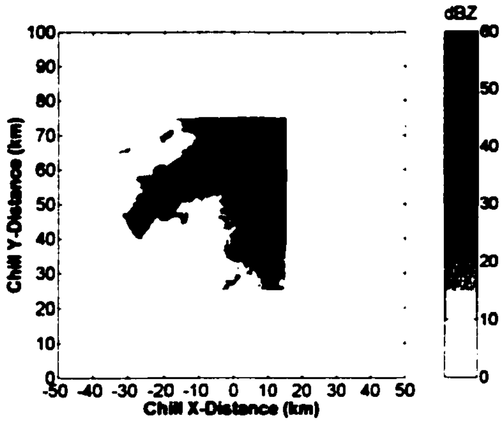

3.7(a)

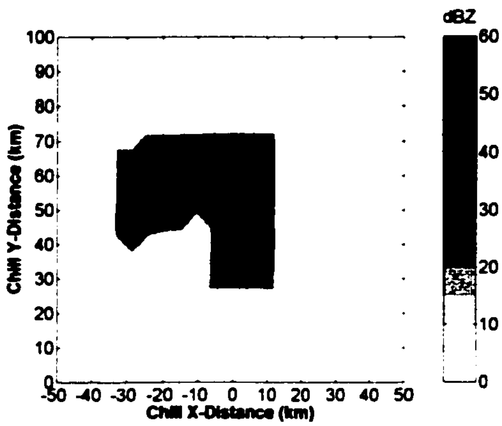

3.7(b)

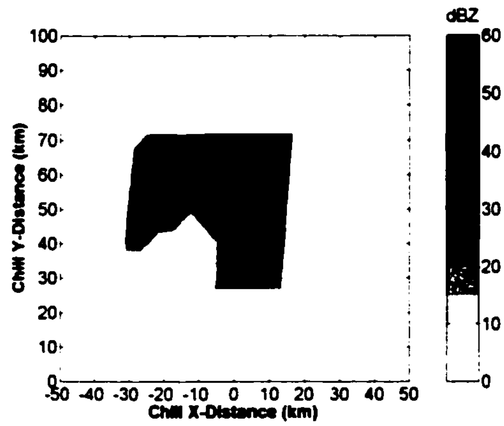

3.7(c)

Figure 3.7: Simulation of TRMM PR reflectivity using CHILL data taken from the STEPS campaign on June 23, 2000: (a) CHILL data image at 2 km CAPPI before simulation shown at 0.5 km horizontal resolution, (b) simulated PR reflectivity image with resolution assumed to be 4 km in the horizontal and matched to CHILL beamwidth in the vertical, and (c) PR reflectivity image of (b) with geometric warping introduce and 1 σ noise added.

From modeling, it is found that geometric warping, due to satellite motions, can affect the magnitude of the measured reflectivities. Geometric distortion is a non-linear effect, which introduces *non-systematic* variabilities into the retrieved SR image. This has an especially acute effect on non-homogeneous radar observations. In this example, the radar image is spatially "warped" in a non-linear way creating a distorted ratio of high-intensity area to low-intensity area. This is evident in comparison of Figure 3.7(b) with Figure 3.7(c) where the high intensity area in the upper right corner of image has become exaggerated due to warping compared to other parts of the image. The effect of warping introduces a bias on average of 1.0 dB into the retrieved PR measurements for log-averaged reflectivity below 9 km, as shown in Figure 3.8.

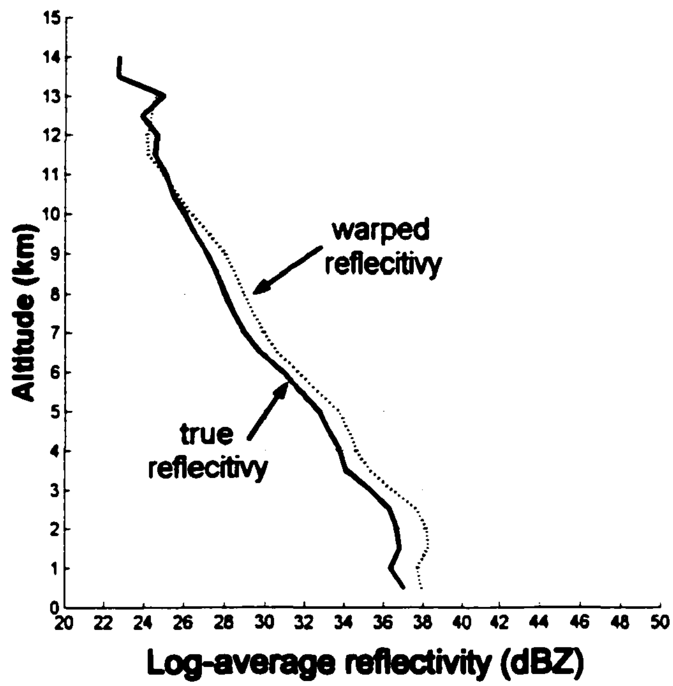

Figure 3.8: Plot of log-average Z_h vs. altitude from simulated PR data. The solid line indicates the true reflectivity and the dashed line indicates the warped reflectivity. The difference between true and warped images is as much as 1.4 dB in offset.

From modeling, it can perhaps be concluded that geometric distortion is a possibility, and that effect on measurements could be equal to the measurement uncertainty in magnitude. It is logical then to ask whether or not this effect is truly seen in real data. Radar observations were collected during the TRMM TEFLUN-B field campaign, which are used to validate the proposed procedure for aligning SR with GR measurements.

3.4 Alignment Examples with In-Situ Data

An example of the polynomial technique to correct for geometric warping is applied to TEFLUN-B data taken on August 13, 1998 using TRMM PR and SPOL data. A polynomial fit was determined between point-pairs found for PR and SPOL images. For this example the α-coefficients (relative to the storm cell center) were found to be **A** = $[-0.3809, 0.9895, -0.0049, 0.0039, 0.0010, 0.0032]^T$ and the β-coefficients were found to be **B** = $[-0.2676\ -0.0097, 0.9704, -0.0012, -0.0006, -0.0000]^T$, indicating a shift in the PR image (relative to SPOL) in the along and cross track directions, possibly some rotation (or slight scaling), and very little other distortion effects. The relative shift in the vertical direction was also determined at each of these altitudes and the average was found to be 0.0212 km. A 4 km CAPPI image of SPOL and PR measurements, aligned and matched in resolution volume, are shown in Figure 3.9(a) and Figure 3.9(b), respectively. Two PR beams (A and B) that pass through the cell are indicated by circles, which are shown in Figure 3.9(a) drawn to scale. A plot of PR and SPOL point-pairs at 4 km is shown in Figure 3.10 with "circles" denoting the SPOL edge points, "squares" denoting PR edge points before alignment and "x's" denoting PR edges after alignment. Note that after alignment, PR edges are more closely aligned to GR edges. The statistics before and after alignment of the spatial location between the edge points of the two radars, in terms of the bias and root-mean-squared error (RMSE) are computed for the x and y-coordinates separately. These statistics, for M points, are defined as

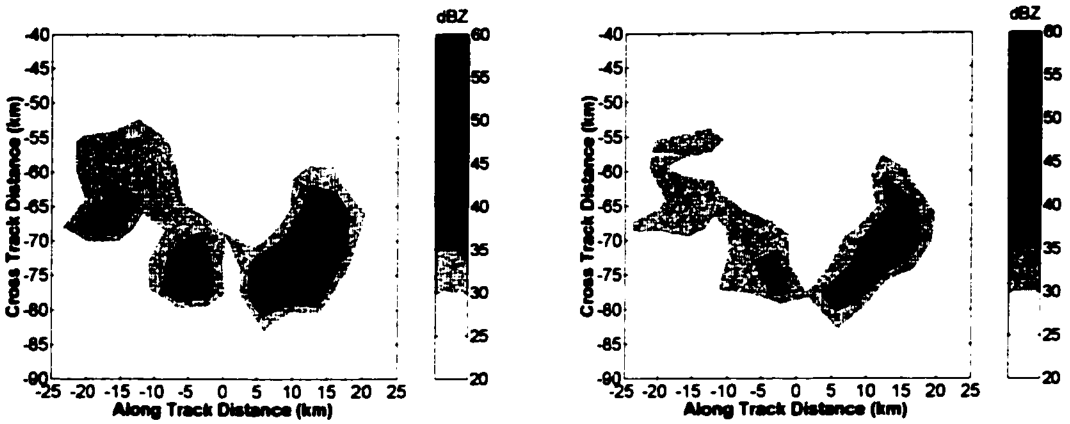

3.9(a) 3.9(b)

Figure 3.9: Matched resolution volume, and aligned, reflectivity data at 4 km CAPPI for TEFLUN-B data on August 13, 1998. (a) GR reflectivity with PR beams A and B at locations indicated by the circles drawn to scale. (b) PR reflectivity. Note the attenuation effects on PR measurements.

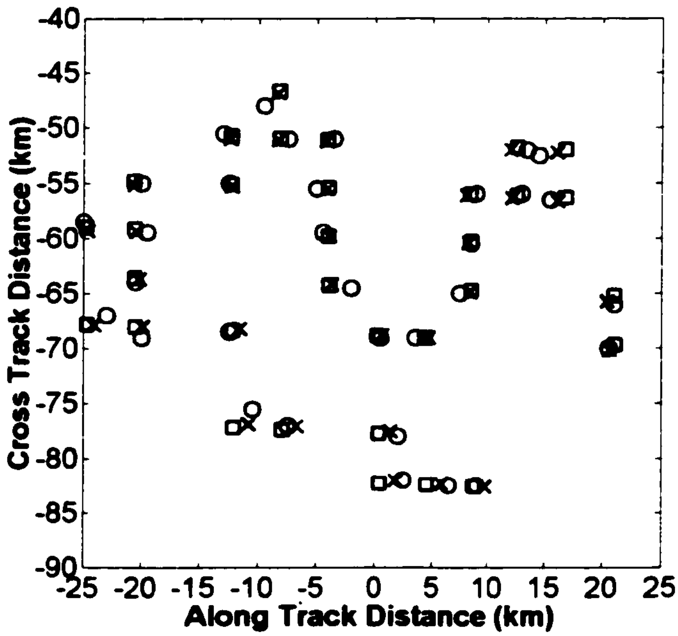

Figure 3.10: PR and SPOL contour edge point-pairs at 4 km CAPPI after resolution volume matching. The "circles" denote SPOL contour points, "squares" denote PR contour points before alignment (i.e., minimization of geometric distortion) and "x's" denote PR contour points after alignment. Note that the "x's" are closer to the SPOL edges than the "squares".

$$\text{bias}_{\text{xcoord}} = \frac{1}{M}\sum_{k=1}^{M}\left[x(GR)_k - x(PR)_k\right] \tag{3.28}$$

$$\text{RMSE}_{\text{xcoord}} = \left\{\frac{1}{M}\sum_{k=1}^{M}\left[x(GR)_k - x(PR)_k\right]^2\right\}^{1/2} \tag{3.29}$$

for the x-coordinates, where x(GR) and x(PR) are the set of x-coordinates locations for the GR and PR, respectively. Similar expressions are also used for the set of y-coordinate points. The Euclidean norm is taken of the statistics found for the x and y-coordinates from which the final statistics are derived.

A comparison of the final statistics before and after PR mapping shows improvement in the alignment between GR and PR data sets (i.e., minimization of the geometric distortion in PR observations relative to SPOL): the bias is seen to decrease from 0.2360 to 0.0509 while the RMSE decreases from 1.1911 to 0.9585. Additionally, the area of PR reflectivity equal to, or above, 20 dBZ is seen to be about 2.2% larger than the area of GR reflectivity, for the same contour, before alignment and about 2.0% after. Note that the percentage before alignment is approximately the same as the model developed using CHILL radar to simulate PR warping.

While the above analysis validates the alignment procedure in a spatial sense, the primary objective is the alignment of *measurements* so that meaningful and accurate validation of spaceborne meteorological algorithms can be conducted. Attenuation affects on PR return echoes, and the difference in receiver noise floor limits of GR and PR, make it difficult to statistically quantify the alignment procedure for all reflectivity levels. Nonetheless, it can be seen from the reflectivity scattergrams between SPOL and PR measurements shown in Figure 3.11(a), (b) and (c), that there is good improvement when resolution volume matching and distortion effects are considered. Figure 3.11(a) shows the scattergram of reflectivity between GR (i.e., SPOL) and PR without volume matching or distortion correction, while Figure 3.11(b) shows the scattergram when only volume matching is considered, but not the effects of PR geometric distortion. Figure 3.11(c) shows the scattergram after the GR and PR data sets have been matched in

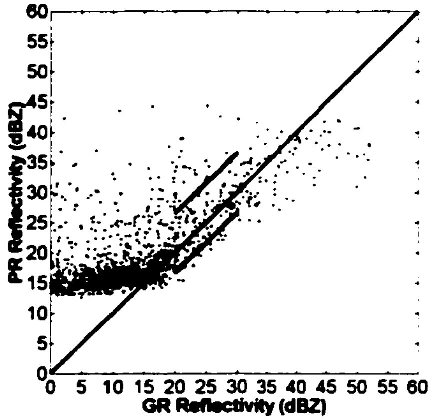

3.11(a)

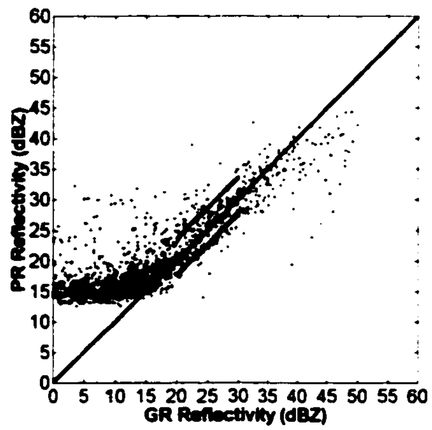

3.11(b)

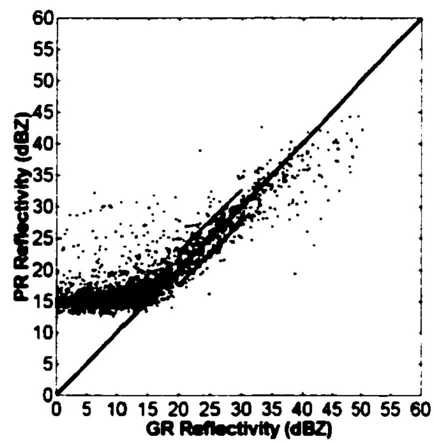

3.11(c)

Figure 3.11: Scattergrams of GR and PR reflectivity data. (a) without volume matching or geometric correction, (b) volume matching, but without geometric correction, and (c) when both GR and PR are matched in resolution volume and PR geometric distortion is considered.

resolution and the affects of geometric distortion on PR have been minimized. For reflectivities between 20 and 30 dBZ, which is in a range above the PR noise floor and where the effects of PR attenuation are assumed insignificant (and, also for reflectivity values above 2 km in altitude to reduce the effects of surface clutter return in PR measurements), it can be seen that the normalized standard error (NSE) between GR and PR reflectivity measurements decreases as volume matching and distortion effects are considered. The NSE is defined, for N number of data points, as

$$NSE = \frac{\sqrt{\frac{1}{N}\sum_{n=1}^{N}\left[Z_m(GR)_n - Z_m(PR)_n - b\right]^2}}{\overline{Z}_m(GR)} \tag{3.30}$$

where, $b = \overline{Z}_m(GR) - \overline{Z}_m(PR)$ with $Z_m(GR)$ being the measured GR reflectivity, $\overline{Z}_m(GR)$ the average GR reflectivity, $Z_m(PR)$ the measured PR reflectivity and $\overline{Z}_m(PR)$ the average PR reflectivity. The NSE is computed to be 20.36%, 12.09% and 10.35% for the cases: (a) without volume matching or geometric correction, (b) volume matching, but without geometric correction, and (c) when both GR and PR are matched in resolution volume and PR geometric distortion is considered, corresponding to the scattergrams in Figure 3.11(a), (b) and (c), respectively. Furthermore, the correlation coefficient between GR and PR reflectivity measurements, which can be defined by

$$coef = \frac{\frac{1}{N}\sum_{n=1}^{N}\left[Z_m(GR)_n - \overline{Z}_m(GR)_n\right]\left[Z_m(PR)_n - \overline{Z}_m(PR)_n\right]}{\sigma[Z_m(GR)]\sigma[Z_m(PR)]} \tag{3.31}$$

where σ is the standard deviation Figure 3.11 of the quantity, and is found to increase from 0.3778 to 0.5728 and to 0.6801 for each of the cases (a), (b) and (c), respectively.

The standard deviation of reflectivity between the two radars for each case are indicated by the solid lines in the 20-30 dBZ GR reflectivity interval in (a), (b) and (c). The average difference between GR and PR (i.e., GR-PR) in this interval is found to be -1.57 dB with standard deviation of 4.95 dB when volume matching and geometric correction are not performed. After volume matching, the average difference and standard deviation were found to be –0.61 dB and 3.00 dB, respectively. These values become -0.14 dB and 2.57 dB when geometric distortion correction is also applied after resolution volume matching has been performed. If measurement uncertainty in GR and PR instruments is assumed to be 1 dB, then the expected standard deviation in the scatter plots about their average difference should be no more than 2 dB. The amount of variability beyond this could be due to time synchronization mismatch between data sets, attenuation effects on PR return signal (even in the 20-30 dBZ interval), or residual errors in alignment and resolution volume matching. In the last case, it is seen that when resolution volume matching is performed the standard deviation is significantly reduced (nearly 2 dB). Likewise, after geometric distortion correction is applied the standard deviation about the average difference is further reduced.

A plot of log-averaged reflectivities across a horizontal plane as a function of altitude is shown for the August 13 data set in Figure 3.12. Both the PR warped and corrected reflectivities are shown (warped indicated by the dotted line and corrected by the dashed line) along with log-averaged GR reflectivity, shown as a solid line) (where Z_m(GR) is used to denote ground radar measured reflectivity and Z_m(PR) TRMM PR reflectivity). The plot indicates the presence of geometric warping in the TEFLUN-B data similar to the results of the simulation of PR data presented earlier. At lower altitudes, where there are non-uniform regions of reflectivity, warping is seen to increase the PR reflectivity observations by as much as 1.0 dB. At higher altitude where attenuation is low, the bias between GR and PR is about -1.5 dB.

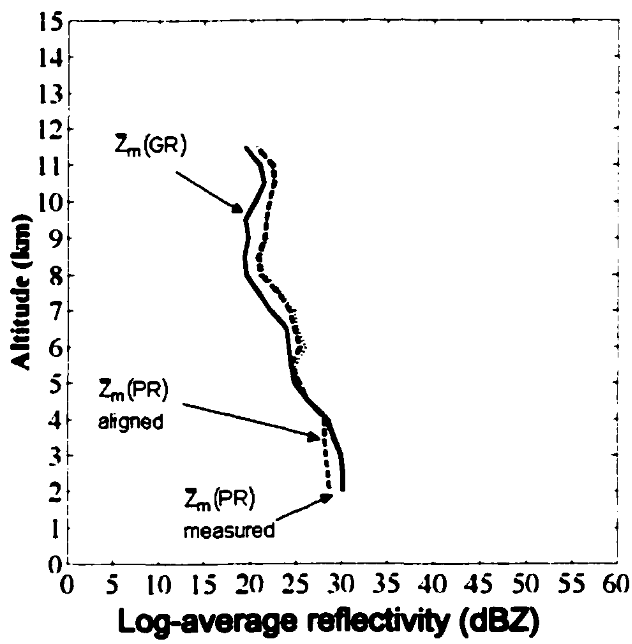

Figure 3.12: Plot of average reflectivity vs. altitude for both log-averaged reflectivity for TEFLUN-B data on August 13, 1998. The dashed line indicates true PR reflectivity, dotted line is the warped PR reflectivity and the solid line is the ground radar reflectivity. The difference between PR warped and corrected reflectivity can be as large as 1.0 dB, which agrees well with simulation.

After resolution volume matching and geometric distortion correction, direct point-to-point comparisons between GR and PR can be made. A cross section of the reflectivity profile for GR data is shown in Figure 3.13(a) with PR beams A and B indicated by the solid lines drawn to scale. The plot of PR and GR reflectivities along beam A is shown in Figure 3.13(b), and along beam B in Figure 3.13(c). In both along-beam plots, the bias between GR and PR is, again, within expected values. In fact, in both plots, the vertical profile of GR and PR agree well above the freezing level (which is indicated by the solid line taken from PR 2A23 data).

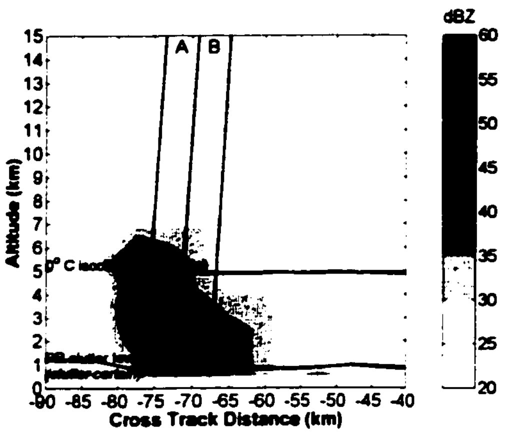

3.13(a)

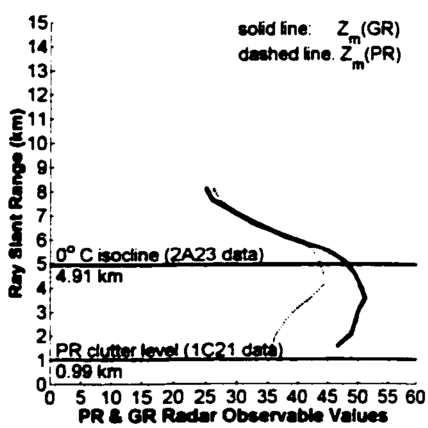

3.13(a)

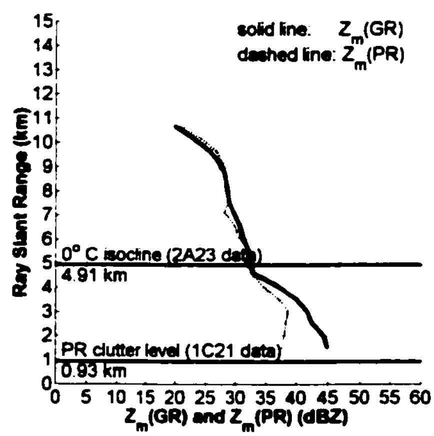

3.13(c)

Figure 3.13: TEFLUN-B data on August 13, 1998: (a) Vertical cross section of GR reflectivity image (volume matched and aligned) with PR beams A and B shown by solid lines drawn to scale. (b) Plot of PR and GR reflectivity vs. ray slant range for beam A. (c) Plot of PR and GR reflectivity vs. ray slant range for beam B.

Finally, a case is presented in which the difference between GR and PR reflectivity measurements is significant (on the order of a few dB). Data was collected simultaneously from the Kwajalein S-band radar and PR on July 10, 2000. PR data sampled at 4 km horizontal resolution at 2 km CAPPI along the TRMM ground track is shown in Figure 3.14. Two storm cells were selected for analysis from the data set, labeled A and B, and marked by the squares as shown in Figure 3.14 along with the location of the Kwajalein ground radar (denoted as GR in the figure).

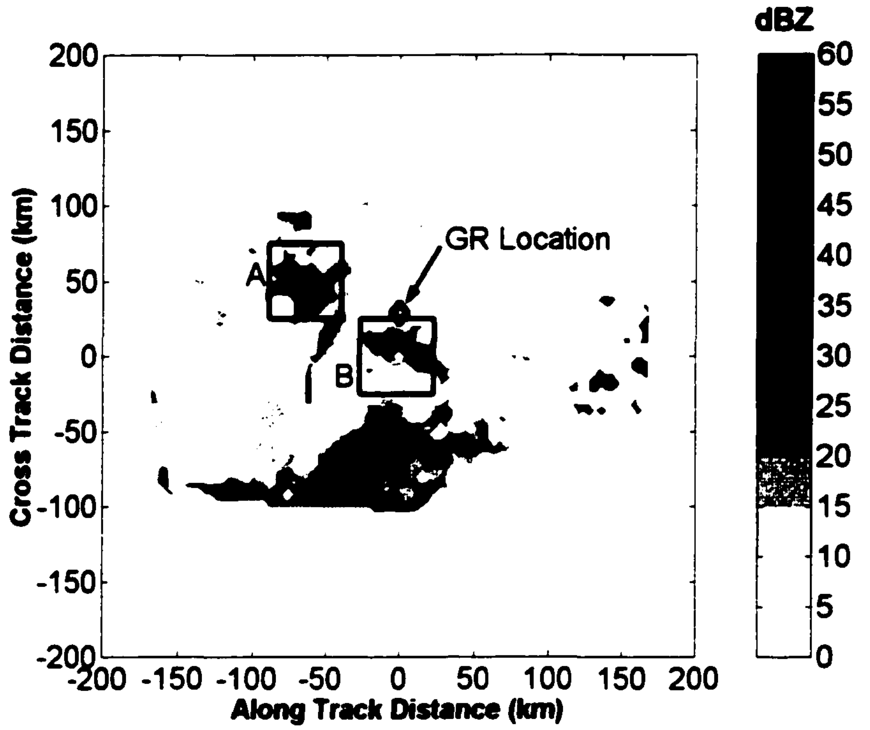

Figure 3.14: Kwajalein PR reflectivity data on July 10, 2000 at 2 km CAPPI, re-sampled to 4 km horizontal resolution along TRMM ground track. Shown are storm cell regions A and B and location of Kwajalein ground radar (GR) location.

Resolution volume matching and alignment was performed for each of the regions. A cross-section of PR reflectivity through the most intense part of storm cell A is shown in Figure 3.15(a), and a plot of the log-averaged reflectivity across a horizontal plane versus altitude for GR (solid line) and PR reflectivity after correction (dashed line) was constructed, which is shown in Figure 3.15(b). The average difference between GR reflectivity and PR reflectivity after correction is about –2.75 dB between the 6.5 and 9.5 km altitude levels (which is above the isocline level and roughly below the cloud top).

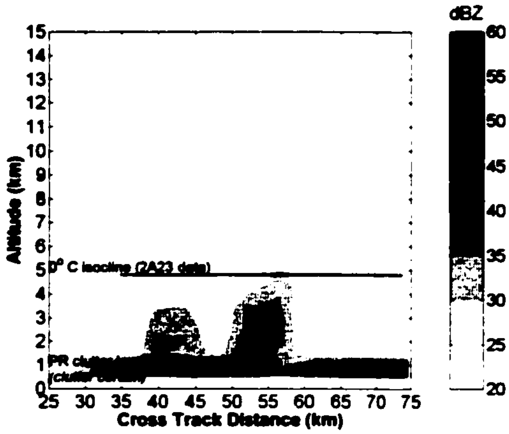

3.15(a)

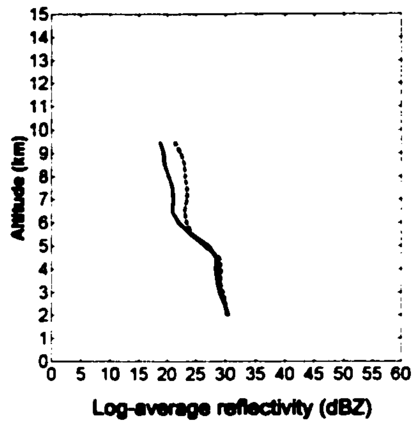

3.15(b)

Figure 3.15: Kwajalein data region A: (a) Shown is the PR cross section reflectivity image through most intense part of the storm cell. PR clutter level (certain) from 1C21 data set is shown by a solid line, and the 0° C isocline from 2A23 data set is also shown as a solid line. (b) Shown is the log-averaged reflectivity across each horizontal plane vs. altitude for GR reflectivity and PR reflectivity after alignment. The GR reflectivity is shown as a solid line with PR as a dotted line. The difference between GR and PR after alignment, between 6.5 and 9.5 km altitude, is –2.75 dB.

Similarly, the cross-section of PR reflectivity through the most intense part of storm cell B is shown in Figure 3.16(a). The log-averaged plots of GR reflectivity and PR reflectivity after correction is shown in Figure 3.16(b). The average difference between GR and PR is about -2.25 dB in the altitude levels between 6.5 and 9.0 km. Even though these storm cells are at different distances from the ground radar location (80 km for cell A and 28 km for cell B), and at different distances from the TRMM ground track (50 km for cell A and nearly coincident with the TRMM ground track for cell B) the difference between GR reflectivity and PR aligned reflectivity is nearly the same for both cases (within 0.5 dB). This simple comparison indicates the robustness of the method even when there exists significant differences between GR and SR measurements as well as when measurements are made at different distances from the radars.

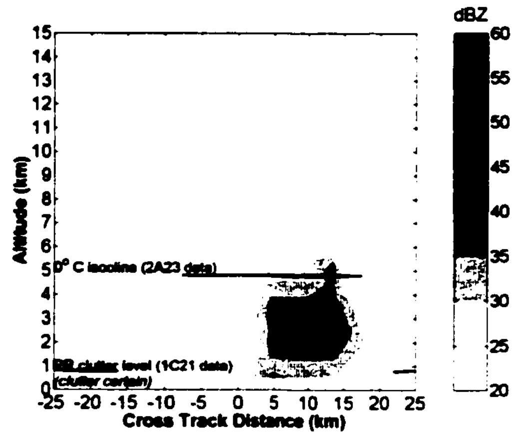

3.16 (a)

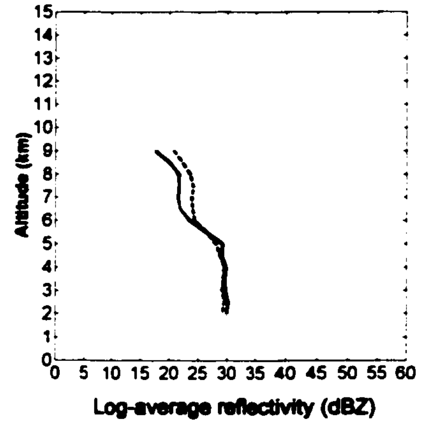

3.16 (b)

Figure 3.16: Kwajalein data region B: (a) Shown is the PR cross section reflectivity image through most intense part of the storm cell. PR clutter level (certain) from 1C21 data set is shown by a solid line, and the 0° C isocline from 2A23 data set is also shown as a solid line. (b) Shown is the log-averaged reflectivity across each horizontal plane vs. altitude for GR reflectivity and PR reflectivity after alignment. The GR reflectivity is shown as a solid line with PR as a dotted line. The difference between GR and PR after alignment, between 6.5 and 9.0 km altitude, is –2.25 dB.

3.5 Summary

A method to align radar measurements from two different platforms (i.e., a static terrestrial and a moving space-based platform) has been developed based on variable resolution volume matching and a polynomial fit to low-intensity contour images between the two radars. Though this method was developed for matching data between a spaceborne radar system and a ground-based system, the method could also be applied to any two radars: ground-ground, space-space, airborne-ground, space-airborne, etc., as well. The method takes into account geometric distortion induced on radar measurements if there is relative movement between the two platforms. An example using real data was used to demonstrate the matching procedure between a spaceborne radar and ground-based radar. Simulation was performed on CSU CHILL radar reflectivities to model PR return. It was found that under certain circumstances geometric warping can cause nearly a 1 dB offset from the true reflectivity field. This effect was also seen in data at altitudes where reflectivity was non-homogeneous. Finally, plots of GR and PR reflectivity along the PR were shown as an example of the type of direct comparison that can be made between space and ground radar measurements based on this technique.

Chapter 4

QUANTITATIVE ESTIMATION OF TRMM PR ATTENUATION

4.1 Theoretical Comparison of Reflectivities at S and K_u-Band

The PR is a downward pointing space-based radar that scans in the cross-track direction along a $\pm$17 degree arc. Situated onboard the TRMM satellite in orbit at a nominal altitude of 350 km, it can be modeled as essentially a vertically pointing instrument (Bolen and Chandrasekar, 2000). In contrast, the GR is a terrestrial-based radar that points only a few degrees off horizontal, and can thus be modeled as a horizontally pointing instrument. The viewing geometry of the two radars is depicted as per Figure 3.4, which is described in Chapter 3. Theoretical modeling is developed to obtain the differences between reflectivities at S- and K_u-band frequencies for rain under ideal (non-attenuating) conditions, which is later used as a reference for PR attenuation estimation. A three-parameter gamma distribution is used to model the rain field, and is described by (Ulbrich, 1983; Chandrasekar and Bringi, 1987):

$$N(D) = n_c f(D) \qquad \text{mm}^{-1}\,\text{m}^{-3} \qquad (4.1)$$

where N(D) is the number of particles (with diameter D in mm) per unit volume per unit size interval, n_c is the particle concentration, and $f(D)$ is the gamma probability density function (pdf), given by

$$f(D) = \frac{\Lambda^{\mu+1}}{\Gamma(\mu+1)} e^{-\Lambda D} D^{\mu}, \qquad (4.2)$$

where Λ and μ are parameters of the pdf, and Γ indicates the gamma function (Abrmovitz and Stegun, 1970). This can subsequently be written in normalized form as (Testude, et. al., 2001, Willis, 1984)

$$N(D) = N_W\, f(\mu) \left(\frac{D}{D_0} \right)^{\mu} \exp\left[-(3.67+\mu)\frac{D}{D_0} \right] \qquad (4.3)$$

where D_o is the volume-weighted median drop diameter and N_w is related to the intercept parameter N_o of an equivalent exponential RSD which has the same water content and D_o as the gamma RSD. The relationship between N_w and N_o can be expressed by:

$$N_W = N_0 f(\mu) D_0^{-\mu} \qquad (4.4)$$

with $f(\mu) = \frac{6}{(3.67)^4} \frac{(3.67+\mu)^{\mu+4}}{\Gamma(\mu+4)}$. Additionally, drops are assumed to be equatorially symmetric with orientation canting angles with a zero-mean Gaussian distribution having a standard deviation of 10 degrees. The azimuth angle was taken to be uniform over 360 degrees. For rain, Figure 4.1 shows a plot of K_u-Band reflectivities for different PR

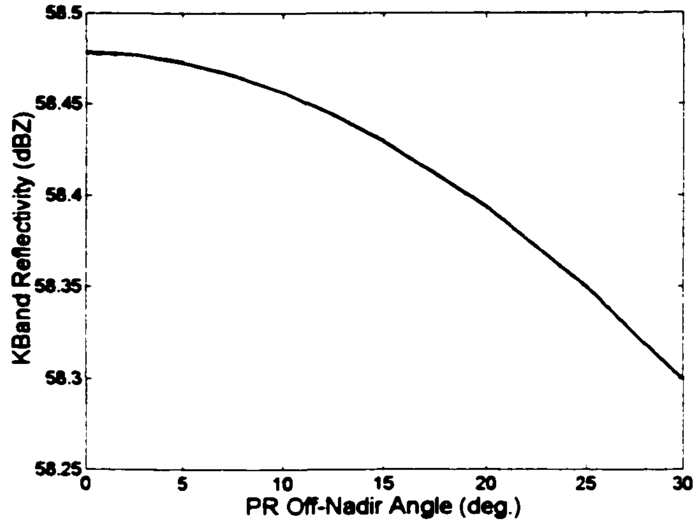

Figure 4.1: Theoretical model of space radar reflectivity measurements of rain for off-nadir pointing angles ranging from 0 to 30 degrees.

pointing angles ranging from 0 degrees off vertical (nadir) to 30 degrees off vertical. Parameters of the gamma distribution were set to N_o = 8000, D_o = 2.5 mm and μ = 0. From this figure, it can be seen that at the PR scan edges (i.e., at 17 degrees off-nadir) the difference in K_u-band reflectivity is only about 0.05 dBZ different from those at nadir. Hence, for all practical purposes, the PR can be assumed as a vertically pointing instrument in subsequent analyses. Using this geometry (i.e., horizontal pointing S-band ground radar, and vertical pointing K_u-band space radar), parameters of the gamma RSD model were varied within the following bounds (Dou, et. al., 1999):

$$\begin{aligned} &10^3 < N_W < 10^5 \\ &0.5 < D_0 < 2.5 \text{ mm} \\ &-1 < \mu < 4 \end{aligned} \tag{4.5}$$

(and, within the constraint that rain rate be less than 300 mm h^{-1}) to determine the theoretical relationship between S- and K_u-band reflectivity measurements for rain medium. A scattergram of the theoretical difference between these frequencies, as a function of GR S-band measurements, is shown in Figure 4.2(a). The mean relationship, and 1-σ bounds, for the scatter points were determined at 1 dB increments of S-band reflectivity along the horizontal axis, and are plotted in Figure 4.2(b) with the mean relationship shown as a dashed line and the 1-σ bounds shown as dotted lines. A second-order polynomial fit was made to the mean relationship and is also shown in figure as a solid line. The polynomial that fits the mean difference relationship (in the interval 20-55 dBZ) is of the form: $\varepsilon[Z(GR)] = 0.0028\ Z(GR)^2 - 0.1188\ Z(GR)+1.0468$, where ε is the difference in reflectivity values and $\overline{Z}(GR)$ is the mean theoretical ground radar reflectivity. It can be seen from the scatter plot, that as drop size increases, K_u-band reflectivities start to deviate from S-band reflectivities due to Mie scattering, and can be up to 2.5 dBZ larger in value.

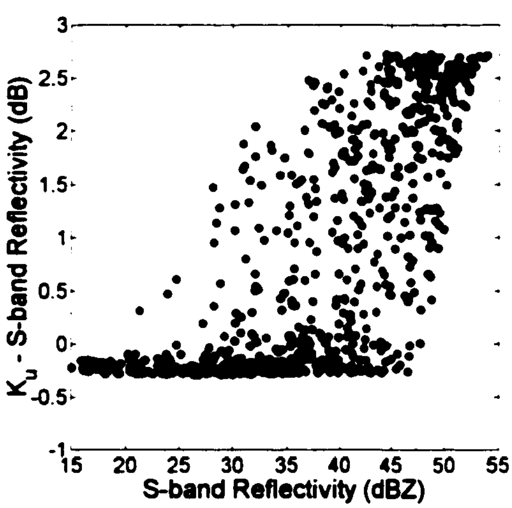

4.2 (a)

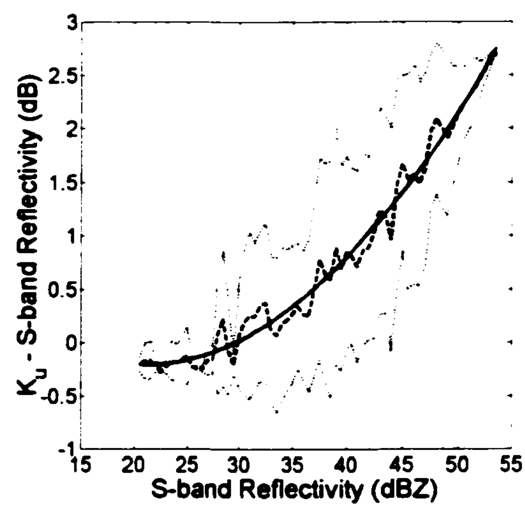

4.2 (b)

Figure 4.2: Theoretical model of the difference in reflectivity for ground-based S-band radar nearly horizontally pointing and K_u-band space radar nearly vertically pointing. (a) Scattergram of S-band reflectivity vs. the difference in reflectivities. (b) Statistical analysis of scattergram in panel (a): mean relationship for scattergram points shown by dashed line, second-order polynomial fit to the mean relationship shown as a solid line, and 1-σ deviation bounds on mean relationship shown as dotted lines.

4.2 Quantitative Inter-Comparison of GR and PR Reflectivity Observations.

Simultaneous observations were collected from ground radar and the TRMM PR when meteorological echoes were present. Data from four case studies was obtained: two days (August 13 and 15, 1998) during the TEFLUN-B campaign and two separate storm cells on one day during the TRMM-LBA experiment (labeled as storm cells February 25A and 25B, 1999). In each case, the GR was scanning in a planned position indicator (PPI) mode set to sweep sectors in azimuth extent covering only the storm areas of interest. The full vertical extents (i.e., starting from near ground level to 15 km altitude) of each of the storm cells were surveyed. A description of the ground radar operational characteristics, and TRMM overflight characteristics, for each case study are given in Appendix B. Also given in Appendix B is a wide area view of the PR reflectivity measurements sampled at 4 km horizontal resolution, and taken at 2 km CAPPI, for the case studies. These wide area reflectivity maps show the storm cells being studied.

The geometric mean (i.e., log-averaged value) of GR measured reflectivity, Z_m(GR), PR measured reflectivity, Z_m(PR), and PR attenuation corrected reflectivity, Z_c(PR), was determined across horizontal planes at 0.5 km altitude increments for altitudes ranging from 1.5 km to the storm top for each of the case studies. Plots of the mean vertical profiles are shown in Figures 4.3, 4.4, 4.5 and 4.6. Vertical cross-sections of the reflectivity measurements (through the most intense part of the storm cell) are also shown for each of the case studies in these figures as well. Ground radar cross-sections are shown in the (a) panels, and PR reflectivity in the (b) panels along with the freezing height altitude and PR clutter level (certain), shown as solid lines. Plots of the mean vertical reflectivity profiles for PR measured, $\overline{Z}_m(PR)$, and PR attenuation corrected, $\overline{Z}_c(PR)$, observations are shown in the (c) panels. Also shown in the (c) panels are the mean ground radar measurements adjusted for K_u-band frequency, $\overline{Z}_{eq}(GR)$, at each altitude increment. Calculations for $\overline{Z}_{eq}(GR)$ are based on theoretical results and measured mean GR reflectivity, $\overline{Z}_m(GR)$:

$$\overline{Z}_{eq}(GR) = \overline{Z}_m(GR) + \epsilon\left[\overline{Z}(GR)\right] \tag{4.6}$$

where, $\varepsilon[Z(GR)]$ is the relationship given by the solid line in Figure 4.2(b). Several observations can be made from Figures 4.3, 4.4, 4.5 and 4.6. Firstly, in the absence of significant attenuation (i.e., at altitudes above the rain layer), the mean reflectivities measured by the ground radar and TRMM PR agree to within about 2 dB. More specifically, the bias ($Z_{eq}(GR) - Z_m(PR)$) is –1.54 dB, -1.68 dB, -1.46 dB and –1.50 dB for the TEFLUN-B August 13 and 15, 1998, and TRMM-LBA February 25A and 25B, 1999 data sets, respectively. This is consistent with observations made by Anagnostou, et. al. (2001) of the bias between TRMM PR and SPOL measurements who used a different methodology for comparison. This is a very important result indicating the cross-validation of the calibration between TRMM PR and GR. If there is no calibration difference between the two radars, and if all the effects of different resolution volumes, look angle, and frequency difference are accounted for, then the difference between $\overline{Z}_m(PR)$ and $\overline{Z}_{eq}(GR)$ gives a direct measure of the PIA, which in turn can be used for various applications including validation of attenuation correction algorithms.

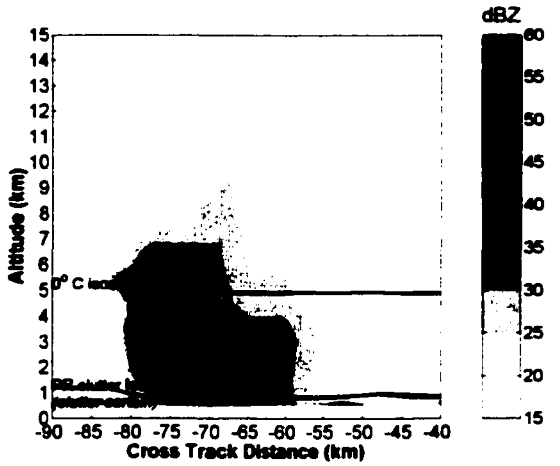

4.3(a)

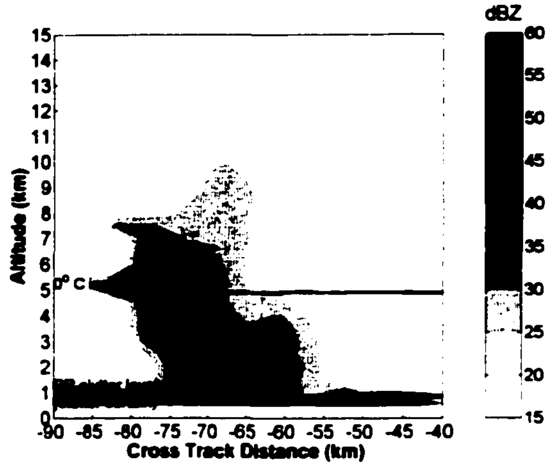

4.3(b)

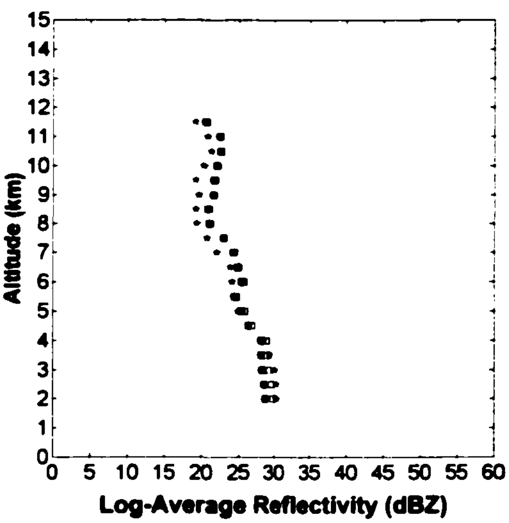

4.3(c)

Figure 4.3: TEFLUN-B, August 13, 1998. (a) Vertical cross-section of GR reflectivity measurements through most intense part of the storm cell. (b) Vertical cross-section of PR reflectivity measurements through the same location as in panel (a). (c) Plot of log-averaged reflectivity across horizontal planes at incremental altitudes for: ground radar corrected for K_u-band, $\overline{Z}_{eq}(\mathrm{GR})$ (shown as a stars), PR measured, $\overline{Z}_m(\mathrm{PR})$ (shown as a black squares), and PR attenuation corrected, $\overline{Z}_c(\mathrm{PR})$ (shown as white squares).

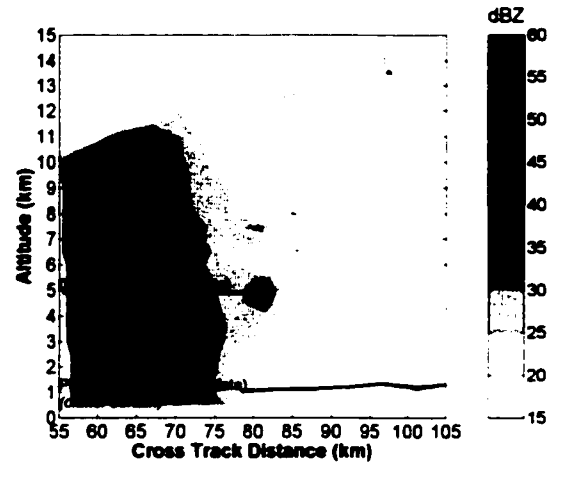

4.4(a)

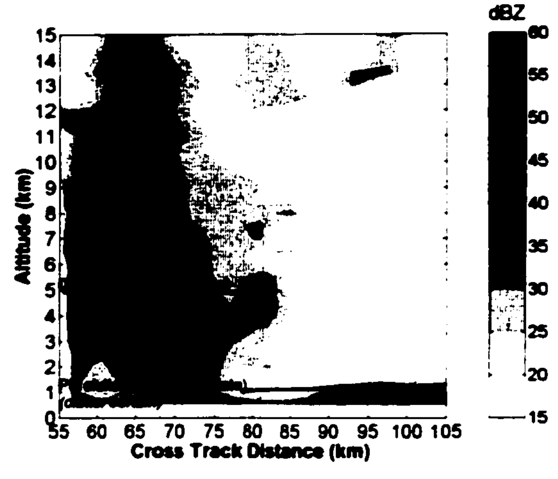

4.4 (b)

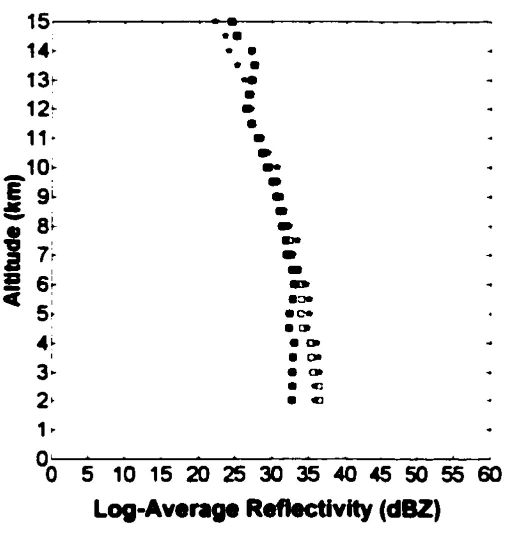

4.4(c)

Figure 4.4: TEFLUN-B, August 15, 1998. (a) Vertical cross-section of GR reflectivity measurements through most intense part of the storm cell. (b) Vertical cross-section of PR reflectivity measurements through the same location as in panel (a). (c) Plot of log-averaged reflectivity across horizontal planes at incremental altitudes for: ground radar corrected for K_u-band, $\bar{Z}_{eq}(\text{GR})$ (shown as a stars), PR measured, $\bar{Z}_m(\text{PR})$ (shown as a black squares), and PR attenuation corrected, $\bar{Z}_c(\text{PR})$ (shown as white squares).

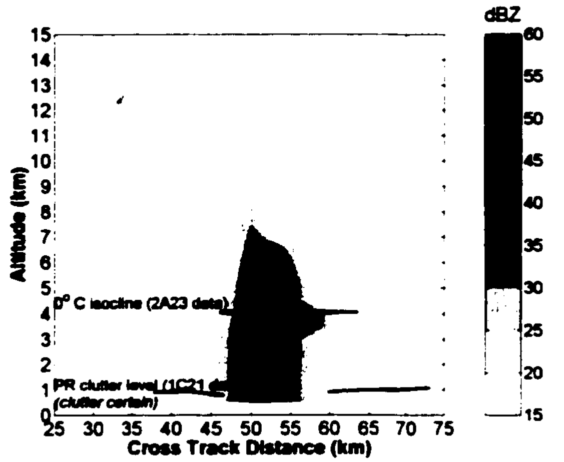

4.5(a)

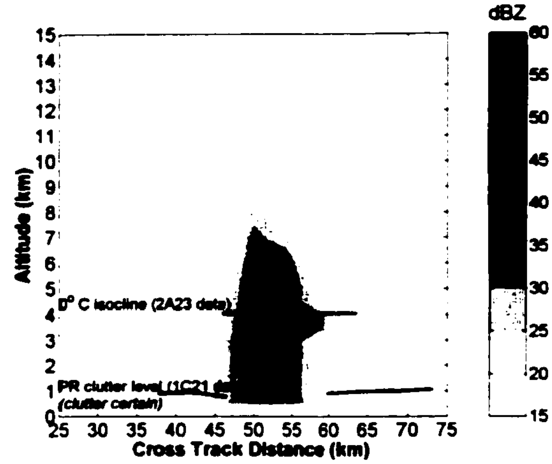

4.5(b)

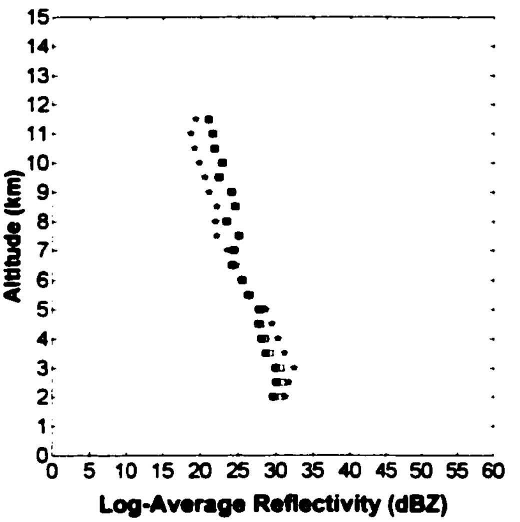

4.5(c)

Figure 4.5: TRMM-LBA, February 25A, 1999. (a) Vertical cross-section of GR reflectivity measurements through most intense part of the storm cell. (b) Vertical cross-section of PR reflectivity measurements through the same location as in panel (a). (c) Plot of log-averaged reflectivity across horizontal planes at incremental altitudes for: ground radar corrected for K_u-band, $\overline{Z}_{eq}(\text{GR})$ (shown as a stars), PR measured, $\overline{Z}_m(\text{PR})$ (shown as a black squares), and PR attenuation corrected, $\overline{Z}_c(\text{PR})$ (shown as white squares).

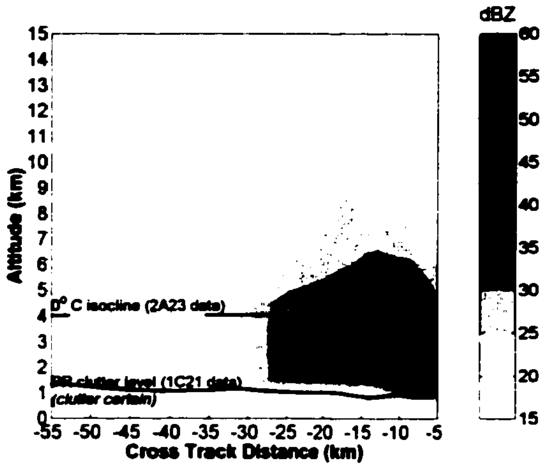

4.6(a)

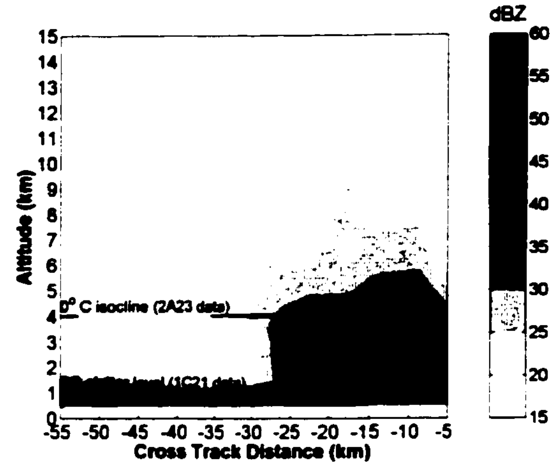

4.6(b)

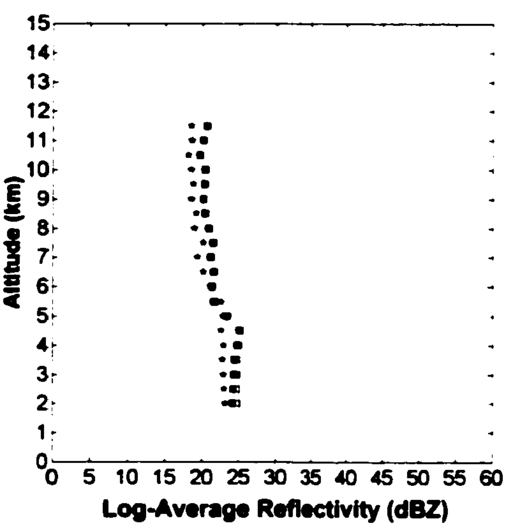

4.6(c)

Figure 4.6: TRMM-LBA, February 25B, 1999. (a) Vertical cross-section of GR reflectivity measurements through most intense part of the storm cell. (b) Vertical cross-section of PR reflectivity measurements through the same location as in panel (a). (c) Plot of log-averaged reflectivity across horizontal planes at incremental altitudes for: ground radar corrected for K_u-band, $\bar{Z}_{eq}(\mathrm{GR})$ (shown as a stars), PR measured, $\bar{Z}_m(\mathrm{PR})$ (shown as a black squares), and PR attenuation corrected, $\bar{Z}_c(\mathrm{PR})$ (shown as white squares).

The difference between ground radar observations and PR measurements corrected for attenuation, $Z_{eq}(GR)$-$Z_c(PR)$, at 2 km altitude, were found to be 0.62 dB, -2.11 dB, 0.40 dB and −1.33 dB for the August 13 and 15, 1998 and February 25A and 25B, 1999 cases, respectively. Correcting for the bias between the two radars, a direct evaluation of the total two-way PIA estimated from the PR attenuation correction algorithm can be made. Adjusting for the bias between the two radars, the differences between $Z_{eq}(GR)$ and $Z_c(PR)$ at 2 km altitude are: 2.16 dB, -0.43 dB, 1.86 dB and −0.17 dB for each of the cases, respectively.

4.3 Percentage of Undetected PR Echoes

In the absence of attenuation, the detection threshold of the PR is about 20 dBZ (which is the reflectivity level that is 3 dB above the receiver noise floor). A quantitative estimate of the percentage of PR data missed, in comparison to the GR data, is made, and its potential impact on mean rainfall estimates is determined. Simultaneous point-wise comparison is made between $Z_m(GR)$ and $Z_m(PR)$ for this purpose. Volume matching and alignment is performed (as per the procedure developed in Chapter 3). Subsequently, if, in the presence of GR echo, the signal power received by the PR is less than 3 dB SNR (signal-to-noise-ratio), it is classified as a *missing* echo. The percent of missing (or, undetected) PR echo is computed from the ratio of area of GR echo below the PR 3 dB receiver noise floor to the total storm cell area measured by the GR. For August 13, 1998 data this percentage is 57.8 %. For August 15, 1998 and the two LBA cases, February 25A and 25B, 1999, the percentage of undetected echo is 66.7%, 66.1% and 62.7%, respectively. Though the numbers are high, they may not have a significant impact on rainfall estimates. The percentage of missed PR echo and PR total areal rainfall rate under-estimate is summarized in Table 4.1.

Table 4.1: Summary of percentage of PR "missed" echo and rainfall rate under-estimation.

Case Study	% PR "Missing" Echo	% PR Total Areal Rainfall Under-Estimation
MELB980813	57.8	4.3
MELB980815	66.7	2.4
BRZL990225A	66.1	5.9
BRZL990225B	62.7	8.9

Shown in Figure 4.7 are the histograms of $\overline{Z}_m(GR)$ for undetected PR echo, at 2 km altitude, for each of the case studies: August 13 and 15, 1998, and February 25A and 25B, 1999 in panels (a), (b), (c) and (d), respectively. It is clear from the histograms that most of the missing PR echo is at low reflectivity value and does not significantly contribute to the estimate of rain rate. Nevertheless, the histograms have "long tails" on the high reflectivity side, which could be due to attenuated PR echoes falling below 20 dBZ. A small percentage of this could also be due to misalignment. In order to demonstrate that the majority of the high levels of GR reflectivity measurements missed by PR are due to attenuation, similar histograms were constructed at 10 km altitude. The results of the histogram are shown in Figure 4.8. at 10 km altitude, the effect of attenuation should be negligible and the missing echoes in these histogram are limited to about 20 dBZ. Thus, a combination of Figure 4.7 and 4.8 indicate that reflectivity values higher than 20 dBZ could be missed by the PR due to attenuation. To determine the impact of missing PR echoes on rainfall estimates, the total areal rainfall was computed from the ground radar data: i.e., whenever there was a missing PR echo the corresponding GR data was used in the rainfall estimate. The rainfall estimates were computed using the WSR-88D (National Weather Service Weather Surveillance Radars [WSR]), Z-R algorithm given by $R = 0.0017\, Z^{0.714}$. The results indicate a 4.3%, 2.4%, 5.9% and 8.9% under estimation of the total areal rainfall for the PR for each of the case studies corresponding to the histograms of Figure 4.7(a), (b) (c) and (d), respectively.

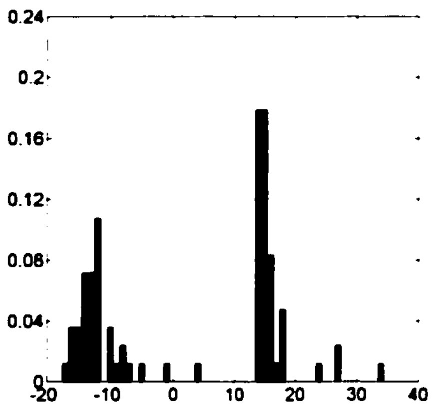

4.7(a)

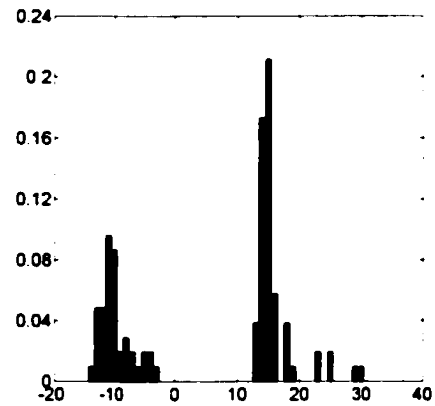

4.7(b)

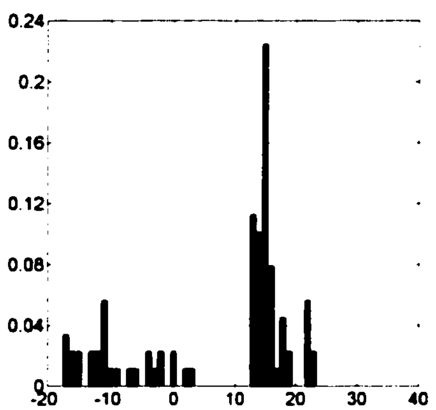

4.7(c)

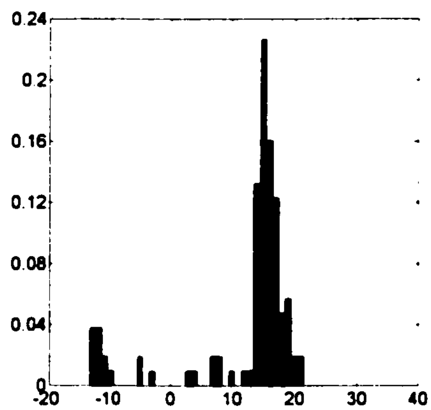

4.7(d)

Figure 4.7: Histograms of GR reflectivity corresponding to PR measurements that are 3 dB below the PR noise floor level at 2 km altitude. (a) August 13, 1998. (b) August 15, 1998. (c) February 25A, 1999. (d) February 25B, 1999.

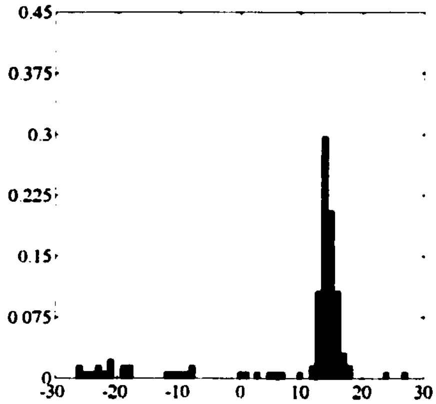

4.8(a)

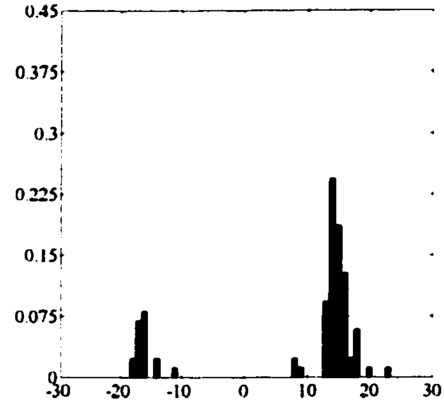

4.8(b)

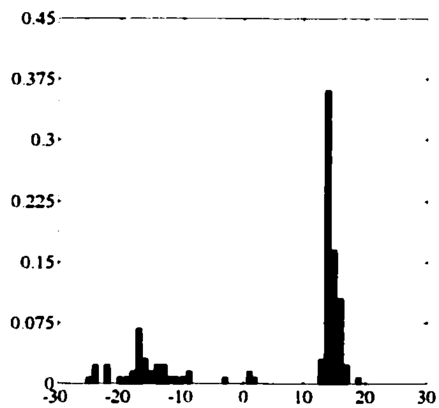

4.8(c)

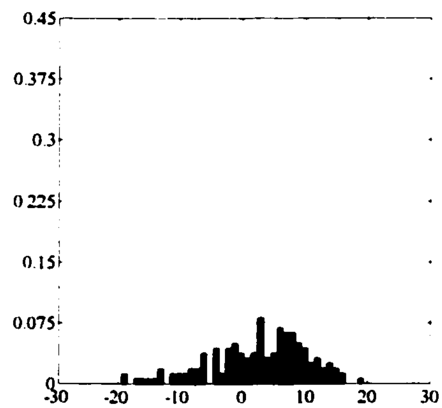

4.8(d)

Figure 4.8: Histograms of GR reflectivity corresponding to PR measurements that are 3 dB below the PR noise floor level at 10 km altitude. (a) August 13, 1998. (b) August 15, 1998. (c) February 25A, 1999. (d) February 25B, 1999.

4.4 Summary

Simultaneous comparisons of TRMM PR data and SPOL data were made to cross-validate TRMM PR and ground radar observations at S-Band. The two radars operate with different beamwidths, at different look angles and at different frequencies. In addition, TRMM PR operates at an attenuating wavelength in the presence of wet precipitation. A procedure has been developed to evaluate the mean differences between TRMM PR and GR data accounting for the differences in the radar systems. There are three main conclusions that can be derived from the analysis: Firstly, in the absence of attenuation (i.e., at altitudes above the freezing level), the mean value of TRMM PR observations and ground radar observations agree to within 2 dBZ. The average bias between the two radars from the case studies analyzed is –1.55 dB. This is within the measurement uncertainty of the two radars, thus cross-validating the calibration of the two instruments. The average difference between Z_{eq}(GR) and Z_c(PR) was found to be 0.85 dB, which is within the uncertainty measurements of the two radars. Secondly, the log-averaged PR attenuation corrected reflectivity estimates, $\overline{Z}_m(PR)$, agree fairly well at low altitudes with ground radar observations, thereby validating the estimate of PIA. This comparison also yielded a direct measure of the average attenuation per data set, and was found to be nearly 5 dB, adjusted for bias (across log-averaged data), for the cases analyzed. Lastly, the TRMM PR misses part of the storm due to a high detection threshold, as compared to high-sensitivity ground radars. Though the percentage of missed PR echoes was about 63.3%, on average, most of the missed echoes were of low reflectivity, and, thus, the impact on rainfall estimate is not significant. A quantitative evaluation of bias in total areal rainfall estimate yielded an under estimation of PR measurements of about 5.4%, on average, which is negligible compared to the accuracy of the rainfall estimates.

Chapter 5

CROSS-VALIDATION OF PR CORRECTION ALGORITHM WITH GR POLARIMETRIC OBSERVATIONS

5.1 Overview of SR Beam-Path Measurements

Polarimetric ground radar observations can be used to quantify the two-way path-integrated attenuation, due to precipitation, that is experienced by earth-observing space radar (SR) systems operating at attenuating frequencies. Observations from ground-based polarimetric radars have been previously used to study the effects of a precipitating medium on radio wave propagation along earth-space paths using satellite-based beacon data. A few of these studies are described by Beaver and Bringi (1997) who also present a method for determining the relationship between specific attenuation (k) at K_a-band frequency and specific differential phase (K_{dp}) at S-band. In their study, they used ground-based observations from the Colorado State University CHILL S-band polarimetric radar to compare earth-space propagation data from the Advanced Communications Technology Satellite (ACTS) beacon.

In rain medium, the cumulative propagation phase shift between horizontally and vertically polarized waves will be different. Bringi, et. al. (1990), showed that attenuation through rain is nearly linearly proportional to the differential phase shift (ϕ_{dp}) at microwave frequencies and modeled the relationship between specific differential phase at S-band frequency and specific attenuation at S, C and X-band frequencies. In a similar way, attenuation for earth-space propagation can also be related to the specific differential phase shift, K_{dp}, measured along the earth-space path. Subsequently, relationships between the specific attenuation, *k*, with specific differential phase (for high rain rate) and reflectivity at horizontal polarization state, Z_h, (for low rain rate and various other hydrometeor types), can be used to determine the two-way PIA along the space radar beam

In this chapter, theoretical relationships are determined between ground-based polarimetric observations and expected values of *k* for various hydrometeor types present along the PR beam path. Hydrometeor classification is performed based on a fuzzy-logic technique developed by Liu and Chandrasekar (2000), which uses GR polarimetric observations. The specific attenuation is integrated along the PR beam path to determine the PIA at each point along the beam. Measured PR reflectivity along with the derived PIA are used to determine the *true* PR vertical reflectivity profile.

5.2 Theoretical Model of GR PIA Estimation

A theoretical model is used to determine the relationship between the specific attenuation (*k*) of a nearly vertical pointing K_u-band spaceborne radar system with the observations of specific differential phase (K_{dp}) and measurements of reflectivity (Z_h) from a nearly horizontal pointing ground radar system. Bolen and Chandrasekar (2000) have shown that modeling the pointing geometries of the two systems in this way is reasonable for intercomparison. The scattering properties for ten different hydrometeor types was determined which include: drizzle (dr), rain (rn), low-density ice crystals (li), high-density ice crystals (hi), wet ice (wi), dry graupel (dg), wet graupel (wg), small hail (hs), large hail (hl) and rain mixed with hail (rh). The hydrometeor size distribution (HSD) for each class type is assumed to be of the form (Ulbrich, 1983):

$$N(D) = n_c\, f(D) \qquad \text{mm}^{-1}\ \text{m}^{-3} \qquad (5.1)$$

where N(D) is the number of particles (with diameter D in mm) per unit volume per unit size interval, n_c is the concentration, and $f(D)$ is the gamma probability density function (pdf), given by

$$f(D) = \frac{\Lambda^{\mu+1}}{\Gamma(\mu+1)} e^{-\Lambda D} D^{\mu}; \quad \mu > -1 \qquad (5.2)$$

where Λ and μ are parameters of the gamma pdf, and Γ indicates the gamma function (Abramovitz and Stegun, 1970). This can subsequently be written in a normalized form as (Willis, 1984 and Testude et. al., 2000)

$$N(D) = N_W\, g(\mu) \left(\frac{D}{D_0} \right)^{\mu} \exp\left[-(3.67+\mu) \frac{D}{D_0} \right] \qquad (5.3)$$

where

$$g(\mu) = \frac{3.67}{3.67^4} \frac{(3.67+\mu)^4}{\Gamma(\mu+4)}, \qquad (5.4)$$

and D_o is the volume-weighted median drop diameter (in units of mm). In this formulation, N_w has units of $mm^{-1}\ m^{-3}$ and is more convenient for theoretical modeling (Bringi and Chandrasekar, 2001).

The HSD parameters (N_w, D_o and μ) were varied according to the values derived from the literature: drizzle as per Sauvegot (1992); rain as per Gorgucci, et. al., (2000a); low-density ice crystal and wet ice as per Passarelli (1978); high-density ice crystal as per Beheng (1978); graupel, wet and dry, as per Bringi, et. al. (1997); and hail as per Cheng and English (1983). The rain-hail mixture was determined from simultaneous inputs of both rain and hail hydrometeors to the simulation. For all but rain, μ was set equal to zero making the HSD an exponential distribution. Particles were also assumed to be rotationally and equatorially symmetric with orientation. The canting angle distribution for rain was fairly narrow, but for graupel and hail it was broad to model tumbling and random orientation. These are, again, consistent with the literature (Bringi and Chandrasekar, 2001).

Raindrops are assumed to be nonspherical in shape with HSD parameters in the range $0.5 \le D_0 \le 2.5$ (mm), $3 \le \log_{10}(N_W) \le 5$ ($mm^{-1}m^{-3}$) and $-1 \le \mu \le 4$. For raindrops of this form, (i.e., oblate spheroids) the axis ratio, r, where r is the ratio of the minor axis to major axis, can be approximately related to the equivalent drop diameter, D_e, of a spherical drop via several models.

At this point, it is noted that the mean canting angle shape and model does not severely affect the estimate of specific attenuation on PR measurements. However, shape and canting angle affect ground radar measurements of K_{dp}. Here, the canting angle mentioned is the "effective canting angle," where transverse oscillations of medium sized raindrops could appear as canting (Andsager, et. al., 1999). Andsager, et. al. (1999) suggest a modified raindrop shape relation in the 1 to 4 mm range to account for transverse oscillation. They also suggest use of a combination of Beard and Chuang (1987) and Andsager, et. al. (1999) to model raindrop shapes for the full range of sizes. However, care should be taken not to modify the mean shape and canting angle simultaneously to account for drop oscillations. The impact of drop shape and canting angle can be seen from the following equations for K_{dp} under Rayleigh approximation (Bringi and Chandresekar, 2001)

$$K_{dp} = \left(\frac{180}{\lambda}\right) 10^{-3} C\, W\left(1 - \bar{r}_m\right) \tag{5.5}$$

where C is a dimensionless constant $(\cong 3.75)$, W is water content, and $\bar{r}_m$ is the mean axis ratio. If the axis ratio relation is assumed linear with a slope of β, (i.e., $r = 1 - \beta D$), then K_{dp} is modified with canting angle distribution as

$$K_{dp} = \beta N_w F_3 \left(\mu, D_o\right) \exp\left(-2\sigma^2\right) \tag{5.6}$$

where σ^2 is the variance in the canting angle (Bringi and Chandrasekar, 2001) and F_3 is a function of μ and D_o. Thus, it can be seen that K_{dp} can be reduced by the variance of canting angle distribution, or by decreasing the mean axis ratio. The slope of the k-K_{dp} relationship for the Pruppacher and Beard (1970), Beard and Chuang (1987), and Andsager, et. al. (1999) axis ratio models are 1.96 dB deg^{-1} and 2.24 dB deg^{-1}, and 2.67

dB deg^{-1}, respectively. However, whatever is modeled, the resulting values of Z_h, Z_{dr} and K_{dp} should be consistent with observations (Keenan, et. al., 2000). Such care ensures consistency in the modeling. For light rain, on the order of 10-20 mm hr^{-1}, (i.e., for K_{dp} < 0.5 deg km^{-1}), a k-Z_h relationship is used. Subsequent analysis in this research uses the Beard and Chuang (1987) axis ratio model to compute the k-K_{dp} relationship for rain medium when $K_{dp} \geq 0.5$ deg km^{-1}.

Figure 5.1 depicts the differences in the viewing geometry between the two systems, and how GR measurements are made along the PR beam, which are used to determine the specific attenuation along the beam. The effect of the difference in

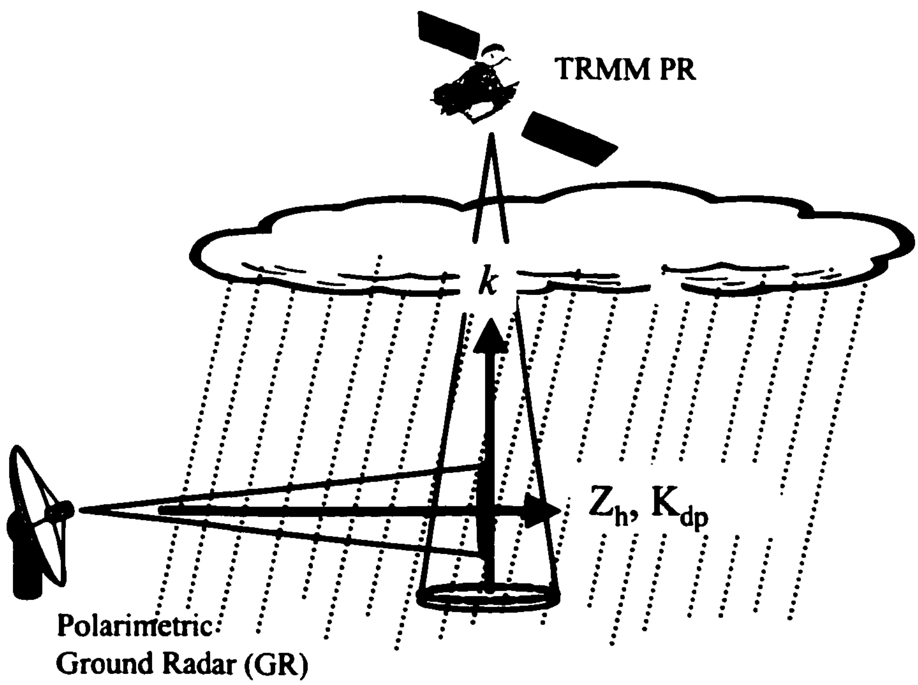

Figure 5.1: Illustration of the ground-based radar observations, reflectivity (Z_h) and specific differential phase (K_{dp}), taken along the TRMM PR beam to determine the specific attenuation (k), and the relative viewing geometry of each system.

operating frequencies between the two radars on reflectivity measurements is illustrated in Figure 5.2. In this figure, rain medium is modeled using a three-parameter gamma distribution with values as previously stated for rain. A theoretical scattergram is constructed of S-band differential reflectivity (Z_{dr}) (for rain rate in the range of about 1 to 300 mm hr^{-1}) versus the difference in reflectivity between a vertical-looking K_u-band system and horizontal pointing S-band system. As particle size gets larger Z_{dr} increases. Additionally, as particle size gets larger, K_u-band reflectivities start deviating more from S-band due to Mie scattering. Thus, the difference in reflectivities and Z_{dr} are well correlated, which can be seen in Figure 5.2. The difference in K_u-band and S-band reflectivity can be as much as 2.5 dB.

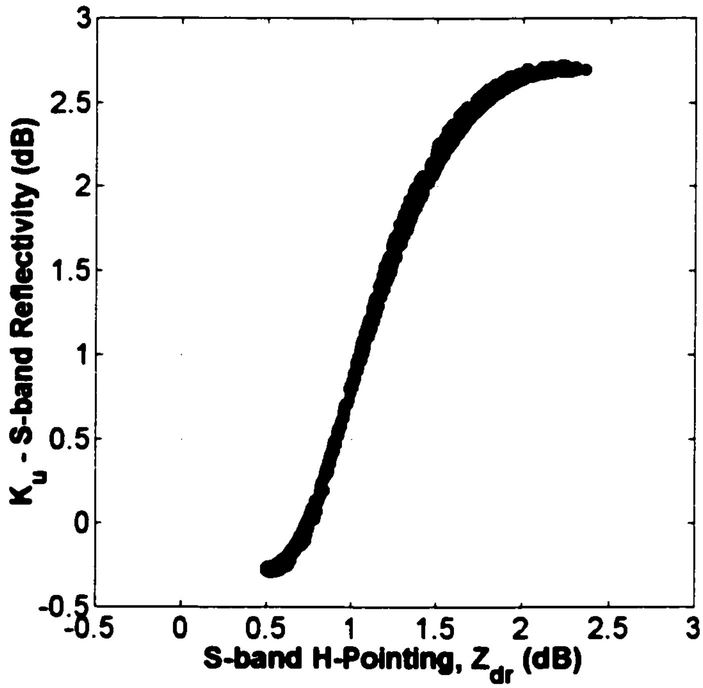

Figure 5.2: Theoretical modeling for rain of S-band differential reflectivity (Z_{dr}) from a horizontal pointing system versus the difference between Ku-band reflectivity from a system pointing in the vertical direction and S-band reflectivity from a horizontal pointing system.

Though rain is the predominant medium responsible for the attenuation in the observed path, drizzle, dry-ice particles and mixed-phase particles may also be present. These hydrometeors are included in the estimate for k via a k-Z_h relationship. The retrieval of k from K_{dp} is used only for rain when rain rate is relatively high. For hydrometeors such as drizzle, where the drop shape is assumed to be nearly spherical, K_{dp} cannot be measured. Similarly, K_{dp} is nearly zero for ice phase. Finally, dry ice particles at the frequencies measured have no measurable phase value or value of specific differential phase. Hence, for all hydrometeors expect for high rain rate rain, a k-Z_h relationship is used to determine the specific attenuation along the PR beam. Specifically, k-Z_h relationships were determined for drizzle, low-density ice crystals, wet ice, dry graupel, wet graupel, small hail, large hail, and rain-hail mixture. As previously stated, the various hydrometeors are modeled as per values derived from the literature: Drizzle is modeled as spherical in shape with volume-weighted median drop diameter (also called the drop diameter for brevity) in the range [0.005, 0.5] mm and intercept, i.e., $\log_{10}(N_w)$, in the range [3, 6] mm^{-1} m^{-3} (units on D_o and the intercept are, hereafter, dropped). Low-density ice crystals were modeled with diameters in the range [0.2, 0.5] and intercept [2, 3], while high-density ice crystals were modeled with diameters of [0.2 0.5] and intercept [3, 5]. Simulation produced no significant attenuation ($k << 1.0$) for high-density ice crystals. Wet ice is modeled as nearly oblate with a density of 0.5 g cm^{-3}. Particle diameter size was in the range [0.5, 2] with intercept range [2, 4]. Graupel is assumed to be spheroidal with density of $\rho = 0.5$ g cm^{-3}, and diameter size and intercept ranging from [1, 3] and [2, 4], respectively. Small and large hail are assumed wet with high-density ($\rho = 0.9$ g cm^{-3}) ice cores. Small hail was modeled as spheroidal with diameter [5, 20] and intercept [0.95, 1.95]. Large hail was assumed prolate (Doviak and Zrnic, 1984), with diameter in the range [20, 50] and intercept [-2.04, -1.95]. Rain-hail mixture used simultaneous inputs of both small and large hail with rain. Scattergrams of the k-Z_h relationship were constructed for each hydrometeor type, including light rain, and a power law of the form $k = a\, Z_h^b$ was fit to the data.

5.3 Estimation of Attenuation Along PR Beam-Path

5.3.1 PIA Estimation from PR Algorithm

Attenuation correction for TRMM PR is carried out using a hybrid of the Hitschfeld-Bordan and surface reference method (Iguchi, et. al., 2000). The surface reference method observes the apparent decrease in the surface cross section, σ^o, which is assumed to be caused by propagation loss due to rain. The algorithm measures the vertical profile of reflectivity, Z_m, between the cloud top and the lowest height above the surface that is clutter-free. The parameter, α, which depends on the raindrop size distribution and other factors, is adjusted in the k-Z relationship, $k = \alpha\, Z^{\beta}$, given by Hitschfeld and Bordan (1954) in such a way so that the PIA estimate along the vertical profile will match the apparent reduction in σ^o. It is presumed that differences between PIA estimated from σ^o and the measured Z_m profile are due to inappropriate choice of initial α values. This method also assumes that the radar is properly calibrated and works well when the apparent decrease in σ^o is much larger than the fluctuations of the true surface return.

At low rain rate, however, the decrease in σ^o due to attenuation may not be significant and could fall below the natural fluctuations of the surface return. In this case, if the surface return is the only source of error, the Hitschfeld-Bordan method is applied (Iguchi, et. al., 2000). That is, the PIA is estimated from the power-law relationship and reflectivity measurements alone. As the attenuation estimate increases, the PIA estimate from the α-adjustment method is given more weight, thus, the hybrid method prevents the divergence associated with Hitschfeld-Bordan.

5.3.2 PIA Estimation from GR Polarimetric Observations

Data from the TEFLUN-B and TRMM-LBA (Large-Biosphere Atmosphere) field campaigns were collected on August 13, 1998 near Melbourne, FL and from a storm cell on February 25, 1999 near Ji-Parana, Brazil, respectively. After resolution cell matching and alignment, ground radar observations of K_{dp} and Z_h were taken along the TRMM PR beam. The hydrometeor type was determined along the beam path using a fuzzy-logic technique adapted from Liu and Chandrasekar (2000) for SPOL measurements near the tropics, which uses ground-based polarimetric observations. The specific attenuation was determined for high rain rate by measuring K_{dp} along the beam and multiplying it by the k-K_{dp} relationship. For typical range gate spacing of 150 m and measurement accuracy of 2.5° for differential propagation phase (Φ_{dp}), K_{dp} can be determined to an accuracy around $\pm$ 0.3° km^{-1} (Gorgucci, et. al., 2000b). The specific differential propagation phase is estimated here via an iterative range filtering technique based on Hubbert, et. al. (1995). Likewise, Z_h was measured along the beam and the appropriate k-Z_h power law relationship was applied to determine the specific attenuation for the various other hydrometeors present along the beam. Note that for rain the k-K_{dp} relationship was used to determine the specific attenuation when $K_{dp} \geq 0.5$ deg/km, otherwise, a power-law relationship based on the k-Z_h model was used. Though we are making estimates of attenuation for other hydrometeor classes, the classes that matter the most are rain and melting ice. Therefore, it is important to get the percentage of these two hydrometeor types along the propagation path correctly. Even if errors are made in detecting other types of hydrometeors, the impact on attenuation estimation is negligible. Hence, most care was taken to ensure that rain and melting ice were properly detected, and, correspondingly, the attenuation properly estimated.

In practice, the hydrometeor constituents found within the matched resolution volume along the PR beam may not be homogeneous. The specific attenuation within the matched volume is, hence, determined by a weighted average of the relationships for each hydrometeor present in the volume taken from GR observations. The PIA is determined from

$$\mathrm{PIA}(s) = \int_{r=0}^{s} \bar{k}(r)\,dr \qquad (5.7)$$

where s is the beam slant range starting from the cloud top at r = 0, and $\bar{k}(r)$ is the mean-weighted specific attenuation within the matched resolution volume. The PR reflectivity corrected for attenuation is given by:

$$Z_m(PR; k\text{-corrected}) = Z_m(PR) + PIA. \quad (5.8)$$

where $Z_m(PR)$ is the measured (attenuated) PR reflectivity. (The corrected reflectivity derived from this method, as described in equation (11), is alternately referred to as $Z_k(PR)$).

5.4 PIA Estimation Examples with In-Situ Data

An example of attenuation correction along the TRMM PR beam is presented next. Ground radar reflectivity profile at 2 km CAPPI (constant altitude planned position indicator) is shown in Figure 5.3 for the TEFLUN-B campaign on August 13, 1998. The image is volume matched and aligned to PR measurements. Shown on the profile are the locations of three PR beams (A, B and C) drawn to scale. Note that volume matching between GR and PR produces an image with lower resolution than either GR or PR images separately. A vertical profile of GR reflectivity (volume matched and aligned) is shown in Figure 5.4(a) that passes through the PR beam at location A. The PR ray is shown as dotted lines on the profile, which is drawn to scale. Also, on this profile are solid lines indicating the freezing level (0° C isotherm) and PR clutter level (certain) taken from PR 2A23 and 1C21 algorithms, respectively. Polarimetric ground radar observations are plotted with $Z_m(PR; k\text{-corrected})$, $Z_m(PR)$ and the PR attenuation corrected reflectivity, $Z_c(PR)$ (2A25 algorithm), along the TRMM PR beam at this location. Polarimetric ground radar observations include: reflectivity ($Z_m(GR)$), linear depolarization ratio (LDR), cross-correlation coefficient between horizontal and vertical

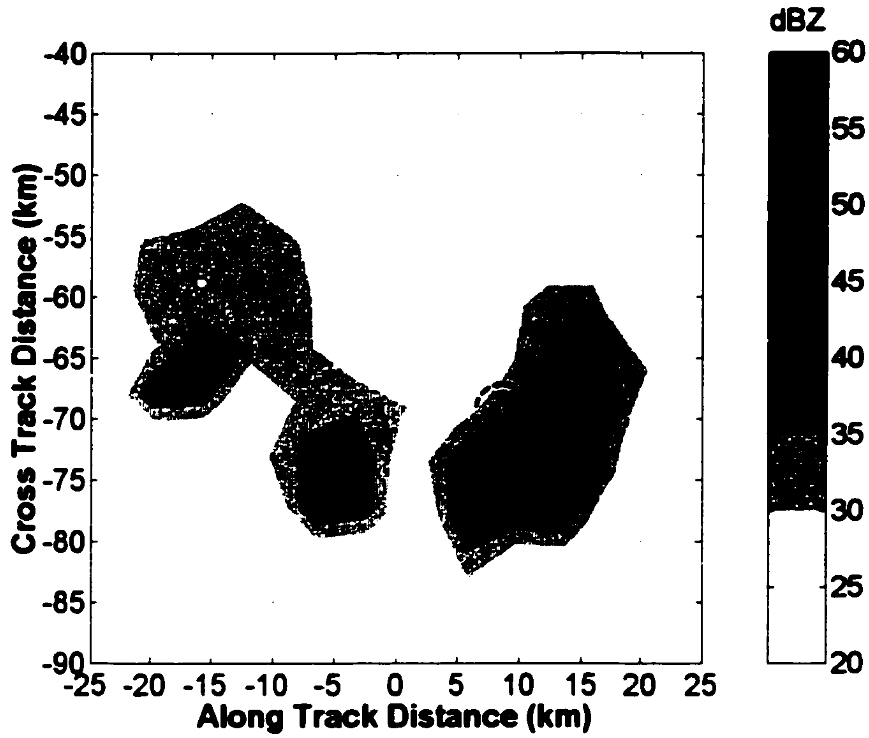

Figure 5.3: TEFLUN-B August 13, 1998. Reflectivity profile of ground radar at 2 km CAPPI, volume matched and aligned to PR measurements. Shown are the locations of PR rays at locations A, B and C, which are drawn to scale.

polarization states (ρ_{co}), specific differential phase (K_{dp}) and differential reflectivity (Z_{dr}). The *ray plot*, showing all of these quantities, for beam A is shown in Figure 5.4 (b). In the ray plot, Z_m(PR) is denoted as black squares, Z_c(PR) as white squares and Z_m(GR) as stars. The corrected reflectivity, Z_k(PR), is shown as a solid line. Similarly, vertical profiles of GR reflectivity that pass through PR beam locations B and C along with their corresponding ray plots are shown in Figure 5.4 (c) (vertical profile) and (d) (ray plot) for ray B, and Figure 5.4 (e) (vertical profile) and (f) (ray plot) for ray C.

If Z_m(GR) is taken as the true vertical profile of reflectivity, then in Figure 5.4 (b) Z_c(PR) is seen to slightly over-estimate the attenuation. For this case, the corrected reflectivity, Z_k(PR) does a better job of following the Z_m(GR) vertical profile. Over

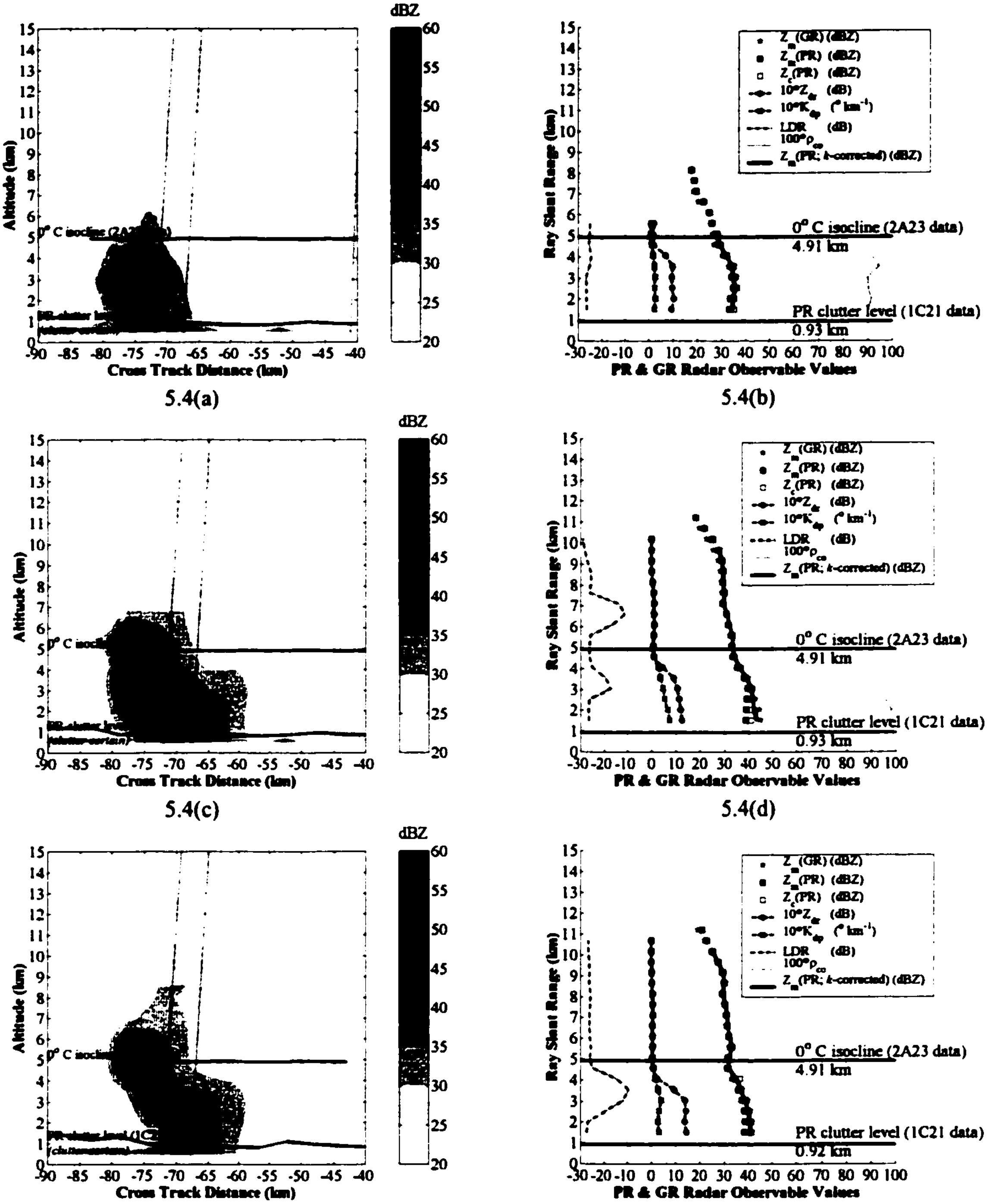

Figure 5.4(a-f): TEFLUN-B August 13, 1998. (a) Shown is the vertical profile of GR reflectivity along the PR scan that passes through beam location A (as depicted in Figure 5.2). Dotted lines depict PR beam drawn to scale. Solid horizontal lines show 0° C isotherm height and PR clutter level (certain) derived from PR 2A23 and 1C21 data, respectively. (b) Volume matched and aligned ground radar polarimetric observables LDR, Z_{dr}, K_{dp} and ρ_{co}, including Z_m(GR) and Z_m(PR), along PR beam A. The solid line indicates the *k*-corrected reflectivity, Z_m(PR; *k*-corrected), and the white squares show the corrected reflectivity derived from the PR 2A25 algorithm. Panels (c) and (d) same as (a) and (b), respectively, for beam at location B. Panels (e) and (f) same as (a) and (b), respectively, for beam at location C.

correction of Z_c(PR) could be due to over-estimation of the hydrometeor size found in the PR beam path. In Figure 5.4(d), attenuation is modest and the PR attenuation correction is seen to under-estimate the GR vertical profile. Again, this under-correction could be due to an under-estimate of the drop size along the PR beam. The profile of Z_k(PR) for this ray is found to closely match the GR profile. The PR ray plot for PR beam C is shown in Figure 5.4(f). Here, attenuation is again modest. The PR attenuation algorithm adequately compensates for attenuation effects and closely matches both Z_m(GR) and Z_k(PR).

Scattergrams of GR measured reflectivity versus PR attenuation corrected reflectivity and *k*-corrected reflectivity were constructed for comparison purposes. Also, histograms of the difference between ground measured reflectivity and PR corrected reflectivity (Z_m(GR) – Z_c(PR)), and the difference between GR reflectivity and attenuation corrected reflectivity derived from GR polarimetric observations (Z_m(GR) – Z_k(PR)) were constructed for the TEFLUN-B and TRMM-LBA data sets (for altitudes $\geq$ 1.5 km). For TEFLUN-B data, the scattergram of Z_m(GR) versus Z_c(PR), when PR reflectivity is 3 dB above the receiver noise floor and PR and GR points are in alignment, is shown in Figure 5.5(a). Similarly, the scattergram for Z_m(GR) versus Z_k(PR) is shown in Figure 5.5 (b). The solid lines on either side of the major diagonal line in each of the plots indicates the standard deviation of the difference between GR and PR points about the mean of their difference. The plots in Figure 5.5 (a) and (b) show, on average, good agreement with Z_m(GR) for both methods. The mean difference between Z_m(GR) and Z_c(PR) is –0.52 dB with standard deviation 3.1 dB, and is –0.30 dB and 3.0 dB, respectively, for the difference with Z_k(PR). The histogram of differences for this data

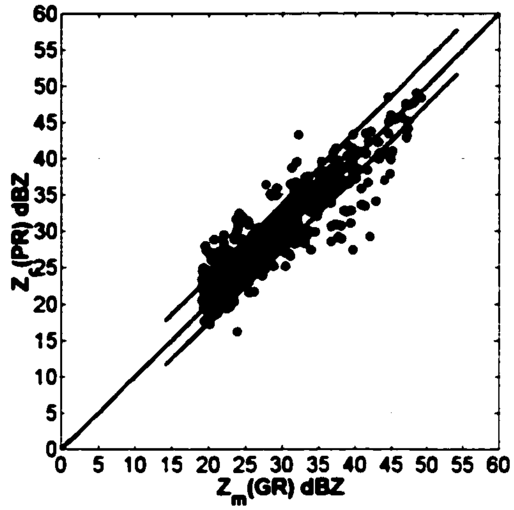

5.5(a)

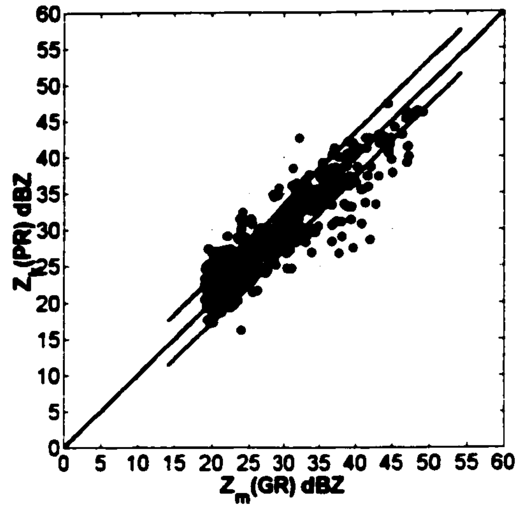

5.5(b)

Figure 5.5 (a-b): TEFLUN-B August 13, 1998. Shown, after volume matching and alignment, are the scattergrams of attenuation corrected reflectivity from the PR algorithm and *k*-corrected algorithm for points where PR is 3 dB above its receiver noise floor and PR and GR points are in alignment, for altitude $\geq$ 1.5 km. The solid lines on either side of the major diagonal indicate the standard deviation about the mean difference between PR and GR values. (a) Measured ground radar reflectivity versus PR algorithm corrected reflectivity with mean –0.52 dB and standard deviation 3.1 dB. (b) GR measured reflectivity versus *k*-corrected reflectivity with mean –0.30 dB and standard deviation 3.0 dB.

set is shown in Figure 5.6(a) and (b) for Z_c(PR) and Z_k(PR), respectively. Mean negative differences in the histograms indicate over-correction while mean positive differences indicate under-correction of attenuation for the two methods. The mean value of the difference for each of the histograms is denoted by a solid line in each figure. The percentage of values of the differences between Z_m(GR) and Z_c(PR) that fall within $\pm$3 dB of the mean value is 75%, whereas it is 76% for the differences between Z_m(GR) and Z_k(PR). Most of the spread about the mean in both Figures 5 and 6 is caused by geolocation alignment problems. However, it is important to note that there is no systematic shift in either direction.

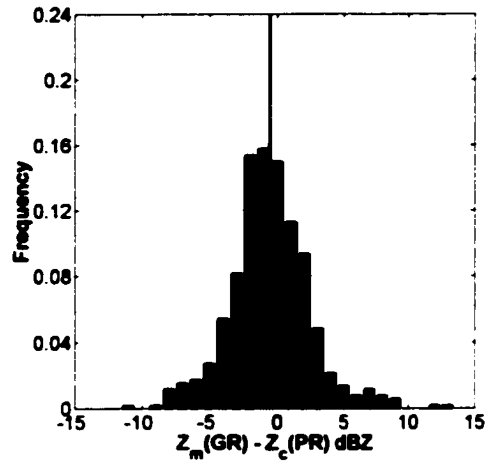

5.6(a)

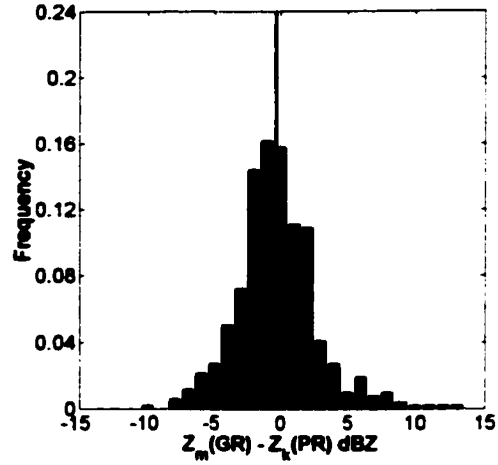

5.6(b)

Figure 5.6 (a-b): TEFLUN-B August 13, 1998. Histograms of the difference between GR reflectivity measurements and attenuation corrected reflectivities derived from the PR 2A25 algorithm and the GR *k*-corrected algorithm, for altitude $\geq$ 1.5 km. Negative differences indicate over-estimation while positive differences indicate under-estimation. The mean value is indicated by the solid vertical line. (a) Histogram for Z_m(GR) – Z_c(PR). The mean is –0.52 dB with 75% of the values falling within $\pm$3 dB of this value. (b) Histogram for Z_m(GR) – Z_k(PR). The mean is –0.30 dB with 76% of the values falling within $\pm$3 dB of this value.

In a like manner, the scattergrams for the TRMM-LBA case are shown in Figure 5.7(a) and (b) for Z_m(GR) versus Z_c(PR), and for Z_m(GR) versus Z_k(PR), respectively. Again, there is good agreement between the measured GR reflectivity and attenuation corrected reflectivity from the two methods. The mean difference between Z_m(GR) and Z_c(PR) for this case is –0.39 dB with standard deviation of 2.1 dB. This is –0.35 dB and 2.0 dB for the mean and standard deviation, respectively, for the scattergram between Z_m(GR) and Z_k(PR).The histograms of the differences between Z_m(GR) and the corrected reflectivities from the two methods are shown in Figure 5.8(a) and (b) for Z_c(PR) and Z_k(PR), respectively. The percentage of values of the difference that are within $\pm$3 dB of the mean for Z_m(GR) – Z_c(PR) is about 85% and for Z_m(GR) – Z_k(PR) is 86%.

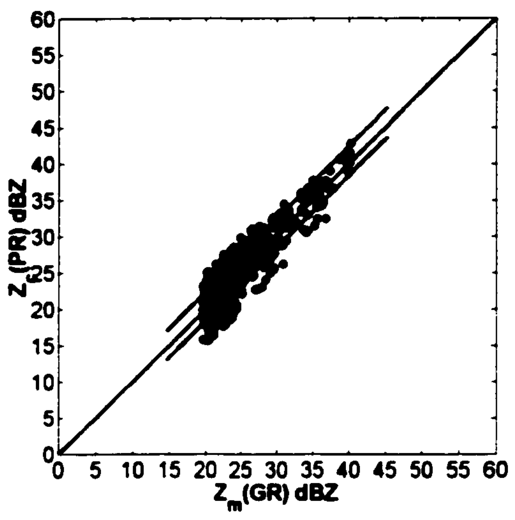

5.7(a)

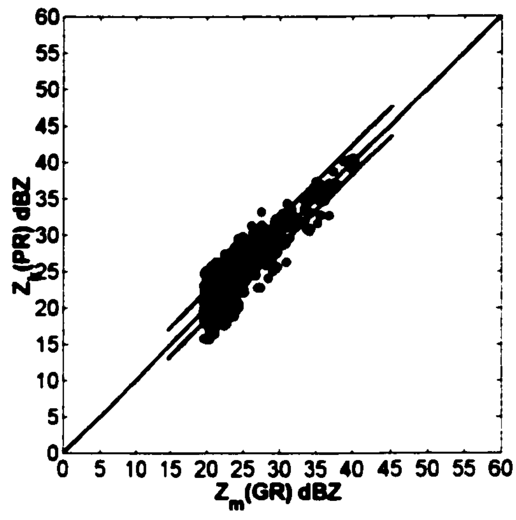

5.7(b)

Figure 5.7 (a-b): TRMM-LBA February 25, 1999. Shown, after volume matching and alignment, are the scattergrams of attenuation corrected reflectivity from the PR algorithm and *k*-corrected algorithm for points where PR is 3 dB above its receiver noise floor and PR and GR points are in alignment, for altitude $\geq$ 1.5 km. The solid lines on either side of the major diagonal indicate the standard deviation about the mean difference between PR and GR values. (a) Measured ground radar reflectivity versus PR algorithm corrected reflectivity with mean –0.39 dB and standard deviation 2.1 dB. (b) GR measured reflectivity versus *k*-corrected reflectivity with mean –0.35 dB and standard deviation 2.0 dB.

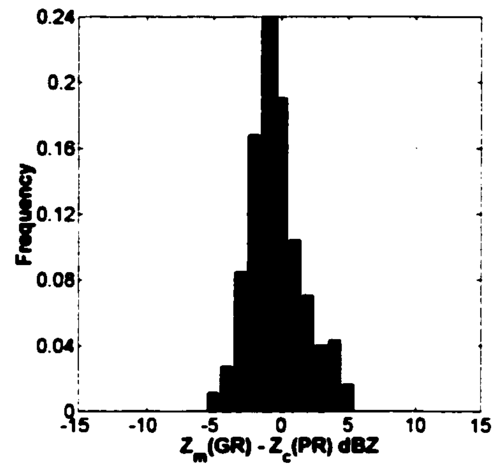

5.8(a)

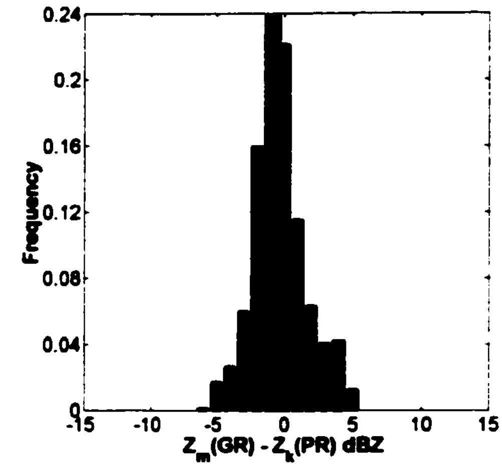

5.8(b)

Figure 5.8 (a-b): TRMM-LBA February 25, 1999. Histograms of the difference between GR reflectivity measurements and attenuation corrected reflectivities derived from the PR 2A25 algorithm and the GR *k*-corrected algorithm, for altitude $\geq$ 1.5 km. Negative differences indicate over-estimation while positive differences indicate under-estimation. The mean value is indicated by the solid vertical line. (a) Histogram for Z_m(GR) – Z_c(PR). The mean is –0.39 dB with 85% of the values falling within $\pm$3 dB of this value. (b) Histogram for Z_m(GR) – Z_k(PR). The mean is –0.35 dB with 86% of the values falling within $\pm$3 dB of this value.

Finally, a scattergram between the two-way PIA derived from the PR attenuation correction algorithm and Z_k(PR) is shown in Figure 5.9 (for altitude between 1.5 and 4 km) using data from both TEFLUN-B and TRMM-LBA data sets. Data from Melbourne, FL is shown as white circles, while the data from Ji-Parana, Brazil is shown as black circles. In the scattergram, the scatter is fairly evenly dispersed about a one-to-one relationship for PIA values less than about 5 dB. For larger PIA estimates, a relatively small bias is seen between the values derived from the PR algorithm, and the ground radar based attenuation. This difference is possibly due to gradients within the PR beam where attenuation correction is implemented. In the GR algorithm, the data is of higher resolution, and therefore, an average propagation constant for the non-uniform beam is explicitly evaluated. However such a procedure is not possible with PR, which could possibly explain the difference between the two attenuation estimates.

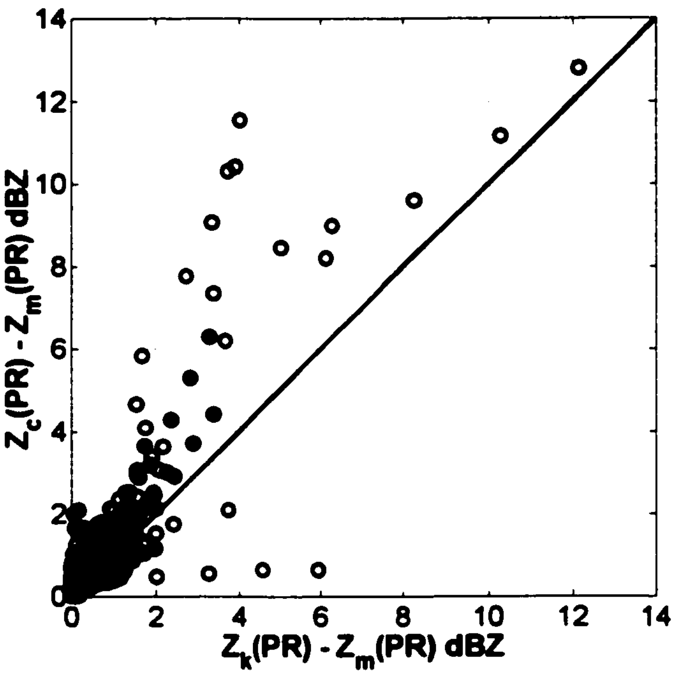

Figure 5.9: Two-way path-integrated-attenuation (PIA) derived from *k*-corrected algorithm versus that derived from the PR attenuation correction algorithm, for altitude between 1.5 and 4 km. Data from August 13, 1998 data taken from Melbourne, FL are shown as white circles, while data from February 25, 1999 taken from Ji-Parana, Brazil are shown as black circles. The scatter is fairly dispersed (about the linear relationship depicted by the solid diagonal black line) for PIA values less than about 5 dB, but are somewhat biased (about 2 dB) toward the PIA derived from the PR algorithm PIA for values greater than this.

5.5 Summary

Attenuation effects on high-frequency spaceborne radars can have a significant impact on rainfall rate retrieval algorithms. A method for quantitatively determining the attenuation of space-based radar signals, along individual space radar beams, using ground-based polarimetric observations has been presented. A theoretical model was developed that related specific attenuation of high-frequency spaceborne signals with ground-based Z_h and K_{dp} observations for various hydrometeor types. From this the two-way PIA was calculated along the SR beam. The method was validated by applying it to experimental data collected during the TEFLUN-B and TRMM-LBA field campaigns. The first important conclusion is that there does not seem to be a systematic under-correction or over-correction of the TRMM PR algorithm in a gross sense, though this may happen on a beam-by-beam basis. And, secondly, the two-way path-integrated attenuation derived from ground radar compares well with those obtained using the TRMM PR algorithm. However, the level of agreement needs to be assessed over an extensive data set. Finally, the mean value of the difference between GR and PR, after attenuation correction, seems to be within 1 dB with a standard deviation of about 2 to 3 dB. Though most of the standard deviation could be due to geolocation alignment problems, it gives and idea about the upper limit of the error induced in the reflectivity value due to attenuation correction. The bias between SPOL ground radar and PR over both data sets presented is about –0.46 dB from an analysis of histogram plots of the difference between Z_m(GR) and Z_c(PR), and is –0.33 dB for the difference between Z_m(GR) and Z_k(PR). Furthermore, it was found that 80% of the values of the difference between Z_m(GR) and Z_c(PR) fell within 3 dB of the mean value for both cases. This was found to be 81% for the differences between Z_m(GR) and Z_k(PR).

Chapter 6

EVALUATION OF TRMM PR ATTENUATION CORRECTION ALGORITHM IN CONJUNCTION WITH RAINDROP SIZE DISTRIBUTION (RSD)

6.1 Overview of RSD Estimation

Measurements from polarimetric ground radars (GR) can be used to estimate the raindrop size distribution (RSD) along the space radar beam path to evaluate attenuation correction. The viewing geometry of the two systems is illustrated in Figure 6.1. The polarimetric radar measurements used in this chapter, include the reflectivity factor (at horizontal polarization state), Z_h, the differential reflectivity, Z_{dr}, and specific differential phase, K_{dp}. In particular, Z_h is related to the 6^{th} moment of the raindrop size distribution, Z_{dr} is related to the volume-weighted median drop size, D_o, or the mass-weighted mean diameter, D_m (e.g., Seliga and Bringi, 1976; Aydin et. al., 1987), and K_{dp} is related to the mass-weighted mean axial ratio of the raindrops (Jameson 1985), which can also be approximately related to the 5^{th} moment of the RSD at S-band frequency (Bringi and Chandrasekar, 2001).

For oblate drops, Pruppacher and Beard (1970) formulated an approximate shape-size relationship between the drop axial ratio, r (i.e., the ratio of the drop's minor axis to major axis), and D_e (the equivalent volume drop diameter of a spherical drop) as $r \approx 1 - 0.062\, D_e$. The effects of raindrop oscillations due to resonance maintained by

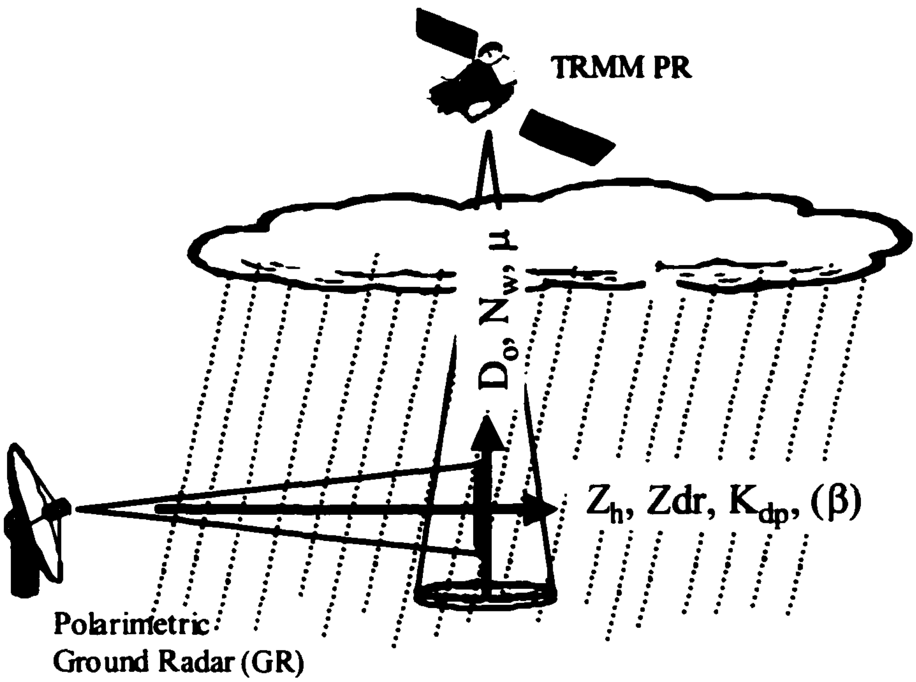

Figure 6.1: Illustration of viewing geometry between TRMM PR and GR based measurements, and observation profiles along the beams.

vortex shedding, or collisions, alter radar observations (Bringi and Chandrasekar, 2001): i.e., drop oscillations and canting will tend, on average, to make the drops *look* less oblate. Using an equivalent linear model between drop shape and size, Gorgucci et al. (2000) incorporated drop canting and oscillations into an estimate for the slope (β) of the shape-size relationship using the measurements of Z_h, Z_{dr} and K_{dp}. Subsequent to this, the retrieval of the RSD parameters was formulated (Gorgucci et al., 2001) for rain rates when $Z_h \geq 35$ dBZ using β and measurements of Z_h and Z_{dr}. At low rain rates, measurements of K_{dp} are noisy at long wavelengths (such as at S-band), which requires some areal averaging to reduce measurement fluctuations. This problem has been addressed by Bringi et al., (2002), and extended the retrieval of the RSD parameters for

$Z_h < 35$ dBZ. These RSD retrieval algorithms discussed in Bringi, et. al. (2002) are used in this chapter to estimate the raindrop size distribution along the TRMM PR beam via ground-based polarimetric observations taken along the beam.

6.2 Theoretical Model of the RSD

Raindrops are shaped by a balance of surface tension and hydrostatic pressure along with aerodynamic constraints (mainly in the vertical direction) due to their fall. Raindrops can be characterized as oblate spheroids and have been studied theoretically by Green (1975), and Beard and Chung (1987), experimentally by Pruppacher and Pitter (1971), and using aircraft probes by Chandrasekar, et. al. (1988). For drops greater than about 1 mm in diameter, the ratio of the minor axis (b) to major axis (a) can be approximated by (Gorgucci, et. al., 2000)

$$r = \frac{b}{a} \approx 1.03 - \beta\, D_e \qquad (6.1)$$

where β is the magnitude of the slope of the shape-size relationship and D_e is the equi-volumetric spherical diameter of the drop in mm. In equation (6.1), $r = 1$ when $D_e \leq 0.03/\beta$. For drops in equilibrium, a commonly used approximation for β is 0.062 mm^{-1}, as given by Pruppacher and Beard (1970). It is noted that, according to equation (6.1), for values of β less than the equilibrium value, drops are less oblate (or, closer to spherical), and for values greater than this they are more oblate.

Models and measurements of the RSD, both at the surface and aloft, indicate that a gamma distribution is adequate for describing the natural variations in the RSD (Ulbrich, 1983). The normalized form of the gamma model (Testud, et. al., 2001; Willis, 1984; and, Bringi and Chandrasekar, 2001), is given by

$$N(D) = N_W \, f(\mu)\left[\frac{D}{D_o}\right] e^{-(3.67+\mu)\frac{D}{D_o}} \tag{6.2}$$

where

$$f(\mu) = \frac{6}{(3.67)^4}\frac{(3.67+\mu)^{\mu+4}}{\Gamma(\mu+4)} \tag{6.3}$$

where N(D) is the number of raindrops per unit volume per unit size in the interval (D,D+ΔD), N_w is the normalized slope intercept parameter of an equivalent exponential RSD (which has the same water content and median volume drop diameter, D_o, as the gamma RSD), μ is the shaping factor and $\Gamma(\,)$ represents the gamma function.

Determination of the RSD is of central importance in describing the properties of the rain medium. Polarimetric radar measurements such as the reflectivity factor, $Z_{h,v}$ (where h and v denote the horizontal and vertical polarization states, respectively), differential reflectivity, Z_{dr}, and specific differential propagation phase, K_{dp}, can be expressed in terms of the RSD as follows:

$$Z_{h,v} = \frac{\lambda^4}{\pi^5 |k|^2} \int \sigma_{h,v}(D) N(D) dD \qquad (mm^6\, m^{-3}) \qquad (6.4)$$

where $\sigma_{h,v}$ is the radar cross-section at horizontal and vertical polarization states, respectively, λ represents the wavelength, and $k = (\varepsilon_r - 1)/(\varepsilon_r + 2)$ where ε_r is the dielectric constant of water;

$$Z_{dr} = \frac{\int \sigma_h(D) N(D) dD}{\int \sigma_v(D) N(D) dD}\text{; and,} \qquad (dB) \qquad (6.5)$$

$$K_{dp} = \frac{180\lambda}{\pi} \Re \int [f_h(D) - f_v(D)] N(D) dD \qquad (deg\, km^{-1}) \qquad (6.6)$$

where $\Re$ refers to the real part of a complex number and f_h and f_v are the forward scattering amplitudes at h and v polarization states, respectively.

Gorgucci et. al. (2001) obtained an estimate for β (at S band) as

$$\beta = a\, Z_h^b\, K_{dp}^c\, \xi_{dr}^d \qquad (6.7)$$

where, $\xi_{dr} = 10^{0.1 Z_{dr}}$. At S-band, the coefficients in equation (6.7) are a = 2.08, b = -0.365, c = 0.380 and d = 0.965. The median volume drop diameter, D_o, normalized slope intercept, N_w, and shaping parameter, μ, can be derived from polarimetric observations and β, which, at S-band wavelength, are given as (Gorgucci, et. al., 2001):

$$D_o = a_1 Z_h^{b_1} (\xi_{dr})^{c_1} \quad \text{(mm)} \tag{6.8}$$

with $a_1 = 0.595\beta^{0.0353}$, $b_1 = 0.0242\beta^{-0.359}$ and $c_1 = 0.103\beta^{-0.91}$;

$$\log_{10}(N_w) = a_2 Z_h^{b_2} (\xi_{dr})^{c_2} \tag{6.9}$$

with $a_2 = 3.12\beta^{0.0201}$, $b_2 = 0.176\beta^{0.376}$ and $c_2 = -0.101\beta^{-0.897}$ (N_w in units of mm^{-1} m^{-3}); and,

$$\mu = \frac{a_3 D_o^{b_3}}{(\xi_{dr} - 1)} - c_3 (\xi_{dr})^{d_3} \tag{6.10}$$

with $a_3 = 200\beta^{1.89}$, $b_3 = 2.23\beta^{0.039}$, $c_3 = 3.16\beta^{-0.046}$ and $d_3 = 0.374\beta^{-0.355}$. The equations (6.8-10) are valid for $Z_h \geq 35$ dBZ, $Z_{dr} \geq 0.2$ dB and $K_{dp} \geq 0.3$ ° km^{-1}. Bringi, et. al. (2002), extended the functional behavior of the RSD to lower rain rate events where measurements of K_{dp} are noisy, and those algorithms are used in this chapter.

6.3 RSD Estimation Along PR Beam-Path

The estimation of the RSD parameters along the TRMM PR beam is illustrated using one of the case studies. Figure 6.2(a) shows the vertical cross section of GR reflectivity for one of the storm cells taken from the TRMM-LBA campaign on February 25, 1999. This storm cell, henceforth referred to as cell A, was located to the northwest of the ground radar location. In figure 6.2(a) the PR beam is indicated, drawn to scale and orientation, by the two nearly vertical solid lines. Also shown are the freezing level altitude and PR clutter level (certain), indicated by the solid horizontal lines, as derived from the PR 2A23 and 2A25 algorithms, respectively. Figure 6.2(b) is a plot of the ground polarimetric radar observations, and PR measurements, along the PR beam.

Shown, from left to right, are the linear depolarization ratio (LDR), specific differential phase (K_{dp}) (scaled by 10), differential reflectivity (Z_{dr}) (scaled by 10), PR attenuated reflectivity measurements (Z_m(PR)), PR attenuation corrected reflectivity (Z_c(PR)), GR reflectivity measurements (Z_m(GR)), and the cross-correlation coefficient between the GR return signal at horizontal and vertical polarization states (ρ_{co}) (scaled by 100). For this beam, GR polarimetric observations generally indicate rain below the melting altitude level. If GR reflectivity is taken as the reference, it can be seen that attenuation on PR return is moderate (about 7 dB) and that the PR attenuation correction slightly under-estimates the attenuation (by about 2 dB). The estimates of the gamma distribution model parameters (N_w, D_o and μ) for rain along the PR beam, for this example, are shown in figure 6.2(c). The parameters $\log_{10}(N_w)$ and D_o are shown as solid lines, and are labeled accordingly. The shape parameter, μ, is shown as a dotted line (also labeled).

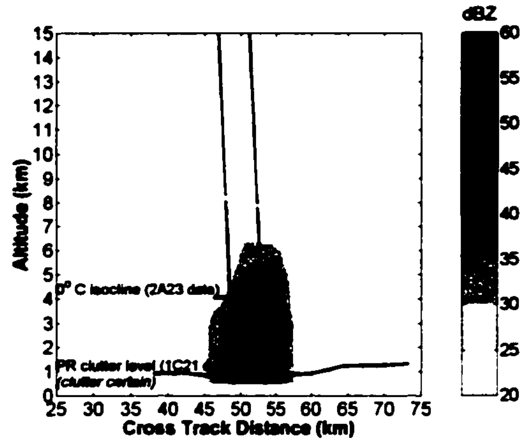

6.2(a)

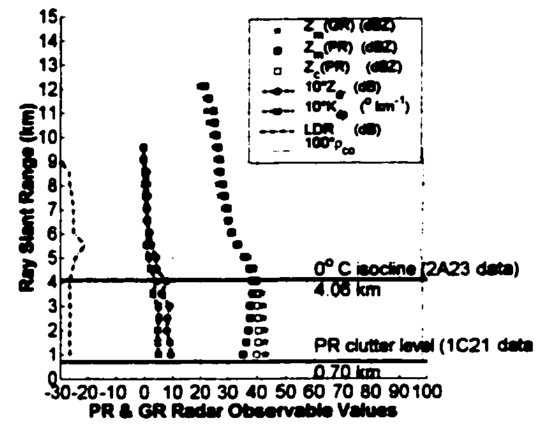

6.2(b)

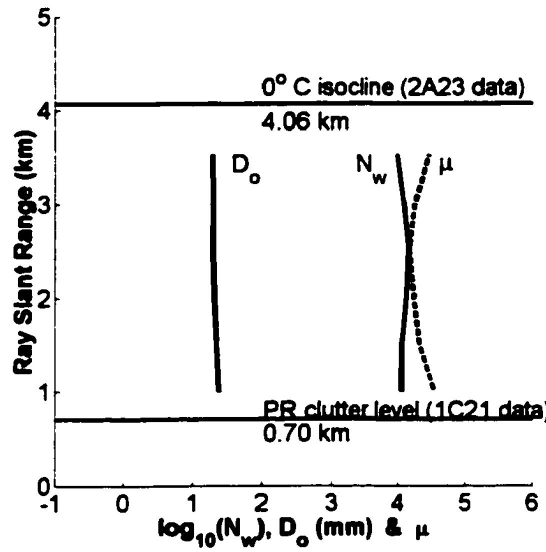

6.2(c)

Figure 6.2: Example of ground based observations and RSD estimates from data using TRMM-LBA storm cell A. (a) Vertical profile of GR reflectivity with location of PR beam indicated by solid vertical lines drawn to scale. (b) GR polarimetric observations along PR ray corresponding to the ray as indicated in panel (a). From left to right, the dashed line is LDR, solid line with x's is K_{dp} (scaled by a factor of 10), solid line with circles is Z_{dr} (scaled by 10), black squares are PR measured (attenuated) reflectivity, white squares are PR attenuation corrected reflectivity, stars are GR measured reflectivity and the dotted line is the cross-correlation coefficient between GR return signal horizontal and vertical polarization states, ρ_{co} (scaled by 100). In this plot, PR attenuation is observed to be about 7 dB with reference to GR measurements. (c) Estimates of the RSD along PR ray corresponding to the ray indicated in panel (a) for altitudes between the PR clutter level and isocline height. Solid vertical lines indicate D_o, and N_w (as labeled), while the dotted is the parameter, μ. In all panels, solid horizontal lines indicate the 0° C isocline altitude and the PR clutter level (certain), as derived from the PR 2A25 and 1C21 data products, respectively.

The drop size diameter is seen to be fairly constant (about 1.2 mm) in the rain layer (i.e., in the altitudes below the freezing level, but above the PR clutter altitude) along the PR beam. Likewise, $\log_{10}(N_w)$ is also fairly constant at about 4. The shape parameter varies somewhat, but is between 4 and 4.5.

6.4 Statistical Analysis of the RSD through the Vertical Profile

In figures 6.3, 6.4 and 6.5, histograms of the values of the RSD parameters D_o, N_w and μ are shown as a function of altitude. That is, the histogram of the parameter values across the horizontal plane at incremental altitudes is determined and the frequency plotted. The result is the frequency of occurrence of the parameter value (shown along the abscissa) as a function of altitude (ordinate axis), henceforth referred to as an altitude-histogram chart. This is done for each of the case studies: TEFLUN-B from August 13 and 15, 1998 and TRMM-LBA from two different storm cells on February 25, 1999. Note that the storm cells for the TRMM-LBA data are labeled as A and B for the cells located northwest and southwest of the GR location, respectively (also referred to as the February 25A and February 25B, 1999 cells, respectively). In these charts, darker areas indicate a higher frequency of occurrence of the parameter value across the horizontal plane at a particular altitude. The solid line in the figures indicates the mean value of the parameter through the vertical profile, and the dashed lines indicated the standard deviation about the mean profile.

Shown in figure 6.3(a) is the altitude-histogram chart for D_o for August 13, 1998. The mean value of the drop size through the vertical profile of the storm cell is about 1.34

mm, and is fairly constant with average standard deviation of 0.28 mm. Likewise, the altitude-histogram charts for August 15, 1998 and February 25A and 25B, 1999 are shown in figures 6.3(b), (c) and (d), respectively. In figure 6.3(b), the mean diameter is as large as 2.0 mm near the surface, and is about 1.7 near the freezing level. However, below 3 km in altitude, the mean D_o remains nearly constant at about 2.0 mm. The

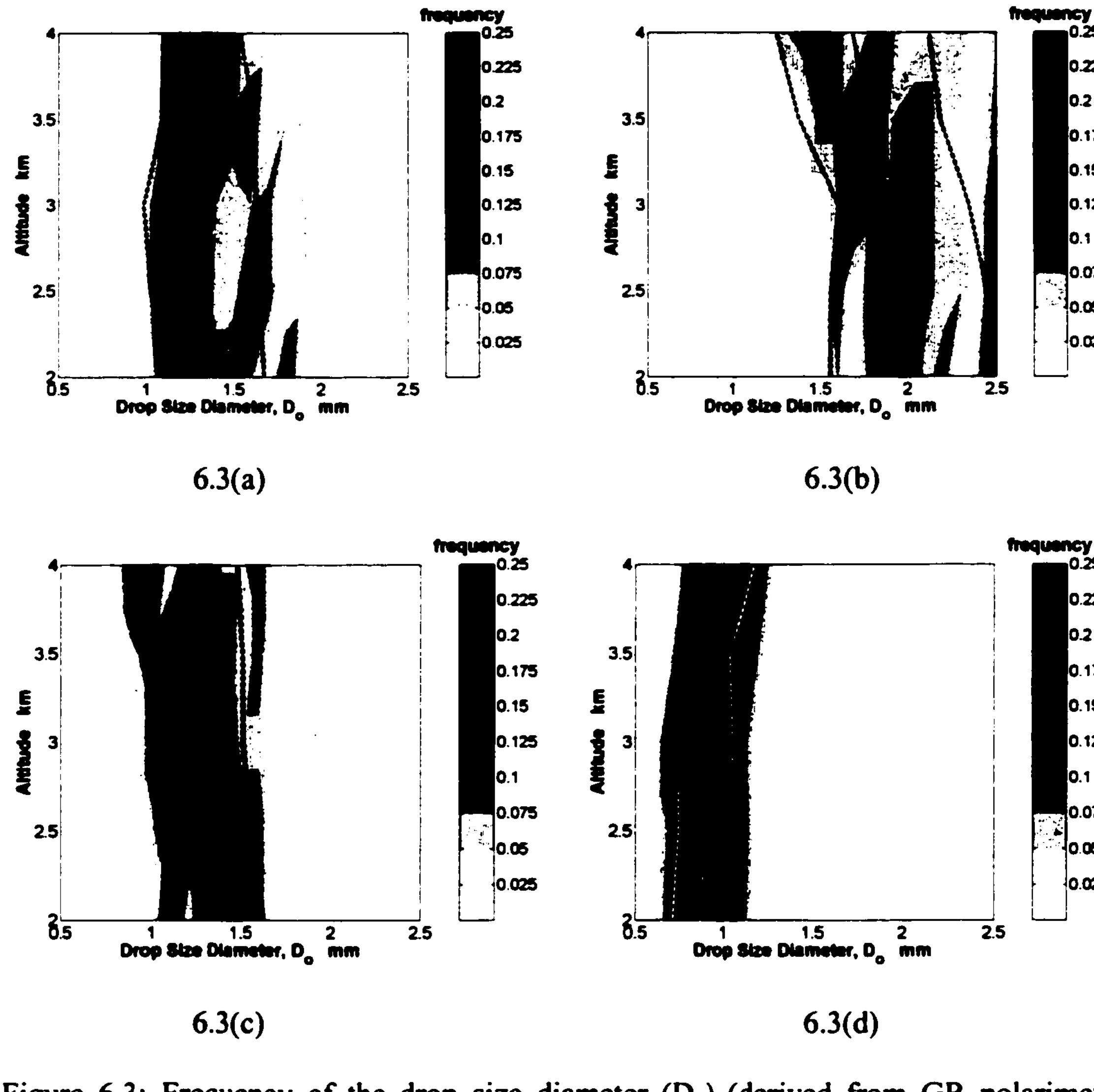

Figure 6.3: Frequency of the drop size diameter (D_o) (derived from GR polarimetric observations) across each altitude in the storm cell, below the isocline level and above the PR clutter noise floor (certain). Solid line in panels (a), (b), (c), and white line in panel (d), indicates the median drop diameter. Darker shades indicate higher frequency of occurrence. (a) TEFLUN-B, August 13, 1998, (b) TEFLUN-B, August 15, 1998, (c) TRMM-LBA, February 25A, 1999 and (d) TRMM-LBA, February 25B, 1999.

standard deviation for the distribution through the profile is about 0.42 mm. In figure 6.3(c), the mean drop diameter is about 1.28 mm, and is fairly constant with standard deviation of 0.25 mm. The range of drop sizes is less than about 1.25 mm for the LBA case B (February 25B), as shown in figure 6.3(d). Here, the mean drop diameter is less than one and is about 0.92 mm. The average standard deviation is 0.15 mm. Though there may be some spread in drop diameters in each of the case studies (as indicated in their respective histograms), the mean value is fairly constant through the vertical profile below 3 km in altitude.

The altitude-histogram charts for the intercept (i.e., $\log_{10}(N_w)$ with N_w in units of $mm^{-1}m^{-3}$) for each of the case studies are shown in figures 6.4(a-d), where each of the figures (a through d) correspond to the TEFLUN-B and LBA cases as described for the figures 6.3(a-d), respectively. In figure 6.4(a), the mean value of the intercept is fairly constant with average value of 3.0 through the vertical profile. The average standard deviation is about 0.6. In figure 6.4(b), the intercept has mean value of 2.6 with average standard deviation of 0.7. Similarly, for the LBA cases: in figure 6.4(c), the average intercept value is 3.5 with standard deviation of 0.6. In figure 6.4(d), the intercept is about 4.3 through the profile with standard deviation of 0.5.

The altitude-histogram charts for the gamma distribution shape parameter, μ, for each of the case studies are shown in figures 6.5(a-d), corresponding to the TEFLUN-B and TRMM-LBA cases as described per figures 6.3(a-d), respectively. For the TEFLUN-B case in figure 6.5(a), the parameter, μ, is about 3.1 on average through the vertical profile with average standard deviation of 2.2. In figure 6.5(b), the shape parameter is fairly constant with average value of 2.6 and standard deviation of 1.2. For the LBA case,

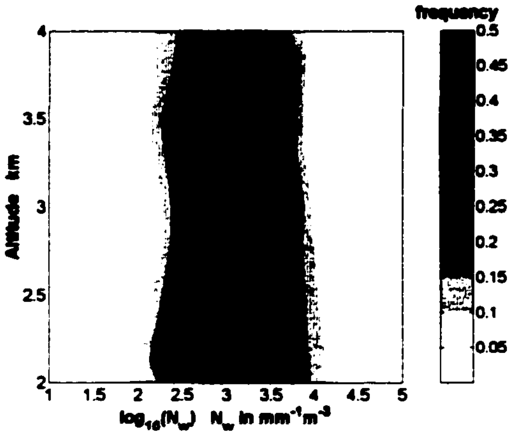

6.4(a)

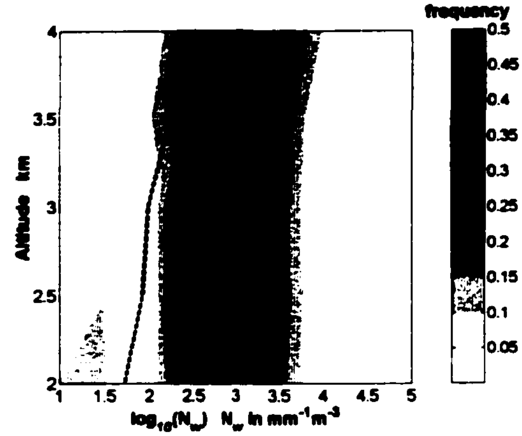

6.4(b)

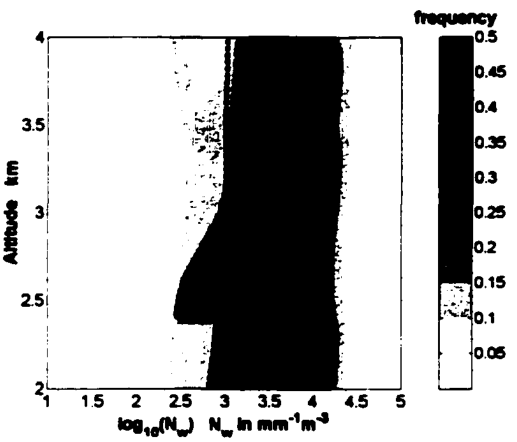

6.4(a)

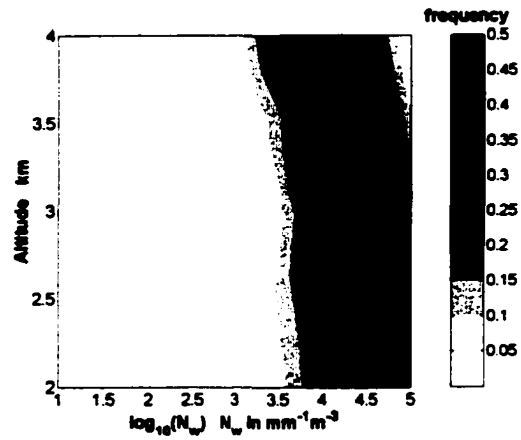

6.4(b)

Figure 6.4: Frequency of the intercept parameter (i.e., $\log_{10}(N_w)$) (derived from GR polarimetric observations) across each altitude in the storm cell, below the isocline level and above the PR clutter noise floor (certain). Solid line in panels (a), (b), (d), and white line in panel (c), indicates the median value of $\log_{10}(N_w)$. Darker shades indicate higher frequency of occurrence. (a) TEFLUN-B, August 13, 1998, (b) TEFLUN-B, August 15, 1998, (c) TRMM-LBA, February 25A, 1999 and (d) TRMM-LBA, February 25B, 1999.

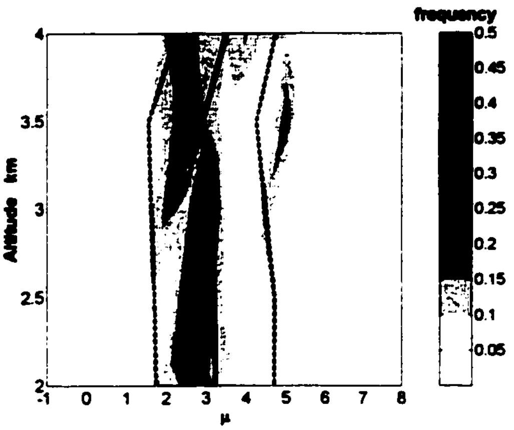

6.5(a)

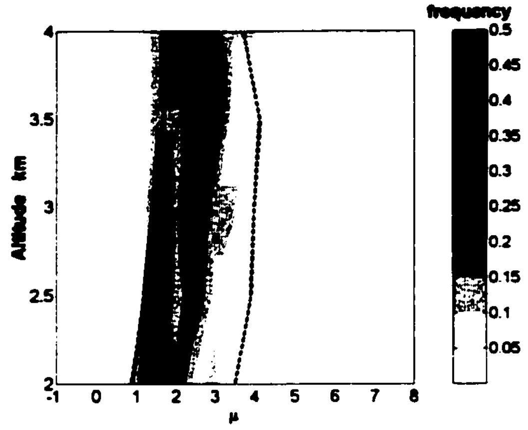

6.5(b)

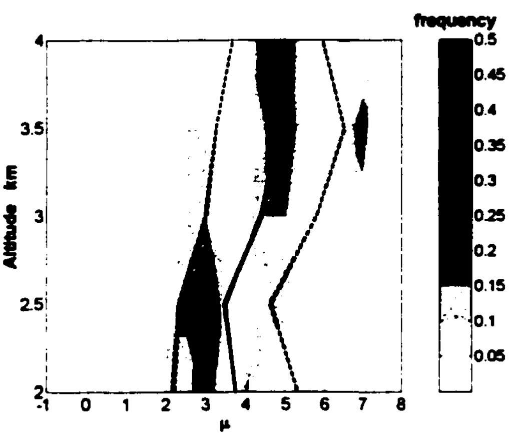

6.5(a)

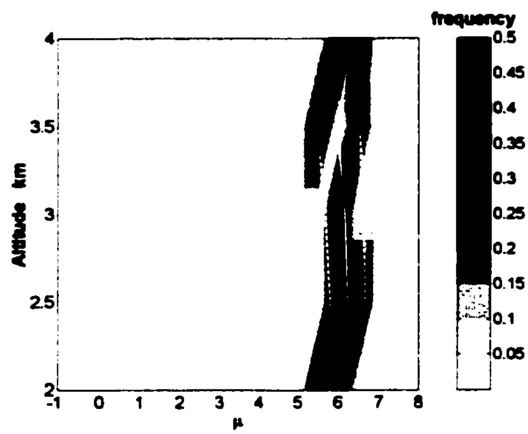

6.5(b)

Figure 6.5: Frequency of the slope parameter (μ) (derived from GR polarimetric observations) across each altitude in the storm cell, below the isocline level and above the PR clutter noise floor (certain). Solid line in panels (a), (b), (d), and white line in panel (d), indicates the median value of μ. Darker shades indicate higher frequency of occurrence. (a) TEFLUN-B, August 13, 1998, (b) TEFLUN-B, August 15, 1998, (c) TRMM-LBA, February 25A, 1999 and (d) TRMM-LBA, February 25B, 1999.

February 25A, 1999, μ is about 4.3 on average. The mean value, however, fluctuates between 3.5 and 4.5 along the vertical profile with standard deviation of 1.4 on average. The μ parameter for the LBA case shown in figure 6.5(d) is fairly narrow with an average value of 6.0 and average standard deviation of 0.3. It should be noted here that Gorgucci, et. al. (2001) indicate that the estimates of μ are not as accurate as for the other two parameters. These values of μ are also in the neighborhood of the assumptions made in the TRMM PR algorithm. A summary of the average value and the average standard deviation of the vertical profiles for Do, log10(Nw) and μ for each of the case studies is given in Table 6.1.

Table 6.1: Summary of the average values of the mean and standard deviation (σ) of D_o, $\log_{10}(N_w)$ and μ through the vertical profile (2-4 km altitude) for each of the case studies.

case study	average D_o mm	$\sigma(D_o)$ mm	average $\log_{10}(N_w)$ N_w in mm^{-1} m^{-3}	$\sigma(\log_{10}(N_w))$ N_w in mm^{-1} m^{-3}	μ	$\sigma(\mu)$
Aug 13, 1998	1.34	0.28	3.00	0.60	3.10	2.20
Aug 15, 1998	2.00	0.42	2.60	0.70	2.60	1.20
Feb 25A, 1999	1.28	0.25	3.50	0.60	4.30	1.40
Feb 25B, 1999	0.92	0.15	4.30	0.50	6.00	0.30

Similar altitude-histogram charts were also constructed for the difference between measured GR reflectivity values, $Z_m(GR)$, and PR attenuation corrected reflectivity, $Z_c(PR)$. These charts are shown in figures 6.6(a-d), and, likewise, correspond to the case studies described for figures 6.3(a-d), respectively. The mean value of the difference, $Z_c(PR)$ - $Z_m(GR)$, is shown as a solid line running through the vertical profile with the standard deviation shown as a dashed line. A grid line at 0 dB difference is shown as a

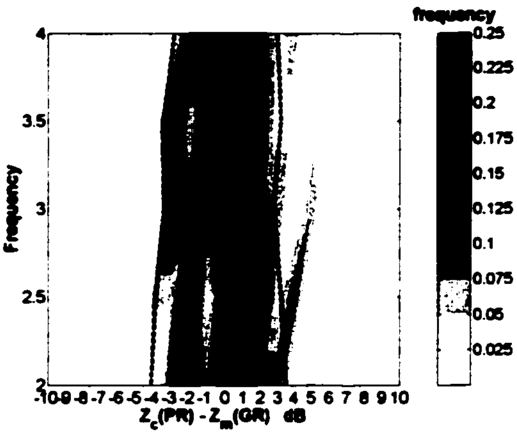

6.6(a)

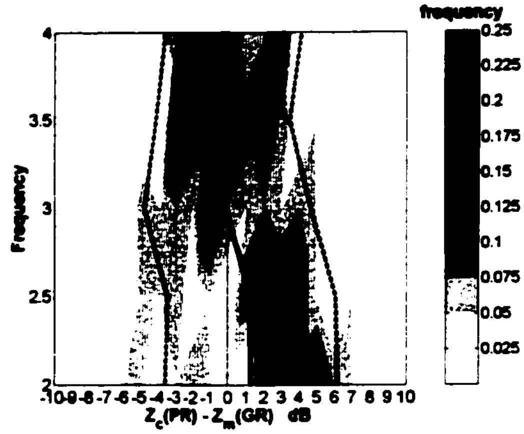

6.6(b)

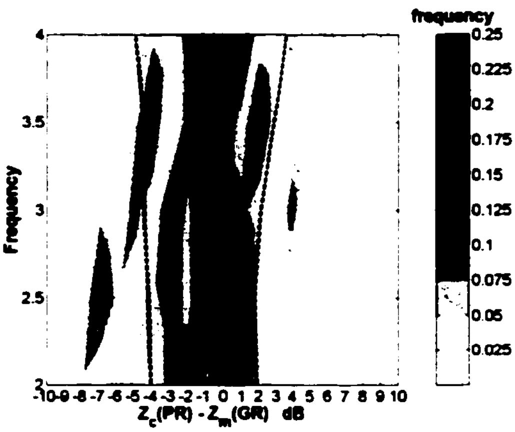

6.6(a)

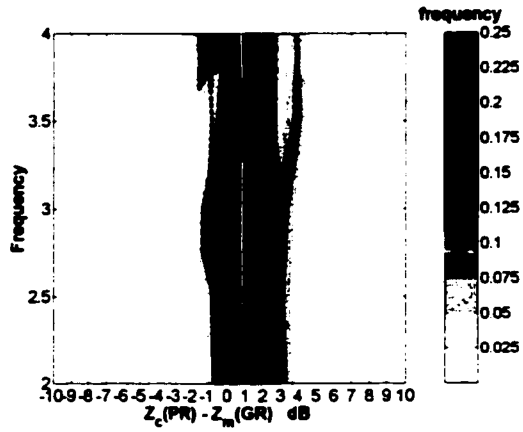

6.6(b)

Figure 6.6: Frequency of the reflectivity difference, Z_m(GR) - Z_c(PR), across each altitude in the storm cell, below the isocline level and above the PR clutter noise floor (certain). The solid line in each of the panels indicates the median value of the difference, and the vertical dashed line is a grid line at 0 dB difference. Darker shades indicate higher frequency of occurrence. (a) TEFLUN-B, August 13, 1998, (b) TEFLUN-B, August 15, 1998, (c) TRMM-LBA, February 25A, 1999 and (d) TRMM-LBA, February 25B, 1999.

dotted line for reference. In figure 6.6(a), the mean value of the difference is nearly constant and close to -0.2 dB through the vertical profile. The average standard deviation for this case is about 3.4 dB. For the TEFLUN-B, August 15, case shown in figure 6.6(b), the difference in Z_c(PR) and Z_m(GR) is nearly zero above 3 km altitude. However, below this altitude, the difference in measurements can be as high as 1 dB. If

Z_m(GR) is taken as the truth data, then this indicates a slight over-estimation in Z_c(PR) at lower altitudes. The average difference through the profile is 0.5 dB, and the average standard deviation is about 4.5 dB. In figure 6.6(c), the difference between PR attenuation-corrected reflectivity and GR reflectivity is about –1.0 dB with standard deviation of 3.5 dB. This result indicates a slight under-correction of PR algorithm compared to ground radar measurements. For the LBA case (storm cell B) shown in figure 6.6(d), the average difference between Z_c(PR) and Z_m(GR) is slightly positive along the vertical profile with mean value of 0.9 dB and standard deviation of 1.7 dB, indicating a slight over-correction of the PR correction algorithm. The average difference, and average standard deviation of the difference, for the vertical profile for each of the case studies is given in Table 6.2. These histograms essentially indicate a storm-by-storm variability in the attenuation correction algorithm, and the variability in the difference in both the positive and negative directions (i.e., there is no systematic difference in one direction).

Table 6.2: Summary of the average difference and standard deviation (s) of the difference between PR and GR through the vertical profile (2 – 4 km altitude) for each of the case studies. Note that a positive difference indicates PR algorithm over-estimating.

case study	average Z_c(PR) - Z_m(GR) dB	standard $\dot{s}$(Z_c(PR) - Z_m(GR)) dB
Aug 13, 1998	-0.2	3.4
Aug 15, 1998	0.5	4.5
Feb 25A, 1999	-1.0	3.5
Feb 25B, 1999	0.9	1.7

6.5 Comparison of PR Algorithm Estimates with GR Observations

The PR algorithm assumes the power-law relationships *k*-Z and Z_c-R to determine the specific attenuation, *k*, for converting measured reflectivity, Z_m, to attenuation-corrected reflectivity, Z_c, and, subsequently, to determine the rain rate, R, from Z_c. The algorithm assumes two different RSD models corresponding to stratiform and convective rain for the initial values of the power-law coefficients. The coefficients are determined for each model for rain and snow at different temperatures and mixing ratios, freezing height level and storm top (Iguchi, et. al., 2000). During the attenuation correction process, the coefficients for *k*-Z are adjusted based on the attenuation estimate. In principle, the attenuation method is based on the surface reference method, which assumes that the apparent decrease in the surface cross-section, σ_o, is due to propagation loss caused by rain. The coefficient, α, in the *k*-Z relationship, $k = \alpha Z^{\beta}$, is adjusted such that the PIA estimated from the measured reflectivity profile will match the reduction in σ_o. In this case, it is presumed that difference in the PIA estimated from σ_o and the Z_m profile are due to varied choice of initial α values. This method works well when the radar is properly calibrated, and when the apparent decrease in σ_o is much larger than the fluctuation of the true surface return. However, when rainfall is light and attenuation is low the estimation of PIA is performed using precipitation echo alone via the Hitschfeld-Bordan (HB) method. Employing HB at low rain rates minimizes the error in PIA estimates due to the fluctuations in the surface cross-section associated with the surface reference method. Conversely, using the surface reference method at high rain rate avoids the divergence problem associated with HB (Iguchi, et. al., 2000).

Values of the coefficients in $R = a Z_c^b$ are determined in a way such that they are consistent with the coefficients (α,β) in the *k*-Z relationship. The relationship between the pairs (a,b) and (α,β) are determined using a quadratic function of the attenuation correction factor. (It is also noted here that the α-coefficient is further adjusted according to a non-uniform beam filling (NUBF) correction factor to compensate for non-uniform distribution of rain echo in the resolution volume.) (Iguchi, et. al., 2000) Thus, when the rain rate is high, and the attenuation is large, the surface reference method is used and the coefficients (a,b) are only weakly dependent on their initial values since Z_c is determined from the measured Z_m and estimates of the PIA near the surface. However, when rain rate is low, and attenuation is small, the appropriate selection of initial RSD parameters is essential since (a,b) are only slightly altered by the surface reference method. In practice a weighted average of the surface reference and HB methods are used to provide a smooth transition in the algorithm.

Comparison is made between Z_m(GR) and Z_c(PR) for each of the case studies. In addition to direct comparisons, the behavior of the reflectivity factor, Z, with the median volume drop diameter, Do, and the rain rate for GR and PR is also made. After resolution volume matching and alignment, scatter plots of Z_m(GR) vs. Z_c(PR) were constructed. These scatter plots are shown in figures 6.7(a-d) for each of the case studies, August 13 and 15, 1998 and February 25A and 25B, 1999, respectively. The scatter plots show relatively good agreement between ground radar reflectivity and PR attenuation-corrected reflectivity. The correlations for the case studies shown in figures 6.7(a-d) are 0.87, 0.82, 0.79 and 0.94, respectively. It should be noted that most of the scatter could be due to mis-alignment of the two data sets as well as from the measurement fluctuations.

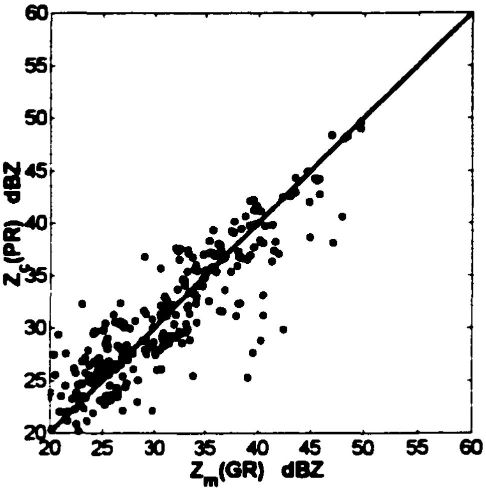

6.7(a)

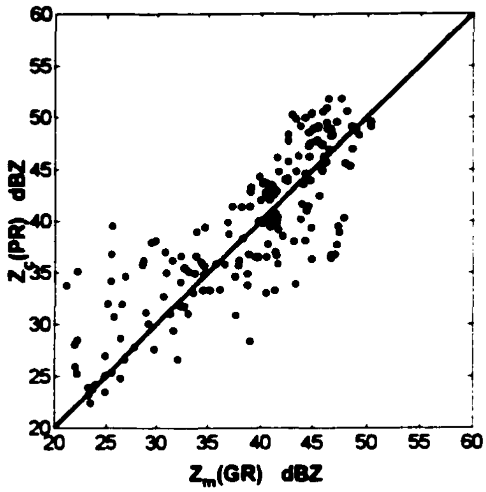

6.7(b)

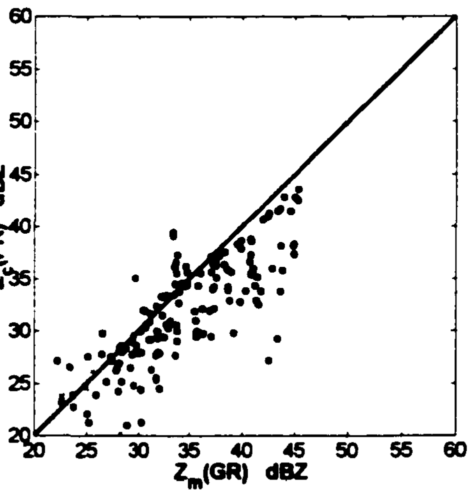

6.7(a)

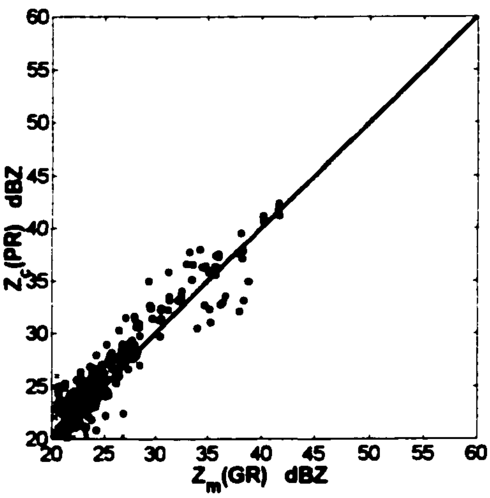

6.7(b)

Figure 6.7: Scatter plot of GR measured reflectivity, Z_m(GR), vs. PR attenuation-corrected, Z_c(PR), reflectivity: (a) TEFLUN-B, August 13, 1998, correlation is 0.87, (b) TEFLUN-B August 15, 1998, correlation is 0.82, (c) LBA, February 25A, 1999, correlation is 0.79 and (d) LBA, February 25B, 1999, correlation is 0.94.

Taking the ground radar measurements as the *truth* data, the functional relationships of $Z_m(GR)/N_w$ and $Z_c(PR)/N_w$ with D_o is constructed for each of the data sets. These relationships are shown in figure 6.8 for the August 13 data set for altitudes between 2 and 4 km. The black circles indicate the GR relationship. A curve of the form $\frac{Z_m(GR)}{N_w} = a\, D_o^b$ is fit to the GR data, which is indicated by the solid line. The PR relationship is depicted by the open squares, and the dashed line shows the curve fit for PR data with coefficients (a_p, b_p). For the relationship with GR data, the coefficients of the fit cure were found to be ($a_g = 0.088$ and $b_g = 7.607$). For PR data, the coefficients are ($a_p = 0.104$, $b_p = 6.975$). The purpose of this comparison is to see the applicability of the PR attenuation-corrected reflectivity to areas beyond the Z-R relationships. For first order approximation, the GR and PR based measurements behave similarly across the range of RSD's. However, a closer examination shows that for small D_o, the normalized PR attenuation-corrected reflectivity slightly under-estimates the drop size compared to $Z_m(GR)/N_w$. At $D_o = 1.29$ mm, the PR begins to over-estimate the drop size.

Similar comparisons are made for the TEFLUN-B August 15 and LBA February 25A and 25B data sets. The functional behavior of $Z_m(GR)$ and $Z_c(PR)$ with D_o for each of these data sets are shown in figures 6.9, 6.10 and 6.11, respectively. In each of these figures, a curve is fit to the data with the solid line indicating the fit to GR data and the dashed line indicating the fit to PR data. The coefficients for the fitted curves for each case are as follows: August 15, GR ($a_g = 0.234$, $b_g = 7.487$) and PR ($a_p = 0.512$, $b_p = 6.547$); February 25A, GR ($a_g = 0.073$, $b_g = 7.671$) and PR ($a_p = 0.110$, $b_p = 6.407$); and, February 25B, GR ($a_g = 0.053$, $b_g = 7.526$) and PR ($a_p = 0.064$, $b_p = 7.390$). The cross-over of the Z/N_w vs. D_o relationships between GR and PR is a manifestation of using a

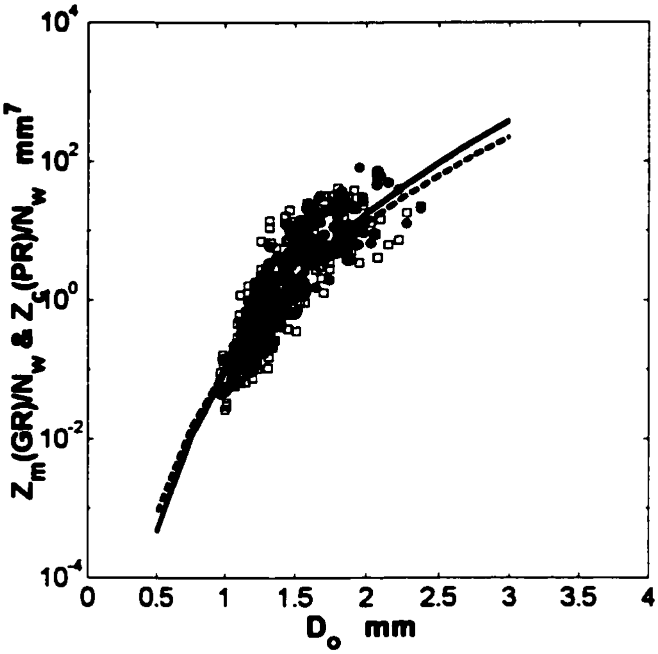

Figure 6.8: August 13, 1998. Scatter plot of $Z_m(GR)/N_w$ and $Z_c(PR)/N_w$ with D_o. GR data indicated by black circles and fit curve by solid line. PR data indicated by open squares and fit curve by dashed line.

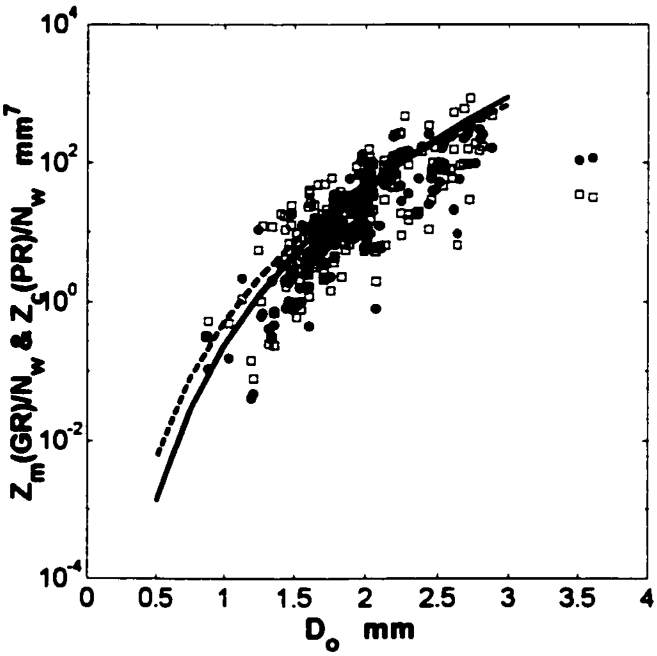

Figure 6.9: August 15, 1998. Scatter plot of $Z_m(GR)/N_w$ and $Z_c(PR)/N_w$ with D_o. GR data indicated by black circles and fit curve by solid line. PR data indicated by open squares and fit curve by dashed line.

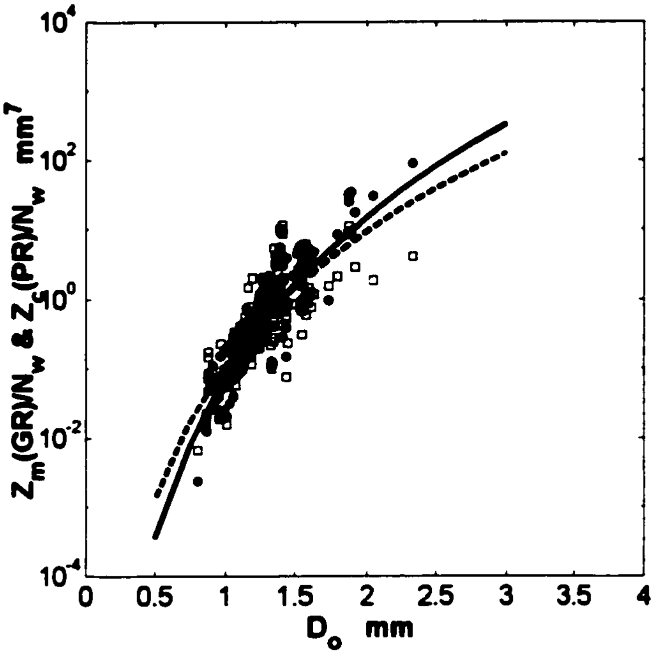

Figure 6.10: February 25A, 1999. Scatter plot of $Z_m(GR)/N_w$ and $Z_c(PR)/N_w$ with D_o. GR data indicated by black circles and fit curve by solid line. PR data indicated by open squares and fit curve by dashed line.

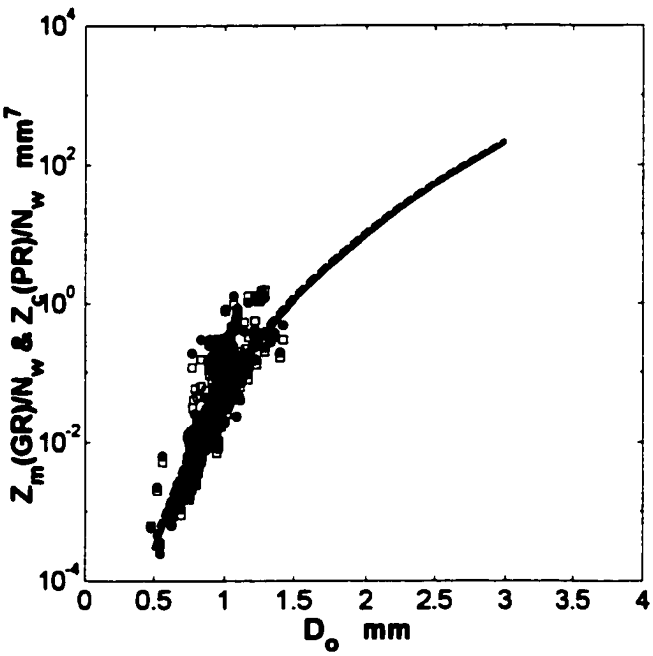

Figure 6.11: February 25B, 1999. Scatter plot of $Z_m(GR)/N_w$ and $Z_c(PR)/N_w$ with D_o. GR data indicated by black circles and fit curve by solid line. PR data indicated by open squares and fit curve by dashed line.

single "α" to the full vertical distribution of DSD along the beam, as opposed to tracking the variability with the RSD. Nevertheless, the closeness in the relationship between Z/N_w and D_o shows how good the attenuation correction procedure is through rain. The coefficients (a_g,b_g) and (a_p,b_p) for the fitted curves for each of the data sets is summarized in Table 6.3.

Table 6.3: Summary of coefficients to the fitted curves with form $\frac{Z}{N_w} = a D_o^b$ for the plots of D_o vs. Z/N_w for GR and PR data. The subscripts "g" and "p" in the table indicate GR and PR data sets, respectively.

	GR		PR	
	a_g	b_g	a_p	b_p
Aug 13, 1998	0.088	7.607	0.104	6.975
Aug 15, 1998	0.234	7.487	0.512	6.547
Feb 25A, 1999	0.073	7.671	0.110	6.407
Feb 25B, 1999	0.053	7.526	0.064	7.390

Next, a comparison of rain rate estimates from GR measurements is made with the PR algorithm. The rain rate for GR was determined from a Z-R relationship when rain rate was less than 10 mm hr^{-1} ($R = 0.017\ Z^{0.714}$), and a relationship using Z, Z_{dr} and β (see Bringi, et. al., 2002) when rain rate was greater than this. Ground radar estimate of the rain rate, R(GR), between 2 and 4 km altitude vs. the PR rain rate estimate, R(PR), for August 13 is shown in figure 12(a). For this data set, the mean bias, defined to be the ratio of the sum of the values of R(PR) to R(GR) (i.e., $\sum R(PR)/\sum R(GR)$), is 0.993, and the mean absolute deviation of the difference between R(GR) and R(PR) was found to be 45%.

A log-log plot of R/N_w vs. Z/N_w can be used to determine the relationship between rain rate and reflectivity factor. Normalization of the reflectivity factor and rain rate by N_w results in a straight line in the log-log plot with constant slope (denoted c_g and c_p for GR and PR data, respectively) and intercept (denoted d_g and d_p for GR and PR data, respectively) that are nearly independent of μ (Bringi and Chandrasekar, 2001). It is also noted that the PR algorithm sets μ to a constant at $\mu = 3$ (Iguchi, et. al., 2000). When Z and R are normalized in this way, the Z-R relationship can be written as (Testud, et. al. 2000; Bringi and Chandrasekar, 2001)

$$\frac{Z}{N_w} = a\left(\frac{R}{N_w}\right)^b \tag{6.11}$$

Thus, the variability in the multiplicative factor in the Z-R relationship is related to N_w. Using equation (6.11), the normalized Z-R relationships for GR and PR data become

$$\frac{Z_m(GR)}{N_w} = 10^{d_g}\left(\frac{R(GR)}{N_{wg}}\right)^{c_g} \tag{6.12}$$

for ground radar observations, and

$$\frac{Z_c(PR)}{N_w} = 10^{d_p}\left(\frac{R(PR)}{N_{wp}}\right)^{c_p} \tag{6.13}$$

for PR attenuation-corrected observations, where, N_{wg} and N_{wp} are the normalized intercepts using GR and PR data, respectively. The normalized intercept, N_{wg}, is derived from GR measurements and, $N_{wp} = N_{wg} + \varepsilon_n$, where ε_n is the value by which N_{wp} must be adjusted so that $Z_m(GR)/N_w = Z_c(PR)/N_w$. The combination of "α" adjustment method and the corresponding rainfall algorithm produces an equivalent N_w assumption for the PR algorithm. An equivalent microphysical interpretation for the variability in Z/N_w versus R/N_w from GR and PR can be made in terms of the N_w variability associated with PR retrieval. Equations (6.12) and (6.13) can be combined (and using $N_{wp} = N_{wg} + \varepsilon_n$) to obtain

$$R(PR)^{c_p} = 10^{(d_g - d_p)} (N_{wg})^{-c_g} (N_{wg} + \varepsilon_n)^{c_p} R(GR)^{c_g} \tag{6.14}$$

which can be re-written as

$$R(PR)^{c_p} = 10^{(d_g - d_p)} (N_{wg})^{c_p - c_g} \left(1 + \frac{\varepsilon_n}{N_{wg}}\right)^{c_p} R(GR)^{c_g} \tag{6.15}$$

Figure 6.12(b) shows the log-log plot of $R(GR)/N_w$ vs. $Z_m(GR)/N_w$ and $Z_c(PR)/N_w$ for the August 13 data. From this figure, the curve fit to the GR data has slope $c_g = 1.352$ (mm^6 m^{-3})/(mm hr^{-1}) and intercept $d_g = 2.800$ (mm^6 m^{-3})/(mm^{-1} m^{-3}). The curve fit to PR data has slope $c_p = 1.382$ and intercept $d_p = 2.533$. The percent difference in GR slope and PR slope with respect to GR is negligible (about 2%). Whereas, the percent difference in intercept is about 10%. Since the percentage difference between c_g and c_p is relatively small it is assumed that $c_g \approx c_p$ and equation (6.15) reduces to

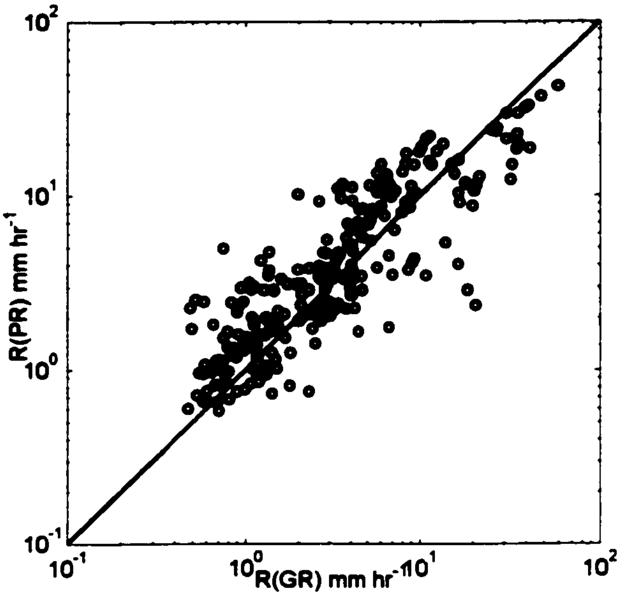

6.12(a)

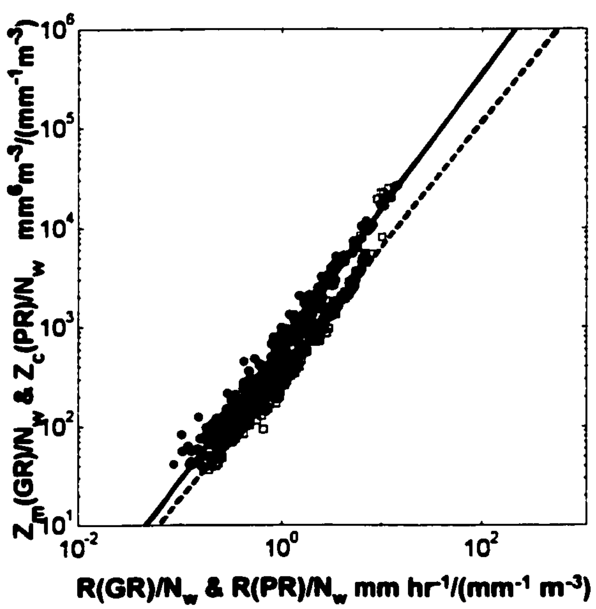

6.12(b)

Figure 6.12: August 13, 1998. (a) Scatter plot of GR rain rate, R(GR), to PR rain rate, R(PR) with statistics: $\sum R(PR)/\sum R(GR) = 0.993$, $\sum |R(GR) - R(PR)|/\sum R(GR) = 0.45$. (b) Scatter plot of R(PR) and R(GR) vs. Zm(GR).Nw and Zc(PR)/Nw, respectively. Black circles indicate GR data with fit curve shown by solid line. PR data indicated by open squares with fit curve shown as dashed line.

$$R(PR)^{c_p} = 10^{(d_g - d_p)}\left(1 + \frac{\varepsilon_n}{N_{wg}}\right)^{c_p} R(GR)^{c_p}. \tag{6.16}$$

From which it follows that

$$10^{(d_g - d_p)}\left(1 + \frac{\varepsilon_n}{N_{wg}}\right)^{c_p} = \left[\frac{R(PR)}{R(GR)}\right]^{c_p}. \tag{6.17}$$

Taking the logarithm of both sides of equation (6.17) yields

$$c_p \log\left(1 + \frac{\varepsilon_n}{Nwg}\right) = c_p \log\left(\frac{R(PR)}{R(GR)}\right) + (d_p - d_g). \tag{6.18}$$

Next, dividing both sides of equation (6.18) by c_p and taking the anti-logarithm of both sides of the equation results in

$$1 + \frac{\varepsilon_n}{Nwg} = \frac{R(PR)}{R(GR)} 10^{(d_p - d_g / c_p)} \tag{6.19}$$

from which ε_n can be determined as

$$\varepsilon_n = \left[10^{(d_p - d_g / c_p)} \frac{R(PR)}{R(GR)} - 1\right] N_{wg} \tag{6.20}$$

The difference in Z/N_w vs. R/N_w plots can be interpreted as an equivalent difference in N_w estimates implicitly used in the PR rainfall algorithm. For the August 13 data set (using the values for d_g d_p and c_p) ε_n can be obtained as (-0.364) N_{wg}. This result indicates that N_{wp} is about 36.4% larger than the estimate derived from GR measurements, or that N_{wp} is over-estimated by PR with respect to GR. Bolen and Chandrasekar (2000) concluded that there was a 3.8% under-estimate in PR rain rate estimate due to the reflectivity sensitivity of PR. The cases considered here were all over land and some of the under-estimate of PR with respect to GR can be attributed to under-correction of reflectivity in PR.

Similar to the plots for the August 13, 1998 data set shown in figures 6.12(a) and (b), plots of R(GR) vs. R(PR) and R/N_w vs. Z/N_w were constructed for the August 15, 1998, and the February 25A and February 25B, 1999 case studies. These plots are shown in the (a) and (b) panels in figures 6.13, 6.14 and 6.15 for each of the case studies, respectively. For each of these data sets, the mean bias (as previously defined) was found to be 0.993, 0.870, 0.764 and 1.220 for August 13, August 15, February 25A and February 25B, respectively, yielding no bias for the average. Also, the mean absolute deviation of the difference between R(GR) and R(PR) was found to be 45%, 40%, 48% and 37% for each case, respectively. For the plots of R/N_w vs. Z/N_w, the (slope, intercept) pairs for the Z/N_w - R/N_w relationship for August 15 are (c_g = 1.249, d_g = 2.859) and (c_p = 1.265, d_p = 2.567) for GR and PR, respectively. The percentage difference between d_g and d_p is about 8% on average. The resulting estimate in N_{wp}, using the indirect procedure developed here, indicates that it is 48.9% over-estimated compared to N_{wg} (i.e., ε_n/N_{wg} = -0.489). Similarly, for the February 25A case study, the percent difference between the intercepts is 6.85%. In this case, N_{wp} over-estimates N_{wg} by 44.7%. The February 25B case study has a 4.19% difference between the intercepts, with N_{wp} under-estimated by 15.9%. The slopes, intercepts, percent differences and 100 ε_n/N_{wg} for each of the case studies are summarized in Table 6.4.

The statistics of the rainfall comparison for the four carefully analyzed case studies can be considered very good. The average error of 42% is close to the theoretical average standard error of a Z-R relation (Chandrasekar, et. al., 2001). It should be noted here that this standard error is a combination of the error in rainfall estimate from both PR and GR, as well as the alignment error between them. While it is difficult to know precisely the standard deviation for each estimate, approximations can be made. The standard error in the estimate of rainfall from GR (using the algorithm presented) can be approximated to 15 – 30% depending on the rain rate (Bringi and Chandrasekar, 200). The error in the comparison between GR and PR, due to various alignment issues, was estimated by (Bolen and Chandrasekar, 2002c) to be about 25%, resulting in a residual standard error of 21%. While the above numbers are rough approximations, this provides a mechanism for making estimates of the standard error in the rainfall estimate from PR, based on data. Finally, the last issue is the bias between PR and GR measurements of rainfall. From the limited number of cases studied here, the mean bias between PR and GR rainfall estimates is negligible for all cases combined. However, for each case there was a bias. This is perhaps what should be expected: that is, the PR uses a common algorithm for all the longitudes with the objective of eliminating bias globally. The procedure for arriving at rainfall on a storm-by-storm basis will vary according to the regional distribution of the rainfall parameters, if a single parameter radar algorithm is used. Therefore, for individual storms, there may be a difference in measurements of rain between GR and PR while globally there may not be a bias.

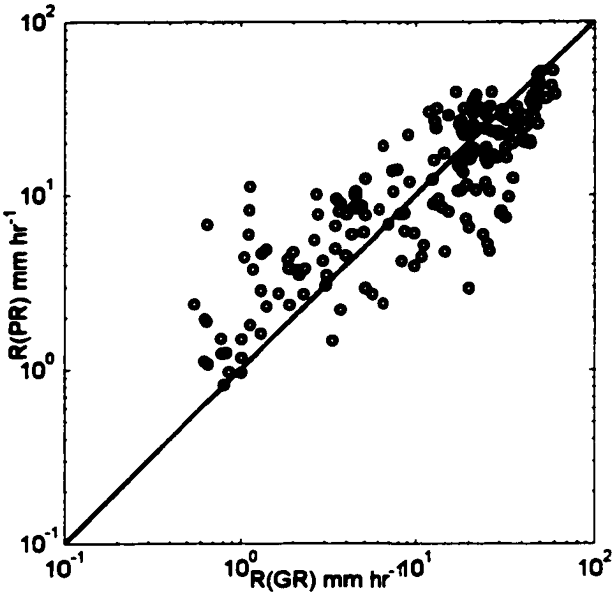

6.13(a)

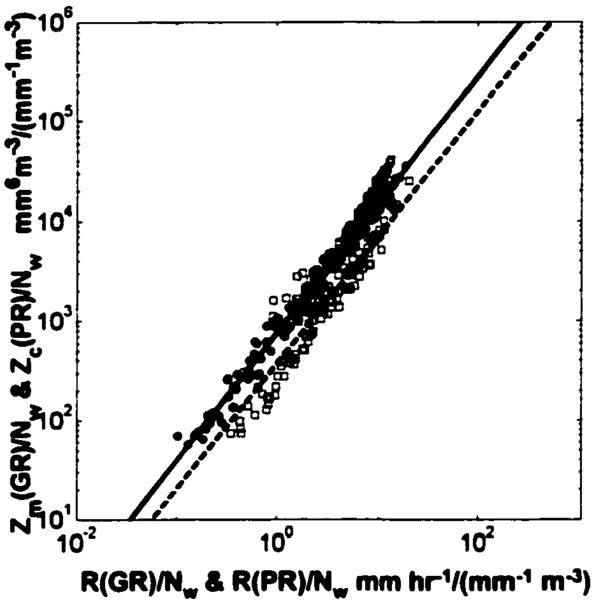

6.13(b)

Figure 6.13: August 15, 1998. (a) Scatter plot of GR rain rate, R(GR), to PR rain rate, R(PR) with statistics: $\sum R(PR)/\sum R(GR) = 0.870$, $\sum |R(GR) - R(PR)|/\sum R(GR) = 0.40$. (b) Scatter plot of R(PR) and R(GR) vs. Zm(GR).Nw and Zc(PR)/Nw, respectively. Black circles indicate GR data with fit curve shown by solid line. PR data indicated by open squares with fit curve shown as dashed line.

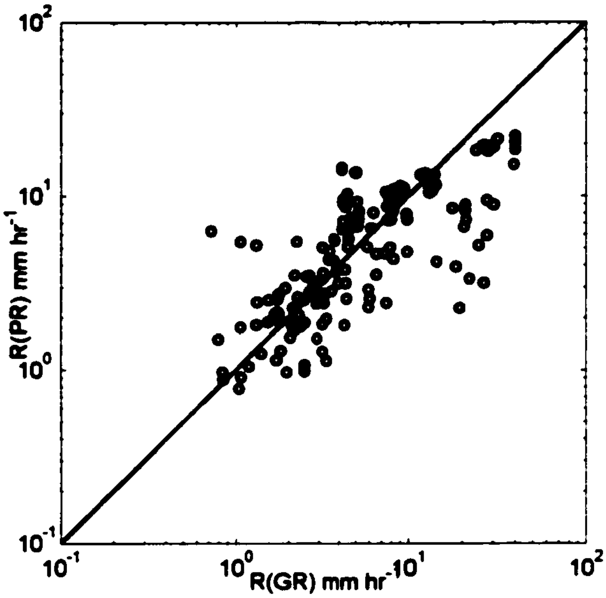

6.14(a)

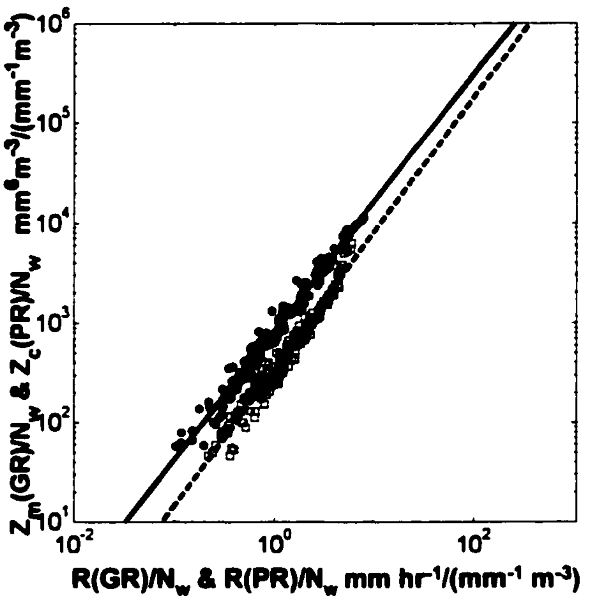

6.14(b)

Figure 6.14: February 25A, 1999. (a) Scatter plot of GR rain rate, R(GR), to PR rain rate, R(PR) with statistics: $\sum R(PR)/\sum R(GR) = 0.764$, $\sum |R(GR) - R(PR)|/\sum R(GR) = 0.48$. (b) Scatter plot of R(PR) and R(GR) vs. Zm(GR).Nw and Zc(PR)/Nw, respectively. Black circles indicate GR data with fit curve shown by solid line. PR data indicated by open squares with fit curve shown as dashed line.

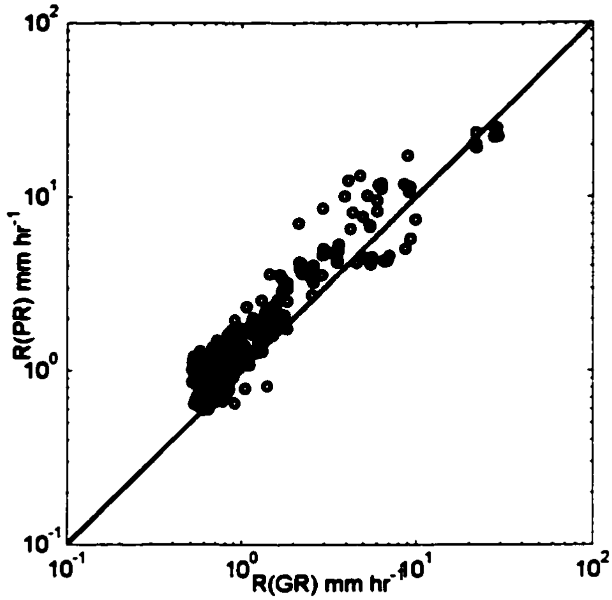

6.15(a)

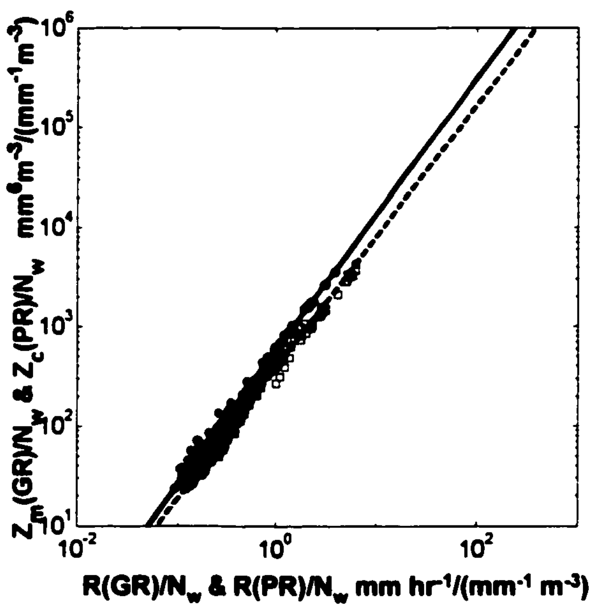

6.15(b)

Figure 6.15: February 25B, 1999. (a) Scatter plot of GR rain rate, R(GR), to PR rain rate, R(PR) with statistics: $\sum R(PR)/\sum R(GR) = 1.220$, $\sum |R(GR) - R(PR)|/\sum R(GR) = 0.37$. (b) Scatter plot of R(PR) and R(GR) vs. $Z_m(GR).N_w$ and $Z_c(PR)/N_w$, respectively. Black circles indicate GR data with fit curve shown by solid line. PR data indicated by open squares with fit curve shown as dashed line.

Table 6.4: Summary of coefficients to the fitted curves of the form $\left(\frac{Z}{N_W}\right) = c\left(\frac{R}{N_W}\right) + d$, percent difference in coefficients relative to GR, and the estimate of PR $\hat{N}_W$ (as a percentage of N_w) for the plots of $\frac{Z}{N_W}$ vs. $\frac{R}{N_W}$ for GR and PR data. The subscripts "g" and "p" indicate GR and PR data sets, respectively.

	GR		PR		comparison of coefficients		
	c_g	d_g	c_p	d_p	$100(c_g-c_p)/c_g$	$100(d_g-d_p)/d_g$	$100(\varepsilon_n/N_w)$
Aug 13, 1998	1.352	2.800	1.382	2.533	-2.23	9.55	-36.4
Aug 15, 1998	1.249	2.859	1.265	2.567	-1.28	10.21	-48.9
Feb 25A, 1999	1.282	2.713	1.325	2.527	-3.38	6.85	-44.7
Feb 25B, 1999	1.343	2.701	1.319	2.588	1.79	4.19	15.9

6.6 Summary

The microphysical retrievals and comparisons presented in this research can be very useful in the microphysical interpretation of PR observations. Polarimetric ground radar observations made along the TRMM PR beam were used to determine the three parameters of a gamma raindrop size distribution (RSD) model along the beam in the rain layer. An example of the estimated RSD along an individual PR beam was presented and compared to GR measurements along the beam. From the limited data available, statistical analysis was performed using altitude-histogram charts where the frequency of occurrence of the model parameters was determined for each horizontal layer through the vertical profile of the storm cell. Data for the statistical analysis were taken from the TEFLUN-B and the TRMM-LBA experiments. Using the mean value for comparison purposes, the altitude-histogram charts for the three model parameters, for each of the case studies, indicates a fairly constant RSD along the vertical profile in the rain layer. Similar charts were also constructed for the difference between measured GR reflectivity (Z_m(GR)) and PR attenuation corrected reflectivity (Z_c(PR)) derived from the current PR attenuation correction algorithm. While there are no systematic bias in the differences between Z_m(GR) and Z_c(PR) there may some under-correction and over-correction on a beam-by-beam basis.

Functional relationships between the normalized reflectivity (Z/N_w) and D_o for PR and GR observations were made for each of the case studies. Again no gross systematic differences were found between GR reflectivity and PR attenuation-corrected measurements. Fluctuations about the mean difference, on a beam-by-beam basis, could be the result of the PR algorithm assumptions of the RSD parameters. Rain rate estimates from the PR algorithm and GR observations for each of the data sets was computed. The average mean bias for all the cases was found to be 0.97, which perhaps indicates that there is no systematic bias in the observation of rain rate between the two systems (based on this limited number of data sets). It was also found that the average fractional standard error of the difference in rain rate estimates is about 42% for all of the cases, which is well within the expected standard errors of comparison for PR and GR based on rainfall estimates. Finally, plots of the normalized reflectivity factor for PR and GR (i.e., Z/N_w) as a function of normalized rain rate (i.e., R/N_w) from the PR algorithm, and that derived from ground radar observations, was also constructed. These were used to make an inference on the equivalent N_w derived form PR thereby developing a microphysical interpretation of the differences. These differences result in different rainfall estimates on a storm-by-storm basis, though on average there may not be any bias.

Chapter 7

SUMMARY AND SUGGESTS FOR FUTURE WORK

7.1 Summary

The principle objective of the research was the inter-comparison of attenuating, short wavelength spaceborne radar measurements with terrestrial-based polarimetric radar observations for the interpretation and calibration of space radar algorithms. Precise measurements between the two systems have been made on a point-by-point basis. This is important for calibration purposes, and for cross-validating retrieval and parameter estimation algorithms used to determine the rain rate from spaceborne platforms. The research includes: the development of a method to align observations from both space and ground-based instruments which takes into account differences in resolution volume size and orientation, differences in operating frequencies, and relative geometric distortion between them. The method, presented in Chapter 3, is validated using *in-situ* data collected during the TRMM field campaigns and can be used to precisely align data between a fixed and moving system.

Estimation of the total two-way path-integrated attenuation (PIA) on high-frequency spaceborne signals was presented in Chapter 4 using TRMM PR and SPOL data. The log-average PIA was found to be on the order of 5 dB, and calibration between the two systems was found to be within the measurement uncertainty of the instruments.

The sensitivity of the PR receiver for measuring meteorological events was also assessed. It was found that large portions of the areal extent of the storm cell was not detected by the PR relative to ground observations. However, though the percent of "missing" echo return was high it was shown that most were of low-intensity and did not contribute significantly to the rain rate estimation.

In Chapter 5, a method was developed to independently determine the PIA on PR measurements using ground-based polarimetric observations. The method used theoretical modeling of the relationships between K_u-band specific attenuation and S-band measurements of reflectivity and specific differential phase of the precipitating medium for ten different hydrometeor types. Ground-based observations were made along the PR beam and the PIA was determined from the measurements and the theoretical relationships for the hydrometeors encountered along the beam. Inter-comparison of this method with the single-frequency algorithm currently being used by the TRMM PR for attenuation correction showed no gross systematic bias in the PR algorithm. Finally, in Chapter 6, the raindrop size distribution (RSD) was determined along the PR beam from ground-based polarimetric observations. A statistical analysis of the RSD in the rain layer was performed using altitude-histogram charts. From these charts it was seen that the RSD is fairly constant below the freezing level through the vertical profile. A comparison of the histogram charts with the PR attenuation correction algorithm was presented. Results from this analysis correlated well with comparison of GR and PR rain rate estimates. From the analysis, it was found that the PR tends to over-estimate when rain rate is light compared to GR rain rate, and over-estimated the rain rate during light rain.

7.2 Suggestions for Future Work and Applications

The ultimate goal of the research should be toward the advancement of retrieval, and parameter estimation, algorithms to improve the quality of rainfall rate estimation near the earth surface. A methodology has been presented to precisely align radar observations from fixed-base and moving platform radar systems. Although, the method was used to produce coincident data sets between ground and space-based systems in the dissertation the procedure can also be applied to alignment between ground and airborne systems. It can also be applied to two ground-based instruments as well, such as between the CSU CHILL multi-parameter radar and S-POL radar. Useful, and significant, investigations of the polarimetric observations made by the CHILL (or, other system) can be made along air profiler beam (be it ground-based, or airborne). These observations can be used to estimate the PIA based on the method in Chapter 5, or to estimate the RSD, as per the analysis performed in Chapter 6, so as to make comparisons of the terminal velocity of raindrops in the rain medium with radar derived PIA and RSD estimations, thereby validating parameter estimation algorithms and rain rate retrieval techniques. The PIA estimates based on the method of Chapter 5, using K_u- and S-band radars, can also be extended to the relationships between other frequencies for both use on both real data and to predict PIA on future missions. For instance, the Global Precipitation Measuring (GPM) project, currently planned to follow the Tropical Rainfall Measuring Mission (TRMM), will operate at 35 GHZ. Analysis can be derived *a priori* of the attenuating effects of the precipitation medium on signal degradation of the GPM echo, thereby refining the retrieval and parameter estimation algorithms planned for this mission.

In addition to meteorological analysis, this work can also be extended to communications systems. Strategic roadmaps for NASA's Human Exploration and Development of Space (HEDS) enterprise support near-term high-frequency communication systems that provide moderate to high data rates with dependable, robust service. Near-earth and human planetary exploration will baseline K_a-Band, but may ultimately require the use of even higher frequencies. Increased commercial demand on low-frequency earth-space bands have also led to increased interest in the use of higher frequencies in regions like K_u and K_a-Band, as well. Operationally, attenuation estimates of the precipitating medium can be used to adjust optimum power levels on earth-space communications links. Open loop estimation of signal degradation can be performed via a network of ground-based polarimetric radars. Furthermore, such a network can also be used in site-diversity schemes for commercial spot-beam satellite systems, such as those used in the cellular mobile industry. Maps of specific attenuation estimates derived from the methods developed in the dissertation can be used near ground sites to determine link quality due to precipitation signal degradation. Scheduled links can be dynamically routed based on the attenuation maps. Impact of the precipitating medium on high rate data signals used for International Space Station (ISS) or Space Shuttle Orbiter (SSO) programs to downlinks to Marshall or Johnson Space Flight Centers can also be made. Signal attenuation on proposed projects like the K_u-band high definition television (HDTV) link can be made *a priori* to signal transmission. Quality assessment can also be made on direct data link distribution from low earth orbit (LEO) satellites supporting HEDS or other NASA enterprises such as high data rate meteorological science missions in the Earth Science Enterprise (ESE).

Appendix A

GENERAL DESCRIPTION OF PR SCAN GEOMETRY AND DATA PRODUCTS

A.1 Precipitation Radar (PR) scan geometry

The scan geometry of the TRMM Precipitation Radar (PR) is represented in Figure A.1. Each scan contains 49 angle bins (or, rays) sampled over an angular arc of 34 degrees. The PR begins recording data along each ray starting from a fixed distance from the satellite, which is different for each ray. The exact value of the starting distance is written in the 1B21 and 1C21 files and is given in the data set "Ray Header" under the column labeled "startBinDist." For the satellite in a nominal altitude of 350 km, sampling begins at about 23 km above mean sea level (msl) and extends along the ray. For the two rays at the scan edge (i.e., farthest from nadir), the distance is 33.5 km, monotonically decreasing to 30.25 km for the two rays adjacent to nadir. At nadir, the distance is 34.75 km. The extra data is known as the "mirror" because reflected energy is recorded from ground to target to ground. In the "normal sample" data set, samples are recorded every 250 meters along the ray. Data from each scan is, therefore, contained in a matrix that is 49 (rays) x 140 (range bins) in size. Each scan is taken about 0.6 seconds apart, and the number of seconds recorded in each file is nominally 5,490 (about the length of one period of the satellite). The size of each normal sample is then 49x140x9150 (TRMM Science User Interface Control Specifications, release4.04, 1999.

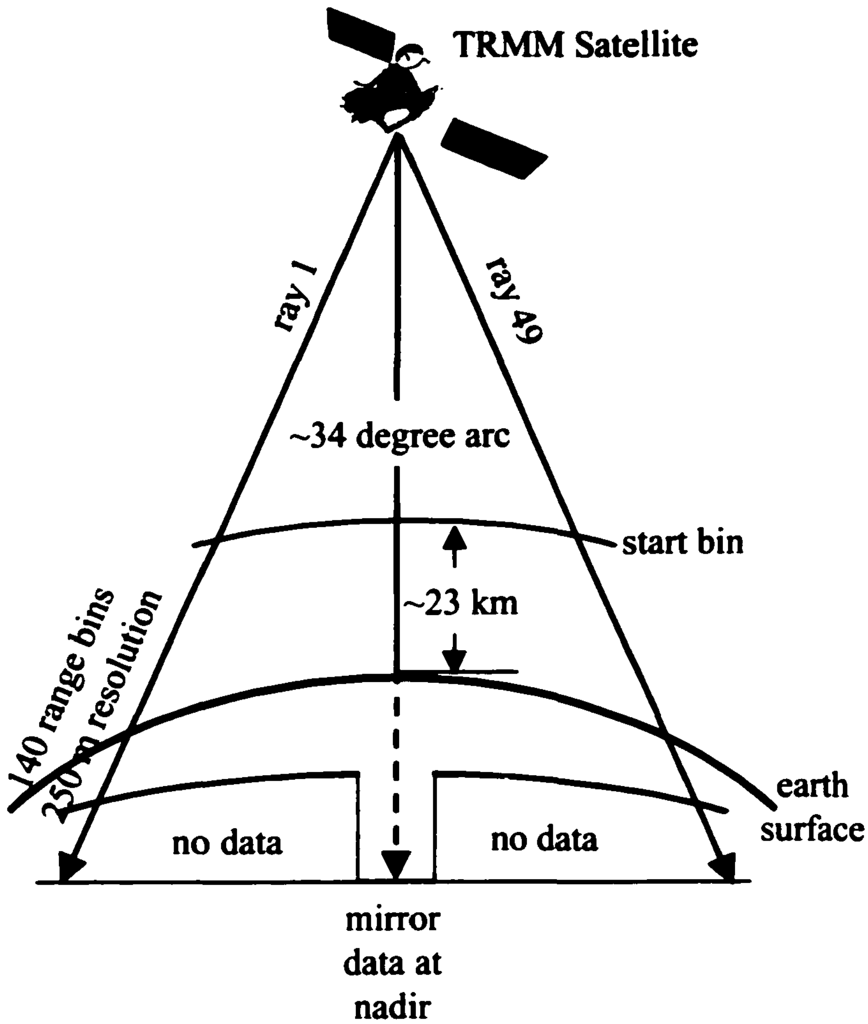

Figure A.1: Representation of PR scan geometry (not drawn to scale). The PR scans across a 34 degree arc starting at about 23 km above msl a the nadir. Each scan is 40 (rays) x 140 (range bins) in size. The mirror data is taken along the nadir ray (number 25).

An exception to this size rule is the PR data corrected for attenuation, derived form the PR algorithm, which are stored in a 49x80x9150 matrix. The range bin is truncated to 80 in this data set, which is the range bin near the earth surface. Since, in the normal sample, the surface can vary, a conversion is needed to relate PR corrected data to the normal sample data. This conversion is (Iguchi, 1999)

$$Z_c(\text{index}) = \text{round}(\text{range bin} - \text{rbellip} + 80) \quad \text{(A.1)}$$

where, Z_c(index) is the corrected index for the measurement, Z_c(PR), range bin is the bin number of the uncorrected index for Z_c(PR) and rbellip = 0.5(binEllipsoid – rayStart) + 1 (with binEllipsoid being the range bin of the earth ellipsoid found in the data file, and rayStart being the starting bin number of the ray found in the RayHeader).

A.2 PR data products

The standard TRMM PR data products are classified into three levels: Level 1 and Level 2 products are data that is processed within the PR instantaneous field of view (IFOV). Level 3 data products are statistics accumulated over monthly measurements in a $5^{\circ} \times 5^{\circ}$ grid. Only Level 1 and 2 data products are used in the dissertation, which are summarized in Table A1 (TRMM PR Algorithm Instruction Manual, version 2.0, 2000).

Table A.1: Summary of PR data products used in the dissertation.

Number/Name	Products	Algorithm Description
1B21: PR Power	received power, and system noise level	converts count value of radar echoes and noise level into engineering values
1C21: PR Reflectivities	profiled reflectivity factor (Z)	converts power and noise values into reflectivity factors
2A23: PR Qualitative	freezing level altitude	detects freezing level and bright band
2A25: PR Profile	attenuation corrected Z-profile	attenuation derived from hybrid of surface reference method and Hitschfeld-Bordan

Appendix B

SUMMARY OF OPERATIONAL CHARACTERISTICS OF SPOL AND TRMM PR RADARS

B.1 SPOL and TRMM PR operational characteristics

Table B.1: Data collection characteristics of the SPOL radar during the TEFLUN-B and TRMM-LBA field campaigns.

Case Study	Date	Time (UTC)		Elevation limits (deg)	Azimuth limits (deg)	SPOL distance (km)
		start	stop			
MELB980813	13-Aug-98	22:25:19	22:30:44	1.0 - 24.0	320 - 40	38
MELB980815	15-Aug-98	21:39:56	21:41:16	1.0 - 7.0	310 - 10	104
BRZL990225A	25-Feb-99	20:10:31	20:15:15	180.0 - 320.0	1.5 - 14.3	79
BRZL990225B	25-Feb-99	20:10:31	20:15:15	180.0 - 320.0	1.5 - 14.3	75

Table B.2: Overflight characteristics of the TRMM PR radar during the TEFLUN-B and TRMM-LBA field campaigns.

Case Study	Date	Time (UTC)		Orbit No.	Scan No.		TRMM distance (km)
		start	stop		start	stop	
MELB980813	13-Aug-98	22:25:19	22:30:44	4085	4371	5470	65
MELB980815	15-Aug-98	21:40:35	21:41:34	4116	5435	5534	80
BRZL990225A	25-Feb-99	20:12:01	20:13:01	7174	7174	7320	35
BRZL990225B	25-Feb-99	20:10:31	20:15:15	7174	7174	7320	30

B.2 Wide area maps of PR reflectivity over meteorological regions of interest

PR reflectivity maps containing 100 scans (1 minute) of PR overpass data are shown in Figure B.1. PR data is sampled at 4 km horizontal resolution, at 2 km CAPPI, in PR centered coordinate system (i.e., the PR scan line is perpendicular to the x-axis after resampling). Shown in the figure are the TRMM satellite ground track (circles), PR scan line (dotted), ground radar location (diamond) and the storm cells that were used. The reflectivity map for the TEFLUN-B, August 13 and 15, 1998 cases and the TRMM-LBA, February 25A and 25B cases are shown in the (a), (b) and (c) panels, respectively.

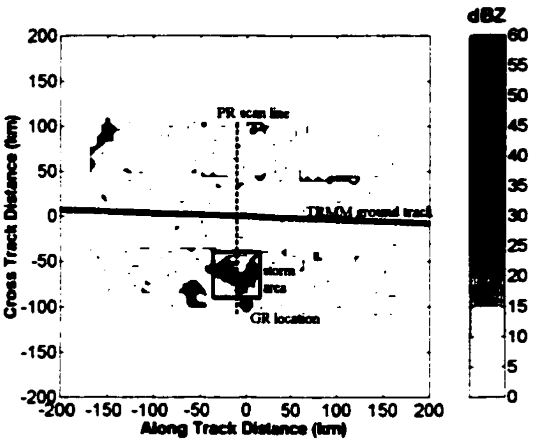

B.1(a)

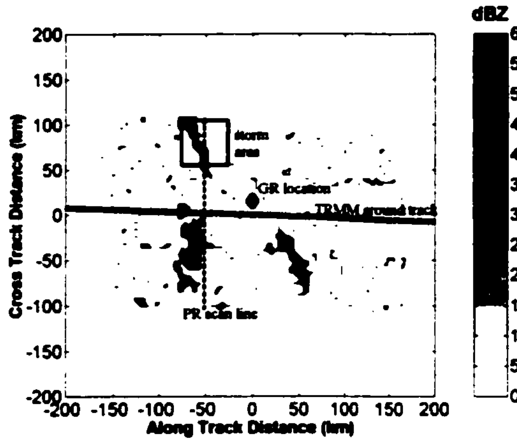

B.1 (b)

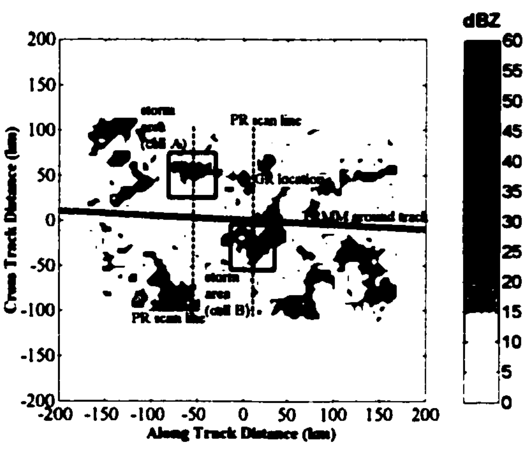

B.1(c)

Figure B.1: PR reflectivity in PR coordinate system, at 4 km horizontal resolution at 2 km CAPPI. (a) August 13, 1998, (b) August 15, 1998, (c) February 25A and 25B, 1999 (labeled accordingly).

Bibliography

1. Amayenc, P.and Marzoug, M., 1992: A survey of algorithms studies developed at CRPE for range profiling of rain rate from a spaceborne radar, Proc. Int. Workshop on the Processing and Utilization of the Rainfall Data Measured from Space, Tokyo, Japan, Communications Research Laboratory, pp 289-294.

2. Anagnostou, E., Morales, C. and Dinku, T., 2001 : The use of TRMM Precipitation Radar observations in determining ground radar calibration biases, *J. Atmos. and Oceanic Tech.*, **18**, 616-628.

3. Atlas, D., 1947: Preliminary report on new techniques in quantitative radar analysis of rainstorms, *Rep. ANMW 7-4, part I*, Air Material Command, Wright-Patterson AFB, Dayton, Ohio.

4. Atlas, D., 1948: Some experimental results of quantitative radar analysis of rainstorms , *Rep. ANMW 7-4, part II*, Air Material Command, Wright-Patterson AFB, Dayton, OH.

5. Austin, P. M. and Williams, E. L., 1951: Comparison of radar signal intensity with precipitation rain rate, Weather Res. *Tech. Rep. 14*, Dep. of Meteorol. Mass. Inst. of Technol., Cambridge, Mass.

6. Aydin, H., Direskeneli, H. and Seliga, T., 1987: "Dual Polarization Radar Estimation of Rainfall Parameters Compared with Ground-based Disdrometer Measurements: October 29, 1982 Central Illinois Experiment," *IEEE Trans. Geosci. Remote Sens.*, **GE-25**, pp 834-844.

7. Batan, L., J., 1973: *Radar Observables of the Atmosphere*, University of Chicago Presss, pp 324.

8. Beard, K. and Chuang, C., 1987: A New Model for the Equilibrium Shape of Raindrops," *J. Atmos. Sci.*, **56**, pp 2673-2683.

9. Beaver, J. and Bringi, V. N., 1997: The Application of S-band Polarimetric Radar Measurements for K_a-band Attenuation Prediction, *Proc. IEEE*, **85**, no. 6, June, pp 893-909.

10. Beheng, K., 1978: Numerical Simulation of Graupel Development, *J. Atm. Sci.*, **35**, pp 683-689.

11. Best, 1988: B.E.S.T. (Tropical System Energy Budget) - Scientific objectives and preliminary definition of a satellite mission dedicated to GEWEX and GLOBAL CHANGE, *Synthesis Document*, Toulose, France, pp 58.

12. Blanchard, D. C., 1953: Raindrop size distribution in Hawaiian rains, *J. Atmos. Sci.*, **10**, pp 457-473.

13. Bolen, S. and Chandrasekar, V., 2002a: "Methodology for Aligning and Comparing Spaceborne Radar and Ground-Based Radar Observations," *J. of Appl. Meteor.*

14. Bolen, S. and Chandrasekar, V., 2002b: "Quantitative Estimation of TRMM PR Signals Along PR Beam Path From Ground-Based Polarimetric Radar Observations," *Radio Science.*

15. Bolen, S. and Chandrasekar, V., 2002c: Methodology for Aligning and Comparing Spaceborne Radar and Ground-Based Radar Observations, *J. of Oceanic and Atmos. Sci.*, under review.

16. Bolen, S. M. and Chandrasekar, V., 2000a: Quantitative Cross Validation of Space-Based and Ground-Based Radar Observations, *J. Appl. Meteorol. Special Issue on TRMM*, **39**, pp 2071-2079.

17. Bolen, S. and Chandrasekar, V., 2000b: Ground and Satellite-Based Radar Observation Comparisons: Propagation of Space-Based Radar Signals," *IEEE IGARSS 2000 Conference*, Honolulu, Hawaii, July 24-28.

18. Bolen, S. and Chandrasekar, V., 1999: "Comparison of Satellite Based and Ground Based Radar Observations of Precipitation," *29th International Conference on Radar Meteorology*, Montreal, Canada, July 12-16.

19. Bolen, S., Chandrasekar, V., and Benjamin, A., 2001: Estimation of Spaceborne Radar Signals from Polarimetric Ground Radar Observations, " *30th International Conference on Radar Meteorology*, Munich, Germany, July 19-24, 2001.

20. Borgeaud, M. Shin, R. T. and Kong, J. A., 1987: Theoretical Models for Polarimetric Radar Clutter, *Electron. Waves and Applic.*, **1**, pp 73-89.

21. Brigni, V. N., Scarchilli, G., Chandrasekar, V., and Bringi, V., 2000: Measurement of Raindrop Shape from Polarimetric Radar Observations, *J. Atm. Sci.*, **57**, pp 3406-3413.

22. Bringi, V. N. and Chandrasekar, V., 2001: Polarimetric Doppler Weather Radar-Principles and Applications, *Cambridge University Press*, New York, NY.

23. Bringi, V. N., Chandrasekar, V., Balakrishnan, N. and D. S. Zrnic, D. S., 1990: An Examination of Propagation Effects in Rainfall on Radar Measurements at Microwave Frequencies, *J. of Atm. and Oceanic Tech.*, **7**, no. 6, pp 829-830.

24. Bringi, V. N., Knupp, K., Detwiler, A., Liu, L., Caylor, I and Black, R., 1997: Evolution of a Florida Thunderstorm during the Convection and Precipitation/Electrification Experiment: The Case of 9 August 1991, *Mthly Wthr Rev*, **125**, pp 2131-2160.

25. Bringi, V., Chandrasekar, V. and Xiao, R., 1998: "Raindrop Axis Ratios and Size Distributions in Florida Rainshafts: An Assessment of Mulitparameter Radar Algorithms," *IEEE Trans. Geosci., Remote Sens.*, **36**, pp 703-715.

26. Bringi, V., Huang, G., Chandrasekar, V. and Gorgucci, E., 2001: A Methodology for Estimating the Parameters of a Gamma Raindrop Size Distribution Model from Polarimetric Radar Data: Application to a Squall-Line Event from the TRMM/Brazil Campaign.

27. Brogan, W., 1985: *Modern Control Theory, Prentice Hall*, Inc., Englewood Cliffs, NJ.

28. Cataneo, R. E. and Stout, E. G., 1968: Raindrop-size distributions in humid continental climates, and associated rainfall rate - radar reflectivity relationships, *J. Appl. Meteorol.*, **7**, pp 901-907.

29. Cataneo, R. E., 1969: A method for estimating rainfall rate - radar reflectivity relationships, *J. Appl. Meteorol.*, **8**, pp 815-819.

30. Chandrasekar, V., Meneghini, R. and Zawadski, I., 2001: Global and Local Precipitation Measuremetns by Radar, *Atlas Symposium Monograph*, Amer. Meteor. Soc., 2001.

31. Chandrasekar, V. and Bringi, V. N., 1987: Simulation of Radar Reflectivity and Surface Measurements of Rainfall, J. Atm and Oceanic Tech., **4**, pp 464-478.

32. Chandrasekar, V., Cooper, W. and Bringi, V., 1988: "Axis Ratios and Oscillation of Raindrops," *J. Atmos Sci.*, **45**, pp 1325-1333.

33. Cheng, L. and English, M., A 1983: Relationship Between Hailstone Concentration and Size, **40**, *J. Atm. Sci.*, pp 204-213.

34. Cox, D. C., 1978: An overview of the Bell Laboratories 19 and 28 GHz COMSTAR beacon propagation experiments, *Bell Syst. Tech. J.*, **57**, no. 4, pp 1231-1240.

35. Davies, P. G., 1994: Summary of attenuation statistics from OPEX members, *Proc. OPEX 21*, Louvain.

36. Dennis. A. S., 1963a: Rainfall determinations by meteorological satellite radar, *NASA CR-50193*, Stanford Research Institute, Menlo Park, Calif.

37. Dennis, A. S., 1963b: Fundamental limitations on precipitation observations from satellites, *NASA CR-52848*, Stanford Research Institute, Menlo Park, Calif.

38. Doviak, R., Zrnic, D., 1995: Doppler Radar and Weather Observations, 2nd Ed. Academic Press, San Diego, CA, pp 271.

39. Durden, S. and Haddad, Z. S., 1998: Comparison of radar rainfall retrieval algorithms in convective rain during TOGA COARE, *J. Atmos. Oceanic Technol.*, **15**, pp 1091-1096.

40. Eckerman, J. and Wolf, E. A., 1975: Spaceborne meteorological radar measurements requirements meeting, *NASA X-900-75-198*, GSFC, Greenbelt, Maryland, **57**, pp 57, plus appendices.

41. Eckerman, J., 1975: Meteorological radar facility for the space shuttle, *IEEE National Telecomm. Conf., New Orleans, IEEE Publ. 75, CH1015 CSCBM* pp 37-6 to 37-17.

42. Fujita, M. 1983: An algorithm for estimating rain rate by dual-frequency radar, *Radio Sci.*, **18**, pp 697-708.

43. Fujita, M., Okamota, K., Masuko, M., Yoshikado, S. and Nakamura, K., 1985:Interferenceof rain rate profile and path-integrated rain rate by an airborne microwave rain scatterometer, *Radio Sci.*,**20**, pp 631-642.

44. Goldhirsh, J. and Walsh, E. J., 1982: Rain measurements from space using a modified seasat-type radar altimeter, *IEEE Trans. Antennas Propag.*, **30**, pp 726-732.

45. Goldhirsh, J., 1988: Analysis of algorithms for retrieval of rain rate profiles from a spaceborne dual-wavelength radar, *IEEE Trans. Geosci. Remote Sens.*, **26**, pp 98-114.

46. Gorgucci, E., Scarchilli, G., Chandrasekar, V., and Bringi, V., 2000: Spatial Distribution of Mean Raindrop Shape from Polarimetric Radar Observations, *13th Inter Conf. on Clouds & Precip., Proc.*, **1**, pp 361-363.

47. Gorgucci, E., Scarchilli, G., Chandraskar, V. and Bringi, V., 2001: "Estimation of Raindrop Size Distribution Parameters From Polarimetric Radar Measurements," submitted to *J. Atmos. Sci.* (under review).

48. Gorgucci, E., Scarchilli, G., Chandraskear, V. and Bringi, V., 2000: "Measurement of Mean Raindrop Shape from Polarimetric Radar Observations," *J. Atmos. Sci.*, **57**, pp 3406-3413.

49. Green, A., 1975: An Approximation for the Shapes of Large Rain-Drops," *J. Appl. Meteor.*, **14**, pp 1578-1583.

50. Herzegh, P. and A. R. Jameson, 1992: Observing precipitation through dual-polarization radar measurements. *Bull. Amer. Meteor. Soc.*, **73**(9), 1365-1374

51. Hitschfeld, W. and Bordan, J., 1954: Errors inherent in the radar measurement of rainfall at attenuating wavelengths, *J. Meteor*, **11**, pp 58-67.

52. Hubbert, J. and Bringi, V., 1995: An Iterative Technique for the Analysis of Copolar Differential Phase and Dual Frequency Radar, *J. Atm. and Oceanic Tech.*, **12**, no. 3, 643-648.

53. Iguchi, T. and Meneghini, R., 1994: Intercomparison of single-frequency methods for retrieving vertical profile from airborne or spaceborne radar data, *J. Atmos. Oceanic Technol.*, **11**, pp 1507-1516.

54. Iguchi, T., Kozu, T., Meneghini, R., Liao, L., and Okamoto, K., 2000: Rain profiling algorithm for the TRMM precipitation radar," *J. Appl. Meteor.*, vol. 39, pp. 2038-2052.

55. Im, E. and Kellogg, K., 1990: Spaceborne radar for rain and cloud measurements: A conceptual design, *Proc. IGARSS'90 Symp.*, College Park, Maryland, pp 425-428.

56. Im, E. and Li, F., 1989: Tropical rain mapping radar on the Space Station. *Proc. IGARSS'89 Symp.*, Vancouver, BC Canada, pp 1485-1490.

57. Jameson, A. 1985: Microphysical Interpretation of Multi-parameter Radar Measurements in Rain. Part III: Interpretation of Propagation Differential Phase Shift Between Orthogonal Linear Polarizations," *J. Atmos. Sci.*, **42**, pp 607-614.

58. Kozu, T. and Nakamura, K., 1991: Rainfall parameter estimation from dual radar measurements combining reflectivity profile and path-integrated attenuation, *J. Atmos. Oceanic Technol.*, **8**, pp 259-270.

59. Liu, H. and Chandrasekar, V., 2000: Classification of Hydrometeors Based on Polarimetric Radar Measurements: Development of Fuzzy Logic and Neuro-Fuzzy Systems, and In Situ Verification, *J. Atm. Oceanic Tech.*, **17**, pp 140-164.

60. Marecal, V., Tani, T., Amayenc, P., Klapisz, C., Obligis, E. and Vitard, N., 1997: Rain relations inferred from microphysical data in TOGA COARE and their use to test a rain-profiling method from radar measurements at Ku-band, *J. Appl. Meteor.*, **12**, pp 1629-1646.

61. Marshall, J. S. and Palmer, W. M. K., 1948: The distribution of raindrops with size, *J. Atmos. Sci.*, **5**, pp 165-166.

62. Marshall, J. S., Langille, R. C. and Palmer, W. M. K., 1947: Measurement of rainfall by radar, *J. Atmos. Sci.*, **4**, pp 186-192.

63. Marzoug, M. and Amayenc, P., 1991: Experimental tests of an improved single frequency algorithm for rain rate profiling using airborne radar data, *Proc. 25th Int. Conf. on Radar Meteorol.*, Paris, France, Am. Meteor. Soc., pp 396-399.

64. Marzoug, M. and Amayenc, P., 1992: A new class of dual-frequency algorithms for rain rate profiling from a spaceborne radar: Principle and tests, Proc. IGARSS'92, Houston, Texas, pp 1376-1379.

65. Marzoug, M. and Amayenc, P., 1993: Algorithms for range profiling of rain rate from a spaceborne radar: Overall validation using airborne radar data, *Proc. 26th Conf. on Radar Meteorol.*, Norman, Okla., Am. Meteorol. Soc., pp 690-693.

66. Marzoug, M. and Amayenc, P., 1994: A class of single- and dual-frequency algorithms for rain-rate profiling from a spaceborne radar. Part I: Principle and test from numerical simulations, *J. Atmos. Oceanic Technol.*, **11**, pp 1480-1506.

67. Marzoug, M., Amayenc, P., Testud, J. and Karouche, N., 1989: Conceptual design of the spaceborne rain radar of the B.E.S.T. project, *Proc. 24th Conf. on Radar Meteorol., Tallahassee, Fl, Amer. Meteorol. Soc.*, pp 597-600.

68. McCormick, G. C. and Hendry, A., 1975: Principles for the radar determination of the polarization properties of precipitation, *Radio Sci.*, **10**, pp 421-434.

69. Meneghini, R. and Nakamura, K., 1990: Range profiling of the rain rate by an airborne weather radar, *Remote Sens. Environ.*, **31**, pp 193-209.

70. Meneghini, R., Eckerman, J. and Atlas, D., 1983: Determination of rain rate from a spaceborne radar using measurements of total attenuation, *IEEE Trans. Geosci. Remote Sens.*, **21**, pp 34-43.

71. Meneghini, R., Nakamura, K., Ulbrich, C. W. and Atlas, D., 1989: Experimental test of methods for measurement of rainfall rate using and airborne dual-wavelength radar, *J. Atmos. Oceanic Technol.*, **6**, pp 637-651.

72. Meneghini, R., Kozu, T., Kumagai, H. and Boncyk, W. C., 1992: A study of rain estimation methods from space using dual-wavelength radar measurements at near-nadir incidence over ocean, *J. Atmos. Oceanic Technol.*, **9**, pp 364-382.

73. Meneghini, R. and Kozu, T., 1990: *Spaceborne Weather Radar*, Artech House, Inc., Norwood, Mass., 1-3, 26-27, 170-174.

74. Moore, R. K. and Xie, S. S., 1988: Radar rainfall measurements system using SAR and conical-scan methods, *Tropical Rainfall Measurements*, J. S. Theon and N. Fugono, Eds, A. Deepack Publishing, pp 243-253.

75. Okamato, K., Miyazaki, S. and Ishida, T., 1979: Remote Sensing of Precipitation by a Satelliteborne Microwave Remote Sensor, *Acta Astronautica*, **6**, pp 0143-1060.

76. Passarelli, R., 1978: Theoretical and Observational Study of Snow-Sized Spectra and Snowflake Aggregation Efficiencies, *J. Atm. Sci.*, **35**, pp 882-889.

77. Pruppacher, H. R. and Pitter, R., 1971: A Semi-Empirical Determination of the Shape of Cloud and Raindrops, *J. Atmos. Sci.*, **28**, 86-94.

78. Pruppacher, H. R., and Beard, K. V., 1970: A wind tunnel investigation of the internal circulation and shape of water drops falling at terminal velocity in air, *Q. J. R. Meteorol. Soc.*, **96**, pp 247-256.

79. Ryde, J. W., 1941: Echo intensities and attenuation due to clouds, rain, hail, sand and dust storms, Rep. 7831, *Rep. 7831*, General Electric Co., Wembley, England.

80. Ryde, J. W., 1946: The attenuation and radar echoes produced at centimeter wavelengths by various meteorological phenomena, *Meteorol. Factors in Radio Wave Prop.*, Physical Soc. of London, pp 169-188.

81. Sachidananda , M. and Zrnic, D., 1986: Differential Propagation Phase Shift and Rainfall Rate Estimation. *Radio Sci.* **21**, pp 235-247.

82. Sachidananda , M. and Zrnic, D., 1987: Rain Rate Estimates from Differential Polarization Measurements, *J. Atmos. Oceanic Tech.*, **4**, pp 588-598.

83. Sauvageot, H., 1992: Radar Meteorology, *Artech House, Inc*, Norwood, MA, 150, pp 167-170.

84. Schowendgerdt, R. A., 1997: Remote Sensing: Models and Methods for Image Processing , 2nd Ed., Academic Press, San Diego, Calif., pp 331-337.

85. Seliga, T. A. and Bringi, V. N., 1976: Potential use of radar differential reflectivity measurements at orthogonal polarization for measuring precipitation, *J. Appl. Meteorol.* **15**, pp 69-76.

86. Seliga, T. A. and Bringi, V. N., 1978: Differential reflectivity and differential phase shift: Applications in radar meteorology, *Radio Sci.*, **13**, pp 271-275.

87. Skolnik, M. I., 1974: The application of satellite radar for the detection of precipitation, *NRL Rep. 2896*, October, pp 100.

88. Testud, J., Amayenc, P. and Marzoug, M., 1992: Rainfall rate retrieval from a spaceborne radar: Comparison between single-frequency, dual-frequency, and dual-beam techniques, *J. Atmos. Oceanic Technol.*, **9** pp 599-623.

89. Testud, J., Oury, S., Amayenc, P. and Black, R., 2001: The Concept of "Normalized" Distributions to Describe Raindrop Spectra: A Tool for Cloud Physics and Cloud Remote Sensing," *J. Appl. Meteor.*, **40**, pp 1118-1140.

90. Tropical Rainfall Measuring Mission Science Data and Information System Interface Control Specification (ICS) Between the Tropical Rainfall Measuring Mission Science Data and Information System (TSDIS) and the TSDIS Science User (TSU), TSDIS-P907, vol. 3, release 4.04, March 31, 1999.

91. Ulbrich, C., 1983: "Natural Variations in the Analytical Form of Raindrop Size Distributions," *J. Climate Appl. Meteor.*, **22**, pp 1764-1775.

92. Wexler, H., 1954: Observing the weather from a satellite vehicle, *J. Brit. Interplanetary Soc.*, **13**, pp 269-276.

93. Wexler, H., 1957: The satellite and meteorology, *J. Astronaut.*, **4**, pp 1-6..

94. Wexler, R. and Swingle, D., 1947: Radar storm detection, *Bull. Am. Meteorol. Soc.*, **28**, pp 159-167.

95. Widger, W. K. and Touart, C. N., 1957: Utilization of satellite observations in weather analysis and forecasting, *Bull. Am. Meteorol. Soc.* **38**, pp 521-533.

96. Willis, P. T., 1984: Functional fits to some observed drop size distributions and parameterization of rain, *J. Atmos. Sci.*, **41**, pp 1648-1661.